Spatio-temporal control of the cytosolic redox environment in C. elegans

Spatio-temporal control of the cytosolic redox environment in *C. elegans*

A dissertation presented

by

Catalina Romero

to

The Committee on Higher Degrees in Systems Biology

in partial fulfillment of the requirements
for the degree of

Doctor of Philosophy

in the subject of

Systems Biology

Harvard University
Cambridge, Massachusetts

August 2013

Advisor: Professor Walter Fontana   Author: Catalina Romero

Spatio-temporal control of the cytosolic redox environment in *C. elegans*

Abstract

Compartmentalization of redox reactions is essential to all life forms. However, it has been difficult to study the redox potential of cellular environments within intact, living organisms. It is not known how this variable changes over the life of a multicellular organism, from its conception to death. Cell-types with various energetic requirements may differentiate the redox potentials of their cytosols, as has been suggested by biochemical measurements on dissected tissues. Unfortunately, these disruptive measurements preclude the investigation of dynamical changes taking place in the organism over space and time, under normal physiological conditions or in response to stimuli.

Within cellular compartments, protein activity can respond to changes in the local redox environment through the reversible oxidation of cysteine thiols. For the majority of cysteines in the proteome, this interaction takes place through equilibration with the glutathione pool; this raises the question whether this redox pool acts as a buffer, or instead as a sensitive media, transducing information from a local physiological state into protein function.

To pursue this question, we measured the spatio-temporal distribution of redox potential of the cytosolic glutathione pool, E_{GSH}, in the nematode *C. elegans*. We used a genetically encoded redox sensor to quantify E_{GSH} using ratiometric fluorescence microscopy. We found the steady state of the glutathione redox potential for different tissues (-268 mV to -271 mV) to be far from its buffering regime; these values were found instead in a regime where E_{GSH} exhibits large changes in response to slight changes in the fraction of oxidized glutathione. This supports the idea that the glutathione pool acts as a responsive media, which integrates and broadcasts a local physiological state. Our work presents an alternative to the commonly held view that glutathione is a

buffering system, preventing change in the oxidative state of cysteine thiols in the proteome.

We also found that the cytosolic redox environment is spatially structured *in vivo*: in the feeding organ, the pharynx, muscles segments show distinct redox potentials. These discrete redox environments occur despite the physical and electrical coupling of their cytosols through gap junctions. The spatial pattern observed persists upon oxidative stress, with specific muscles exhibiting unique E_{GSH} response dynamics. We identified a mechanism that controls levels of E_{GSH} as well as its spatial differentiation: insulin signaling modulates the level of cytosol oxidation, and the FOXO/DAF-16 transcription factor contributes to the spatial patterning of cytosolic E_{GSH} in feeding muscle.

Insulin signaling also modulates the cytosolic redox environment in other tissues, and it does so in a tissue-specific manner. Furthermore, we show that remote action of the transcription factor DAF-16 in the intestine lowers the cytosolic redox environment in feeding muscles, suggesting that tissues can influence each other's redox state in a cell non-autonomous manner.

The link between redox potential and insulin signaling – a major determinant of lifespan – prompted us to investigate the effects of aging on the redox pattern. We observed the pharyngeal glutathione pool during aging, and discovered that the spatial differentiation of the cytosolic redox potential undergoes structured changes. Our results show that insulin signaling modulates those changes. Notably, while the absolute level of E_{GSH} is uncorrelated with lifespan, we do find a correlation between the spatial differences in redox potential, and the remaining lifespan of an animal. This shows that the spatial patterning of the redox environment of the pharynx is linked to the aging process.

Table of Contents

Chapter 4.

Changes in the spatial pattern of cytosolic redox potential during development and aging

Part 1 – Cytosolic redox potential and anterior-posterior redox pattern in the pharyngeal muscle during development

Part 2 – Age-dependent changes in cytosolic redox potential are regulated by insulin signaling

Chapter 5.

Differences in E_{GSH} across tissues and tissue communication

List of Figures

List of Figures *(continued)*

List of Tables

"Life is nothing but electrons

looking for a place to rest"

Albert Szent-Györgyi,

Nobel Prize in physiology, 1937

Chapter 1

Introduction to redox biology and the development

of genetically encoded redox sensors

Redox reactions are part of metabolism and cell signaling

All known forms of life depend on the compartmentalization of redox potentials. Autotrophic organisms, such as plants and cyanobacteria, use sunlight to create redox gradients through carbon fixation, while heterotrophic organisms, like us, depend on those redox gradients for our maintenance (Herrmann and Dick, 2012). Whichever carbon source an organism employs, catabolism and anabolism can take place concurrently in the cell, thanks to the spatial separation of electrochemical fluxes, where molecules accept or donate electrons in accordance with the redox potential of the subcellular compartment in which they are contained.

Besides playing a central role in bioenergetics and metabolism, redox biology is also an integral part of cell signaling and cell decision-making. The use of reactive oxygen species (ROS) as signaling molecules is evolutionarily conserved (Schippers et al., 2012). One hypothesis suggests that this mode of communication was implemented during the evolution of multicellularity, as a way to coordinate cellular metabolism and growth between cells (Blackstone, 2000; Lalucque and Silar, 2003): for example, the social amoeba *Dictyostelium discoideum* shifts from unicellular to multicellular form using superoxide as a signaling intermediate (Bloomfield and Pears, 2003), and its development and differentiation require the action of NADPH oxidases (Lardy et al., 2005).

Spatio-temporal resolution in redox measurements

Because of their diffusibility and reactivity, endogenously produced oxidants are good candidates to broadcast chemical events locally and transiently. Indeed, the cell uses

protein redox modifications to integrate information, linking metabolic status to signaling events (Fisher-Wellman and Neufer, 2012; Wang et al., 2012). A quantitative measurement of protein redox modifications *in vivo*, with high spatial and temporal resolution, would be a valuable resource for investigating the redox processes that take place in the context of the living system. Until recently, though, our capacity to observe and quantify dynamic redox processes in the context of living cells, tissues, or whole organisms was constrained by technical limitations, such as the disruptive nature of homogenizing procedures (Meyer and Dick, 2010).

This constraint was removed with the development of genetically encoded redox fluorescent sensors, which makes *in vivo* study of the spatial and temporal dynamics of redox homeostasis possible within the context of the whole organism. The family of redox-sensitive Green Fluorescent Proteins (roGFPs) is based upon the two distinct excitation spectra exhibited by the GFP fluorophore, dependent on its protonation state. Wild-type GFP has two widely separated excitation maxima (Tsien 1998): the neutral form of the fluorophore has a higher peak of excitability at 395 nm, and a lower peak of excitability at 475 nm compared to the anionic form.

Leveraging this difference in excitation spectra, the Remington group engineered fluorescent proteins that report structural changes in response to environmental conditions. In roGFPs, the protonation state of the fluorophore becomes redox sensitive via the introduction of a pair of cysteines (S147C/Q204C) into the β-strands 7 and 10, in close proximity to the fluorophore. When these thiol groups oxidize, an intramolecular

disulfide bond is formed, causing structural rearrangements that affect the protein's two excitation maxima in opposite directions (Hanson et al., 2004). The reversible redox reaction between adjacent cysteines allows us to monitor the redox potential of the thiol-disulfide bond via ratiometric fluorescence microscopy.

What is roGFP measuring?

From a total of 10,507,692 codons that belong to the 23,865 proteins in *C. elegans*, 2.0084% encode cysteines (Prof. Dr. Bernd Moosmann, personal communication). From approximately 211,000 cysteine residues, then, 10-20% are expected to be oxidizable thiols exposed to the solvent (Jones 2008, based in estimations for the human proteome). This large number of redox-sensitive cysteines are broadly distributed among signaling, regulatory and structural proteins. These thiol groups could be regulated by two major cellular redox control mechanisms: the glutathione thiol (GSH) / glutathione disulfide (GSSG) redox couple, or the thioredoxin (Trx) mechanism. GSH/GSSG is the most abundant thiol in the cell; found in millimolar concentration, it is thought to react as a generalist with most cysteine-containing proteins. The Trx are small proteins present in the cell at concentrations several orders lower than GSH, and they are thought to act as specialists, dedicated to the redox regulation of specific targets[1] (Jones 2008).

The oxidation and reduction of roGFP cysteines is controlled by the GSH/ GSSG redox couple, therefore roGFP provides a window into the redox state of many other thiol

---

[1] Although Trx can bind to many substrates, kinetic studies shows that their specificities for different targeted proteins are based in their differential rates of catalysis.

groups in the proteome, whose redox states are also regulated by the glutathione potential. Through *in vitro* experiments, Meyer et al., 2007 established that roGFP equilibrates with the GSH/GSSG pool through the action of glutaredoxins. Several other redox mechanisms were tested for their interaction with roGFP, including small molecules like ascorbate and NADPH, or other catalytic mechanisms like thioredoxins and protein disulfide isomerases (PDIs), without affecting the redox state of the sensor (Meyer et al., 2007; Gutscher et al., 2008). Thus roGFPs are considered *bona fide* sensors for the glutathione redox potential (E_{GSH}).

Since their invention, the roGFP sensors have been diversified. Their midpoint potentials have been modified by changing the geometric strain of the disulfide bond, through mutation or insertion of residues. Currently available variants have midpoint potentials ranging between -300 mV to -230 mV. The kinetic properties of the sensor can also be modified by the introduction of basic amino acids in the proximity of the cysteines, which increases the reactivity of the thiols. In the case of roGFP1-R12 this last modification accelerated the *in vitro* kinetics of oxidation and reduction by 6-fold (Cannon and Remington, 2006). Yet the kinetics of oxidation of roGFPs *in vivo* happens faster than *in vitro* (Dooley et al., 2004), due to the catalytic action of glutaredoxins (Meyer et al., 2007). We chose the variant roGFP1-R12 for this study, based on its standard midpotential (-265 mV) and its enhanced rate of response.

Methodological Advantages of roGFP sensors

The development of these roGFP sensors offer several advantages:

i. Their ratiometric nature makes them more quantitative than other, intensity-based fluorescence methods (e.g. rxYFP, fluorescent dyes), since the ratio is insensitive to photobleaching or concentration changes.

ii. The ratiometric measurements are pH insensitive under the physiological range, from pH 5.5 to pH 8 (Schwarzlander et al., 2008).

iii. Because they are genetically encoded, these sensors can be targeted to specific cell compartments and tissues, enabling the study of redox biology with unprecedented spatial resolution.

iv. The reversibility of the thiol/sulfide reaction between the two cysteines opens the possibility of investigating redox dynamical changes happening *in vivo,* in short timescales.

v. Lastly, their non-disruptive nature allows studying redox biology in the context of the cell and the whole organism.

Other methods to study redox biology include measurements of glutathione by HPLC (Go et al.*,* 2008), redox western blot of thioredoxins (Fernando et al., 1992; Halvey et al., 2005), enzymatic assays in glutoredoxins (Lillig, 2008) and quantification of the thiol groups in the proteome by OxICAT (Leichert et al., 2008). These methods are highly specific, either for the redox couple under study or, in the case of OxICAT, by uncovering the identity of the proteins through mass spectrometry. They are limited, however, in that they require homogenization of the biological sample: tissue homogenization and cell disruption not only destroy information about compartment-specific redox states, but also preclude the ability to investigate how these subsystems

integrate information about their redox state to achieve homeostasis at the organismal

level.

Uses of roGFP in other organisms

The use of roGFP sensors in living cells, e.g. mammalian cell culture or tissue slices, is

transforming our ability to investigate redox processes, being particularly useful in

applications where the spatial and temporal resolution of redox changes are fundamental

to understanding a phenomenon. An elegant example was provided by Guzman et al.,

2010, in the investigation of the specific oxidative response observed in subpopulations

of dopaminergic neurons. The ability to measure mitochondrial roGFP oxidation at

single-cell resolution in midbrain slices revealed higher levels of oxidation in

dopaminergic neurons belonging to the substantia nigra pars compacta[2], compared to

neighboring dopaminergic neurons of the ventral tegmental area. This made it possible to

identify membrane calcium fluxes in autonomous pacemaking as a causative factor for

the higher oxidation levels of dopaminergic neurons in the substantia nigra pars

compacta. The oxidative response due to calcium fluxes is not observed in the

neighboring dopaminergic neurons in the ventral tegmental area, a region that is less

susceptible to Parkinson's disease.

The usefulness of roGFPs sensors increases as it becomes possible to measure oxidation

levels in multicellular organisms with spatial and temporal resolution. What are the redox

---

[2] Parkinson's disease results from the neurodegeneration of dopaminergic neurons in the
substantia nigra pars compacta. This subpopulation of neurons is particularly susceptible
to neurodegeneration associated to oxidative stress.

changes that actually occur in the physiological context of the whole organism? What is

the spatial and temporal distribution of those events? Which redox differences exist

naturally between the different tissues and cell types within the body? To what extent can

these basal redox states be affected by genetic, behavioral and environmental factors,

such as feeding, physical activity, or infection? Albrecht et al., 2011 pioneered the effort

of quantitatively mapping the glutathione redox potential of *Drosophila* larvae. They

found endogenous differences in the basal redox states between tissues, and identified

localized redox changes in fat tissue associated with changes in the feeding behavior.

Although the opacity of the adult fly is not amenable to ratiometric fluorescence

microscopy, their group developed a chemical method to fix the redox state of roGFP,

studying the histological samples under fixation. Under this chemical modification, they

observed age-dependent redox changes that are tissue-specific and compartment specific.

C.elegans is a great model organism for studying redox biology *in vivo,* due to its

transparency and genetic tractability. The first use of roGFP sensors in *C.elegans* comes

from the Nehrke laboratory, where they investigated redox changes in mitochondrial

fragmentation (Johnson and Nehrke, 2010) and the relationship between oxidative stress

with cytosolic acidification (Johnson et al., 2012). In addition, other two groups (Back et

al., 2012; Knoefler et al., 2012) have performed ratiometric fluorescent measurements to

study different aspects of the redox biology in the development and aging of the worm.

In both cases, they use sensors that involve several chemical reactions, which can

complicate interpretation. A detailed discussion about the chemical mechanisms involved

in these different types of ratiometric sensors will be presented in Chapter 2, when we

discuss the methodological details of ratiometric measurements using roGFP1_R12 in depth. Once the chemical basis for each of these methods is discussed, we will examine the results from Back et al., 2012; Knoefler et al., 2012, in detail, in Chapter 4.

Roadmap

Our work reveals the existence of tissue-scale spatial patterns in the cytosolic redox potential in living nematodes. These spatial differences in cytosolic E_{GSH} redox potential change over development and adulthood, and are under the control of insulin signaling. In Chapter 2 we discuss how we developed a method for quantifying E_{GSH} in living nematodes. We explain how we built the sensor with optimized expression in *C.elegans*, how we validated it *in vivo*, and how we tested its reversibility and kinetic properties. Then we discuss how we established the dynamic range of the sensor, quantified with our microscopy set up to determine the empirical parameters needed for transforming ratiometric fluorescence measurements into E_{roGFP} using the Nernst equation. We conclude the chapter with a discussion about the biological meaning of our measurements.

In Chapter 3 we show the existence of a tissue-scale spatial pattern of E_{GSH} in the *C. elegans* pharynx. We observe an anterior-posterior difference in redox potential of up to 7.5 mV. Despite being connected by gap junctions, cytosolic E_{GSH} seems to differentiate from its neighbors, and cells of the same tissue exhibit a remarkably discrete redox

phenotype. Exposing the worm to oxidative stress reveals further differentiation between muscle segments. Time series of individual animals under stress shows how muscle segments have distinct spatio-temporal responses when exposed to external oxidants. We then seek to identify a mechanism for the spatial differentiation of E_{GSH} between muscle segments. We find that insulin signaling modulates the level of oxidation, and that the FOXO/DAF-16 transcription factor contributes to the spatial differentiation of cytosolic E_{GSH} in feeding muscle.

The redox differentiation between adjacent muscle segments is not a static phenomenon. In Chapter 4 we investigate the pattern formation of cytosolic E_{GSH} during development and its changes during aging. In developing larvae we observe an interesting phenotype: the majority of individuals have a more homogeneous redox potential across the anterior-posterior axis, with exception of a small fraction of individuals, particularly in L3 and L4 larval stages, which exhibit exacerbated anterior-posterior differences and unusual high levels of oxidation. We hypothesize this subpopulation corresponds to individuals in the molting process, where NADPH oxidases produce superoxide to crosslink the collagen molecules of the newly shed cuticle. This observation exemplifies the discreteness of cytosolic E_{GSH} as a "cellular variable", distinct from neighboring and connected cytosols.

After completion of larval development, we find that the Anterior-Posterior difference in redox potential observed in young individuals is established by day two, and it changes polarity throughout adulthood. In the insulin receptor *daf-2* mutant, a long-lived mutant with decreased insulin signaling activity, we observe a monotonic decline in the

oxidation levels throughout adulthood. Under this genetic perturbation we observe a similar trend in the spatial changes of cytosolic E_{GSH} with age. The polarity changes throughout adulthood with a similar, but different offset. Importantly, we find that these Anterior-Posterior redox differences are correlated with organismal lifespan in wild type (R^2=0.20, p<0.0001), while the absolute level of tissue oxidation is uncorrelated with lifespan.

In Chapter 5 we focus on the cytosolic E_{GSH} differences across tissues, and we present evidence of a cell non-autonomous component in the regulation of the cytosolic redox potential. We measure the cytosolic E_{GSH} in intestine, PLM neurons and feeding muscle in wild type young individuals and find that these three tissues have different cytosolic E_{GSH} baselines. Then we ask whether insulin signaling regulates the cytosolic E_{GSH} in intestine and PLM neurons, as was shown for feeding muscle. We find that insulin signaling has tissue-specific effects in the regulation of redox potential: compared to wild type, *daf-2* mutants exhibit lower cytosolic E_{GSH} in feeding muscles and intestine, but decreased insulin signaling has no effect in the PLM neurons. The effect of insulin signaling in the cytosolic redox potential requires the activity of the FOXO/DAF-16 transcription factor, and we test whether this transcription factor acts locally or remotely to control cytosolic redox potential. In *daf-16(mu86); daf-2(e1370)* double mutants, the action of *daf-16(+)* in feeding muscle is sufficient to lower E_{GSH} values in this tissue, compared to their siblings with no pharyngeal *daf-16(+)* expression. Remarkably, the action of *daf-16(+)* in intestinal cells is also sufficient to lower E_{GSH} in feeding muscles,

despite the absence of *daf-16* in this tissue; this suggests that the pharyngeal cytosolic redox environment can be modified by the action of other tissues.

The spatial differentiation of the cytosolic redox environment within a tissue and between tissues, and the range of values observe at steady state, provides a new perspective changing the way we think about E_{GSH} cytosolic redox potential as a buffering system with expected homogeneous values.

Authors Contribution

C.R. wrote the text.

Chapter 1 – References

1. Albrecht SC, Barata AG, Grosshans J, Teleman AA, Dick TP (2011) In vivo mapping of hydrogen peroxide and oxidized glutathione reveals chemical and regional specificity of redox homeostasis. Cell Metab 14: 819-829.

2. Back P, De Vos WH, Depuydt GG, Matthijssens F, Vanfleteren JR, et al. (2012) Exploring real-time in vivo redox biology of developing and aging Caenorhabditis elegans. Free Radic Biol Med 52: 850-859.

3. Blackstone NW (2000) Redox control and the evolution of multicellularity. Bioessays 22: 947-953.

4. Bloomfield G, Pears C (2003) Superoxide signalling required for multicellular development of Dictyostelium. J Cell Sci 116: 3387-3397.

5. Cannon MB, Remington SJ (2006) Re-engineering redox-sensitive green fluorescent protein for improved response rate. Protein Sci 15: 45-57.

6. Dooley CT, Dore TM, Hanson GT, Jackson WC, Remington SJ, et al. (2004) Imaging dynamic redox changes in mammalian cells with green fluorescent protein indicators. J Biol Chem 279: 22284-22293.

7. Fernando MR, Nanri H, Yoshitake S, Nagata-Kuno K, Minakami S (1992) Thioredoxin regenerates proteins inactivated by oxidative stress in endothelial cells. Eur J Biochem 209: 917-922.

8. Fisher-Wellman KH, Neufer PD (2012) Linking mitochondrial bioenergetics to insulin resistance via redox biology. Trends Endocrinol Metab 23: 142-153.

9. Go YM, Jones DP (2008) Redox compartmentalization in eukaryotic cells. Biochim Biophys Acta 1780: 1273-1290.

10. Gutscher M, Pauleau AL, Marty L, Brach T, Wabnitz GH, et al. (2008) Real-time imaging of the intracellular glutathione redox potential. Nat Methods 5: 553-559.

11. Guzman JN, Sanchez-Padilla J, Wokosin D, Kondapalli J, Ilijic E, et al. (2010) Oxidant stress evoked by pacemaking in dopaminergic neurons is attenuated by DJ-1. Nature 468: 696-700.

12. Halvey PJ, Watson WH, Hansen JM, Go YM, Samali A, et al. (2005) Compartmental oxidation of thiol-disulphide redox couples during epidermal growth factor signalling. Biochem J 386: 215-219.

13. Hanson GT, Aggeler R, Oglesbee D, Cannon M, Capaldi RA, et al. (2004) Investigating mitochondrial redox potential with redox-sensitive green fluorescent protein indicators. J Biol Chem 279: 13044-13053.

14. Herrmann JM, Dick TP (2012) Redox Biology on the rise. Biol Chem 393: 999-1004.

15. Johnson D, Allman E, Nehrke K (2012) Regulation of acid-base transporters by reactive oxygen species following mitochondrial fragmentation. Am J Physiol Cell Physiol 302: C1045-1054.

16. Johnson D, Nehrke K (2010) Mitochondrial fragmentation leads to intracellular acidification in Caenorhabditis elegans and mammalian cells. Mol Biol Cell 21: 2191-2201.

17. Jones DP (2008) Radical-free biology of oxidative stress. Am J Physiol Cell Physiol 295: C849-868.

18. Knoefler D, Thamsen M, Koniczek M, Niemuth NJ, Diederich AK, et al. (2012) Quantitative in vivo redox sensors uncover oxidative stress as an early event in life. Mol Cell 47: 767-776.

19. Lalucque H, Silar P (2003) NADPH oxidase: an enzyme for multicellularity? Trends Microbiol 11: 9-12.

20. Lardy B, Bof M, Aubry L, Paclet MH, Morel F, et al. (2005) NADPH oxidase homologs are required for normal cell differentiation and morphogenesis in Dictyostelium discoideum. Biochim Biophys Acta 1744: 199-212.

21. Leichert LI, Gehrke F, Gudiseva HV, Blackwell T, Ilbert M, et al. (2008) Quantifying changes in the thiol redox proteome upon oxidative stress in vivo. Proc Natl Acad Sci U S A 105: 8197-8202.

22. Lillig CH, Berndt C, Holmgren A (2008) Glutaredoxin systems. Biochim Biophys Acta 1780: 1304-1317.

23. Meyer AJ, Brach T, Marty L, Kreye S, Rouhier N, et al. (2007) Redox-sensitive GFP in Arabidopsis thaliana is a quantitative biosensor for the redox potential of the cellular glutathione redox buffer. Plant J 52: 973-986.

24. Meyer AJ, Dick TP (2010) Fluorescent protein-based redox probes. Antioxid Redox Signal 13: 621-650.

25. Schippers JH, Nguyen HM, Lu D, Schmidt R, Mueller-Roeber B (2012) ROS homeostasis during development: an evolutionary conserved strategy. Cell Mol Life Sci 69: 3245-3257.

26. Schwarzlander M, Fricker MD, Muller C, Marty L, Brach T, et al. (2008) Confocal imaging of glutathione redox potential in living plant cells. J Microsc 231: 299-316.

27. Tsien RY (1998) The green fluorescent protein. Annu Rev Biochem 67: 509-544.

28. Wang TA, Yu YV, Govindaiah G, Ye X, Artinian L, et al. (2012) Circadian rhythm of redox state regulates excitability in suprachiasmatic nucleus neurons. Science 337: 839-842.

Chapter 2

Quantification of redox potential in living nematodes by ratiometric fluorescence microscopy

Abstract

We wanted to investigate how the different cells in a multicellular organism coordinate their redox states. The question compelled us to develop non-intrusive redox measurements, with spatial resolution, so that we could investigate these relationships in the physiological context of a living animal. To observe redox processes *in vivo*, we generated transgenic worms expressing the redox probe roGFP1_R12 in the feeding muscle of *C.elegans*. This sensor was engineered from wild-type GFP through the insertion of two cysteines, whose thiol groups can be reversibly oxidized to form an intramolecular disulfide bond. These structural rearrangements transduce into changes in the spectral properties of the chromophore, making it possible to study the degree of protein oxidation using ratiometric fluorescence measurements.

To estimate the dynamic range of the sensor we treated worms sequentially with oxidants and reductants: the fluorescence intensities and their ratio, R, show that the sensor responds quickly, reversibly, and exhibits a large, 7.8-fold, dynamic range. Knowing the fluorescence intensities of fully reduced and fully oxidized sensors in single individuals, allows us to relate R to the fraction of oxidized sensor, OxD_{roGFP}. Given OxD_{roGFP} and the sensor's midpoint potential, the redox potential, E_{roGFP}, can be calculated by the Nernst equation. The redox state of the sensor, like that of most cysteine-containing proteins, responds to the redox potential of the glutathione disulfide (GSSG)/glutathione thiol (GSH) couple, E_{GSH}, thus providing a general window onto the oxidation state of many other cysteine-containing proteins in the cell.

Glutathione has often been referred to as the "redox buffer of a cell". Importantly, our preliminary measurements of baseline E_{GSH} levels, along with the formal tissue-specific quantifications shown in chapter 5, place the glutathione redox potential measured in all tissues (-268 mV to -271 mV) far outside of the glutathione buffering regime. These results indicate that, in *C.elegans* tissues, E_{GSH} is sensitive to small changes in the fraction of oxidized glutathione; supporting the perspective that glutathione is a responsive physiological variable rather than an unresponsive buffering system.

Chapter 2 – Introduction

The oxidation state of cysteine thiols can regulate the activity, interactivity, structure and stability of proteins (Herrmann & Dick, 2012). The cell uses these reversible modifications to integrate global information, such as its metabolic status, to the local activity of individual proteins (Fisher-Wellman & Neufer 2012; Wang et al., 2012). For the majority of proteins containing redox sensitive cysteines [3], the probability of being in an oxidized or reduced state is determined by the glutathione redox potential, E_{GSH}. In turn, E_{GSH} represents a global variable determined by a collective output: it contains information about many processes that are ultimately linked to NADPH availability, the 'currency' of reducing equivalents in the cell. The perspective of E_{GSH} being an integrative variable offers an alternative to the classic interpretation of glutathione being a buffering system, whose sole function is simply to avoid oxidative damage.

To observe redox processes *in vivo*, we generated transgenic worms expressing the redox sensor roGFP1_R12 (Cannon and Remington, 2006). This sensor was engineered from wild-type GFP by insertion of two cysteines (S147C/Q204C) in the β-strands 7 and 10, in close proximity to the fluorophore. The thiol groups of these two residues can reversibly oxidize, and this redox reaction changes the excitation properties of the fluorophore: when an intramolecular disulfide bond is formed, structural rearrangements affect the

---

[3] The cell has two major systems to control thiol-disulfide groups: the glutathione and thioredoxin systems. The glutathione system is thought to act as a generalist, while the thioredoxin system is thought to specialize, being dedicated to the redox regulation of specific targets (Jones 2008).
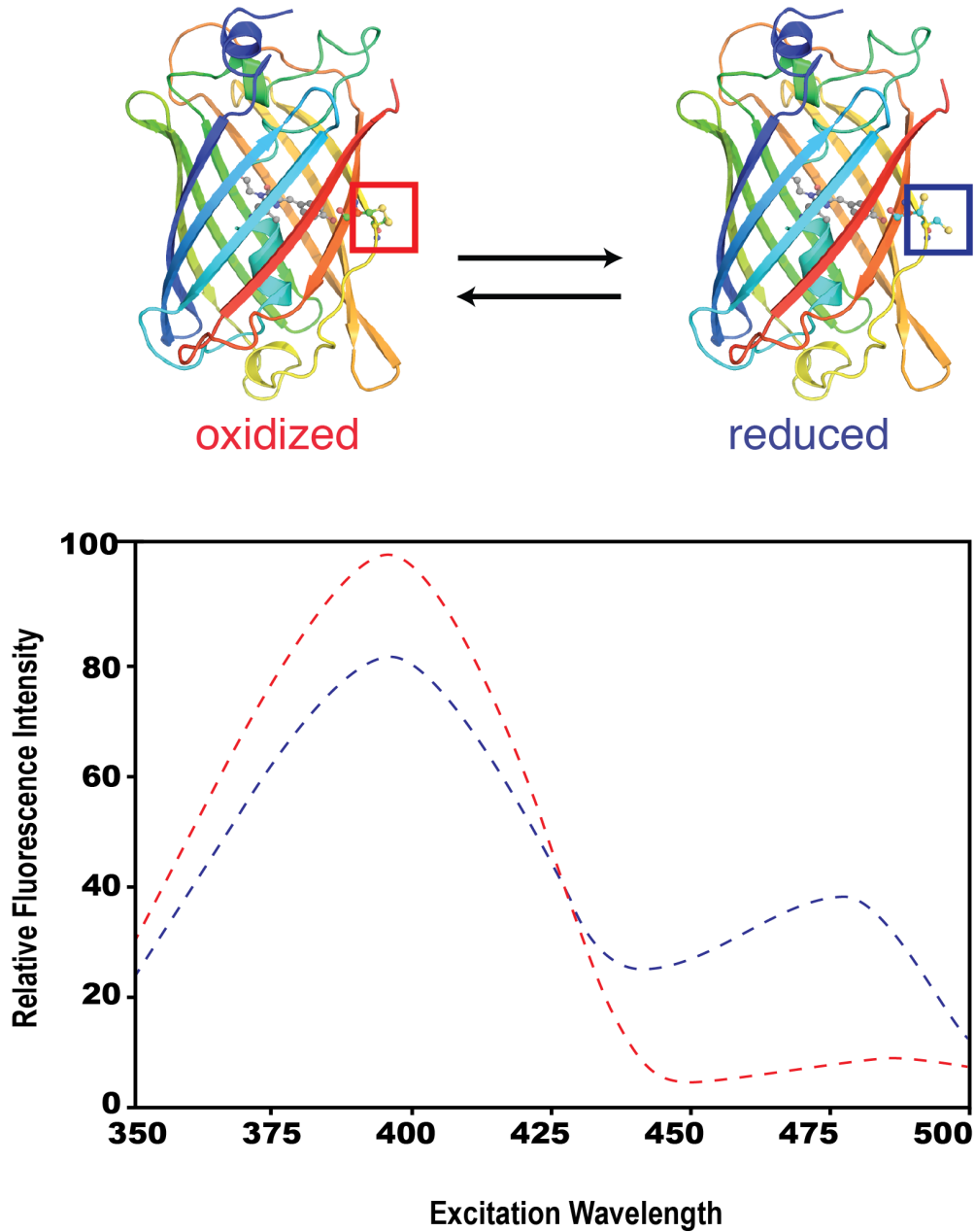
Figure 2.1: The redox sensitive Green Fluorescent Protein (roGFP). (A) The two cysteines introduced in the β- barrel oxidize reversibly, forming a disulfide bond; (B) Excitation spectra of roGFP1. The structural rearrangements caused by the disulfide bond deflect the excitation spectra of the protein in opposite directions (adapted from Hanson et al., 2004).

protonation state of the Y66[4], deflecting the protein's two excitation maxima in opposite directions (Figure 2.1). In this way, the reversible changes in the two cysteines allow us to monitor the redox potential of the thiol-disulfide bond via ratiometric fluorescence microscopy (Hanson et al., 2004; Dooley et al., 2004). Like most cysteine-containing proteins, the redox state of the sensor responds to the redox potential of the glutathione disulfide (GSSG)/glutathione thiol (GSH) couple, thus providing a window into the oxidation state of the cysteine-containing proteins controlled by the cell's major redox system.

How to quantify E_{GSH} *in vivo* from ratiometric fluorescence microscopy

The equilibrium between the GSH/GSSG redox couple, and the redox couple defined by the reduced ($roGFP_{Red}$) and the oxidized form of the sensor ($roGFP_{Ox}$), can be described by the Nernst equation (*Eq. 1*):

$$E_{GSH} = E^{0'}{}_{GSH} - \frac{RT}{zF} \ln \frac{[GSH]^2}{[GSSG]} = E^{0'}{}_{roGFP} - \frac{RT}{zF} \ln \frac{[roGFP_{Red}]}{[roGFP_{Ox}]} = E_{roGFP}$$

In this equation R is the gas constant (8.315 J/K^{-1} mol^{-1}), T is the absolute temperature (298.15 K), z is the number of electrons transferred (2 in this case), and F is the Faraday constant (9.648 104 C mol^{-1}). We can express the mass-action ratio for each of these two redox couples in terms of the fraction of molecules containing a disulfide bond over the

[4] In the wild type GFP, the protonated state or neutral form of the fluorophore has an excitation peak with a maximum at 395 nm (A band); in its de-protonated or anionic form (B-band), it has an excitation peak with a maximum at 475 nm (B band) (Tsien, 1998). This dual-excitation state is the key factor enabling the rational design of ratiometric roGFP sensors (Reviewed in Meyer & Dick, 2010).

total number of molecules. The fraction oxidized is known in the field as *OxD* for

oxidation degree (*Eq.2*):

$$OxD_{GSH} = \frac{2[GSSG]}{[GSH] + 2[GSSG]} = \frac{2[GSH]}{GSH_{Total}}$$

$$OxD_{roGFP} = \frac{[roGFP_{ox}]}{[roGFP_{Red}] + [roGFP_{Ox}]}$$

Using the fraction oxidized, we could rewrite the Nernst equation for both couples (*Eq. 3*):

$$E_{GSH} = E^{0\prime}_{GSH} - \frac{RT}{2F} \ln \left(\frac{2GSH_{Total}(1 - OxD_{GSH})^2}{OxD_{GSH}} \right)$$

$$E_{roGFP} = E^{0\prime}_{roGFP} - \frac{RT}{2F} \ln \left(\frac{1 - OxD_{roGFP}}{OxD_{roGFP}} \right)$$

Notice that E_{roGFP} depends exclusively on the $[roGFP_{Red}]/[roGFP_{Ox}]$ ratio. In contrast,

because the oxidation of glutathione is a second order reaction, E_{GSH} will depend on two

factors: the [GSH]/[GSSG] ratio, and the total concentration of glutathione equivalents,

[GSH]$_{Total}$. A higher concentration of total glutathione will render the E_{GSH} potential more

negative[5].

Depending on the redox state, each sensor's molecule will emit a fixed amount of light

(at 535 nm) when excited at 410nm and when excited at 470 nm. Thanks to this

---

[5] A 10-fold increase in total glutathione concentration will lower E_{GSH} by 30mV, as illustrated in Figure 2.6.

ratiometric nature, it is possible to express a relationship between the fraction of roGFP molecules oxidized ($OxD_{roGFP} = N_{ox}/N_{Total}$) and the macroscopic observable of the sensor, i.e. the ratio of fluorescence intensities measured in a population of molecules, when illuminated at 410 nm and 470 nm, $R=I_{410}/I_{470}$ (Meyer et al., 2007). Assuming that the total fluorescence intensity observed corresponds to the sum of the intensities of individual roGFP molecules, then the following relationship can be established (*Eq. 4*):

$$OxD_{roGFP} = \frac{R - R_{Red}}{\frac{I470_{Ox}}{I470_{Red}}(R_{Ox} - R) + (R - R_{Red})}$$

Where R is the actual ratiometric measurement ($R=I_{410}/I_{470}$), R_{Red} is the ratio when the sensor is fully reduced, R_{Ox} is the ratio when the sensor is fully oxidized, $I470_{Ox}$ corresponds to the intensity of emission when the fully oxidized sensor is excited at 470 nm light, and $I470_{Red}$ corresponds to the intensity of emission when the fully reduced sensor is excited at 470 nm light. The term $I470_{Ox}/I470_{Red}$ can be thought of as an "instrument factor", as it describes the relative efficiency of the light path at 470 nm illumination in the two extremes of the dynamic range of the sensor. To extract quantitative information about E_{GSH} from ratiometric fluorescence measurements, it is necessary then to find three empirical parameters: R_{Red}, R_{Ox} and the instrument factor. Once these parameters are calculated for a specific microscopy setup, it is possible to express R in terms of OxD_{roGFP}. Subsequently, knowing sensor's midpoint potential (-265 mV) we can calculate E_{roGFP} by expressing the Nernst equation in terms of OxD_{roGFP} (*Eq. 3*).

E_{roGFP} **equilibrates with *E_{GSH}* *in vivo* via glutaredoxin**

The fast equilibration of roGFP with the GSH/GSSG couple requires the enzymatic

action of Glutaredoxin. Initially, it was unclear whether the cysteine residues engineered

in this exogenous protein would be targeted by the catalytic mechanisms controlling

thiol-disulfides within the cell. In the original report, however, it was noticed that roGFP2

in HeLa cells had EC_{50} three orders of magnitude lower than when treated *in vitro*

(Dooley et al., 2004). This suggested that a catalytic mechanism would be involved in the

equilibration of roGFP in the cell. Later, Meyer et al., 2007 showed that glutaredoxin

(Grx) was that missing link. Using incubation with pharmacological and enzymatic

agents, they showed that roGFP sensors are: a) sensitive to nanomolar concentrations of

GSSG; and b) interact only with glutathione. Other mechanisms tested so far, including

compounds such as NADPH and ascorbate, or enzymes such as thioredoxins (Trxs) and

protein disulfide isomerases (PDIs), have not affected the redox state of roGFP (Meyer et

al., 2007; Meyer & Dick, 2010). A version of roGFP fused to GRX has been designed

(Gutscher et al, 2008), and it will be discussed in the following section.

Comparison between redox fluorescence sensors

Several types of genetically encoded fluorescent redox probes have been engineered

within the last ten years. They belong to 3 basic families: HyPer, rxYFP and roGFPs

(Figure 2.2).

   i.   *HyPer*: this H_2O_2 sensor based on the regulatory domain of the prokaryotic

         transcription factor OxyR, which contains two cysteines critical to H_2O_2 sensing.
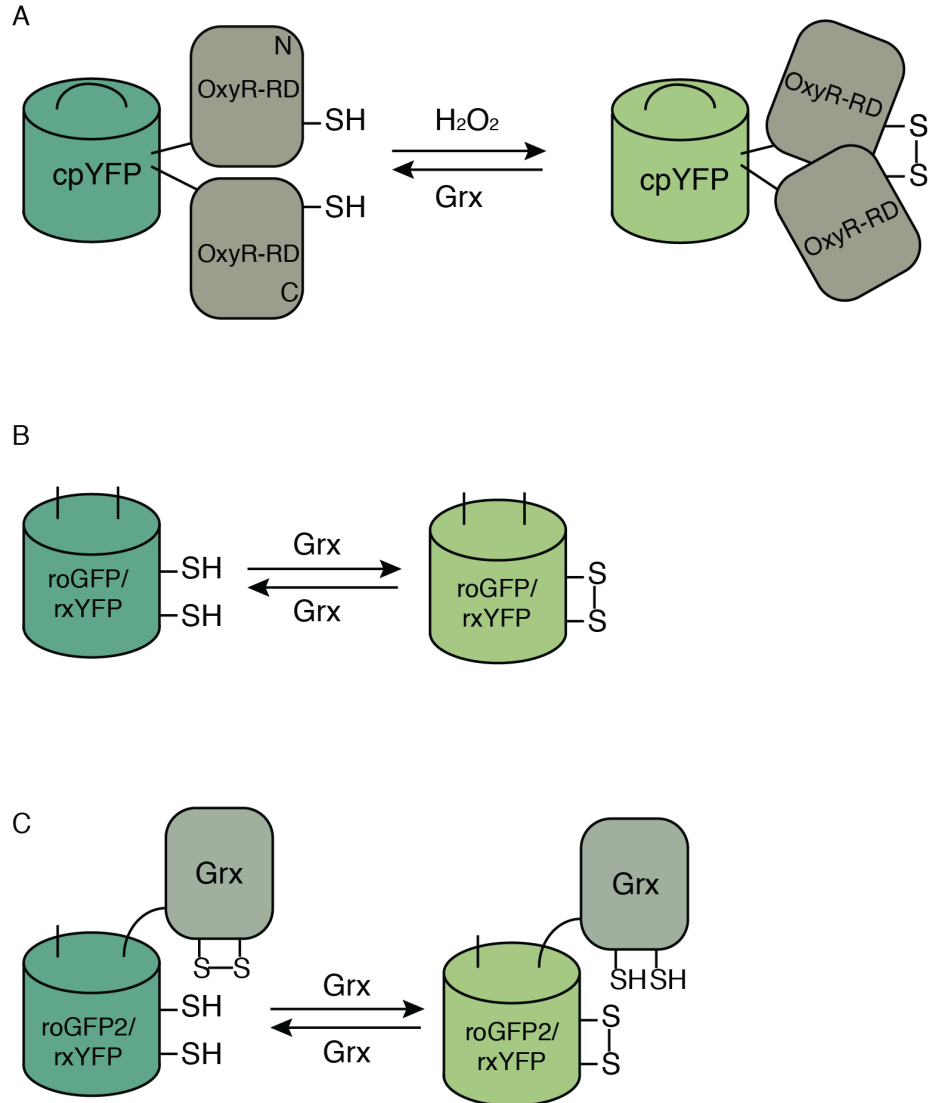
Figure 2.2: Families of genetically encoded redox sensors. (A) HyPer was designed by inserting cpYFP into the regulatory domain of the prokaryotic transcription factor OxyR. (B) roGFP and rxYFP were engineered by introducing a pair of cysteines in the proximity of the fluorophore. (C) Fusing roGFP/rxYFP with enzymes that catalyze redox reactions, such us in Grx and Orp1, changes the chemistry of the redox modification and can increase the equilibration rate *in vivo* (Adapted from Lukyanov and Belousov 2013).

ii.   By inserting a cpYFP in this domain, the conformational changes caused by the

disulfide bond formation will transduce into excitation changes at the maxima 420

nm and 500 nm, turning HyPer into a ratiometric sensor (Belousov et al., 2006).

The main advantage of this sensor compared to fluorescent dyes is its specificity

and sensitivity, reported to be in the nanomolar range. The principal disadvantage

is its high pH dependence: changes as small as 0.2 pH units can alter the ratio as

much as the full reduction or the full oxidation (Meyer & Dick, 2010; Lukyanov

& Belousov et al., 2013).

iii.   *rxYFP*: the creation of a redox-sensitive fluorescent proteins by introducing a pair

of cysteines in the proximity of its fluorophore was first attempted by the Jakob

Winther laboratory, and resulted in the design of rxYFP. Although this was

intended to be a ratiometric sensor, the protein does not fluoresce in the neutral

form of the chromophore, so rxYFP is a redox sensor based on total intensity

(Ostergaard et al., 2004). This sensor is pH-dependent as well: for both HyPer and

rxYFP, the Tyr 66 residue that becomes protonated in response to the disulfide

bond formation allows proton transfer to the media (Lukyanov & Belousov et al.,

2013), which explains their pH sensitivity.

iv.   *roGFP*: Both the ratiometric property and the pH-independence were achieved by

the Remington group, using GFP as backbone. roGFP1 and roGFP2 were

obtained by introducing a pair of cysteines (S147C/Q204C) in the β-strands 7 and

10, in wtGFP or EGFP (S65T variant) respectively. These ratiometric sensors

have excitation maxima around 400 nm and 475 nm, with a clear isosbestic point
at 425 nm (Hanson et al., 2004; Dooley et al., 2004).

It has been proposed that, by fusing roGFP sensors with enzymes involved in a particular type of redox regulation, the redox state of roGFP would equilibrate faster, and become as specific as the enzyme to which it is fused. Fusions with human glutaredoxin-1 (Grx-roGFP) and with the peroxidase Orp-1 (Opr1-roGFP) have been generated successfully (Gutscher et al, 2008; Gutscher et al, 2009). At this point it is important to notice the differences in the reversibility mechanisms of the glutathione sensors versus the hydrogen peroxide sensors. roGFP and Grx-roGFP are being oxidized and reduced by the same redox couple, thus interacting with only one redox potential: that of the GSH/GSSG pair. However, in the case of HyPer and and Opr1-roGFP, they are communicating with two redox potentials, as their reduction depends on the glutathione system of the cell. Therefore, they interact simultaneously with two redox couples: H_2O_2/H_2O and GSH/GSSG. An eventual change in the reducing capacity of the glutathione system (for example, decreased NADPH availability) will shift the balance towards a more oxidized HyPer, even if the H_2O_2 levels remain constant (Meyer and Dick, 2010).

The fusion Grx-roGFP shows greater kinetic rates and higher sensitivity than roGFP. We decided, however, to use the unmodified version of the roGFP sensor for the *in vivo* measurements in *C. elegans*. In our experience, obtaining a high intensity of fluorescence is one of the most critical factors for successful quantitative ratiometric measurements in living animals. We wanted to avoid any unexpected consequences that overexpressing a

key component of the thiol-disulfide control (like Grx) could have in our observable of interest. We were not concerned about the kinetic limit, since our primary goal was to investigate how steady state levels of E_{GSH} affect cytosolic proteins. In the eventual case that availability of Grx became a limiting factor for fast equilibration, we reasoned that this constraint would also affect the cytosolic endogenous proteins, which were the focus of our study.

This kinetic factor, however, could affect how the oxidative stress assay, presented in chapter 3, is interpreted. For that particular case we cannot confirm that the roGFP1_R12 sensor is indeed equilibrated with E_{GSH}. As we will see in this chapter, however, the oxidation kinetics of the sensor expressed in feeding muscle seems more than adequate: we observe the time taken to reach a half-maximal response ($t_{1/2}$) is below 90 sec.

Chapter 2 – Results

Based on previous experience with ratiometric measurements in the nematode, we consider a high signal-to-noise ratio to be one of the most critical factors for making quantitative *in vivo* measurements feasible. Therefore we decided to: *i)* build our own version of the sensor with optimized expression in *C.elegans*; and *ii)* optimize imaging media and microscopy conditions to minimize noise.

We built the *C.elegans* version of roGFP1_R12 from a GFP construct that had been previously optimized for higher expression efficiency in this organism, through the introduction of introns, UTRs and codon bias (Fire vector kit, Addgene). We generated transgenic worms expressing the sensor in the cytosol of pharyngeal muscle cells using the promoter for myosin-2 (*Pmyo-2::roGFP1_R12*). The fluorescence intensities in feeding muscle were consistent across conditions and suitably high: images using at least two-thirds of the dynamic range of the camera were obtained with exposure times of 40 msec for each excitation channel.

We chose to perform our measurements in open-plate microscopy[6], as it ensures normoxia and easily allows the tracking and recovery of individual worms. To optimize imaging conditions, we modified the standard NGM (Nematode Growth Media) into a simpler version called NIM (Nematode Imaging Media). Replacing agar with agarose and

---

[6] In our experience, the use of PDMS devices did not provide enough immobilization for ratiometric measurements: subtle movements of the head or contractions in the feeding muscles during pumping made it challenging to take two consecutive images without registration issues.

excluding peptone, we reduced the background autofluorescence of the media to 11% and 12% of the original value, when excited at 410 nm and 470 nm light; more importantly, the standard deviation of the estimation of background autofluorescence dropped 6-fold. Minimizing error in the estimation of background is particularly important in ratiometric measurements, where background subtraction from numerator and denominator can propagate the error.

To calculate the fraction of roGFP1_R12 molecules with a disulfide bond, OxD_{roGFP} (acronym used in the field for 'Oxidation Degree'), using ratiometric fluorescence measurements, we needed to determine the dynamic range of the sensor *in vivo*, and the ratio of I_{470} values when the sensor is fully oxidized versus when it is fully reduced – a parameter called Instrument Factor ($IF = I_{470\ Ox} / I_{470\ Red}$). For *IF* estimation, it was important to measure the dynamic range of the sensor in the same population of molecules, enclosed in a similar volume. To this end, we needed to achieve conditions of maximal oxidation and maximal reduction without bleaching and without changes in the volume of the tissue (i.e. muscle contraction), which could affect the signal intensities by dilution or concentration. First, we tested different incubation conditions for different oxidants: H_2O_2, *tert*-butyl hydroperoxide, 2,2'-Dipyridyldisulfide (Aldrithriol) and Diamide. Notice that the last two compounds directly oxidize the thiol groups of the sensor, while the two peroxides do not, due to the high pKa of these thiols (pKa ~9; Cannon and Remington, 2006); instead, they will oxidize the sensor via the GSH/GSSG redox couple[7].

---

[7] Interestingly, in time series experiments where worms were imaged for 60 to 90 minutes in the presence of 100mM *t*BuOOH, we notice a wide variability in the maximal *R* attained by different individuals, while that maximal value remained stable over time.

From all the conditions tested we found that sequential treatment with the oxidant

diamide (50 mM, Sigma), followed by treatment with the reducing agent dithiothreitol

(DTT, 100 mM, Sigma), resulted in maximal oxidation and reduction of the sensor,

respectively. These compounds affect the sensor's oxidation state without requiring the

GSSG/GSH couple, ensuring that full oxidation and reduction are not constrained by total

glutathione; neither did they cause bleaching or volume changes in the tissue of 1-day-old

individuals. In one such experiment, we estimated the dynamic range of the sensor

($R_{Ox}/R_{Red} = 7.8$) by acquiring R time-series in the procorpus of 40 animals, tracked

individually. These animals were first observed in the absence of treatment, and then

sequentially treated with 50 mM diamide for 90 min, followed by treatment with 100 mM

DTT for 120 min (Figure 2.3). Animals were imaged for 10 minutes before treatment,

and for the last 30 minutes of diamide and DTT treatment. All chemical incubations were

performed in NIM plates. We observed that all 40 animals exhibited a dramatic, stable

and reversible response to these treatments. We identified nine animals where the sensor

was first maximally oxidized and then maximally reduced (Figure 2.4). All of these

animals exhibited quite similar R_{ox}, R_{red}, and *IF* values, which resulted in similar

mappings between $R_{410/470}$ *and* OxD_{roGFP} and E_{roGFP} (Figure 2.4E and F). Thereafter, we

used the average values of R_{ox}, R_{red}, and *IF* from these animals to compute OxD_{roGFP} and

E_{roGFP}.

We think the different plateau values are caused by individual-to-individual variation in
the glutathione system capacity.

To test the kinetics of roGFP1_R12 oxidation and spontaneous recovery in living

nematodes, we performed time series experiments where the sensor was expressed in the

cytosol of pharyngeal muscle cells. Worms were imaged for 10 minutes before treatment;

they were then transferred to an oxidative media containing 50 mM diamide and imaged

for 60 minutes; and lastly they were transferred back to normal conditions and imaged

during recovery for an additionally 60 minutes (Figure 2.5). In this experiment, we

tracked the response of 10 animals individually, acquiring images once each minute, with

imaging gaps of 3 min and 4 min between transfers, respectively. Because all animals

reached near maximal OxD_{roGFP} values after 3 minutes in diamide, we conservatively

estimate that time to a half-maximal response ($t_{1/2}$) is lower than 1.5 minutes. The

recovery from diamide treatment exhibits slower kinetics[8]. We fitted the time series of

OxD_{roGFP} to a three-parameter exponential function to estimate $t_{1/2} = 4.1$ minutes for the

diamide-recovery phase (Figure 2.5). The fact that OxD_{roGFP} recovers quickly and

spontaneously from maximal oxidation to nearly baseline levels: a) indicates that E_{roGFP}

is equilibrating with E_{GSH} *in vivo*, and b) highlights the remarkable capacity of the tissue

to recover from severe oxidative stress in only a few minutes.

The assumption of equilibration between sensor and GSSG/GSH couple is warranted,

since OxD_{roGFP} recovers quickly and spontaneously from maximal oxidation to nearly

baseline levels (Figure 2.5), when worms are shifted from diamide treatment back to

---

[8] It is important to note that these kinetic rates might underestimate the response of the sensor *in vivo*, since the worms were not perfused with the oxidants, nor washed out to measure recovery. This experiment was done by transferring individual worms from one solid media to another by standard procedures, using a worm pick and bacteria: we expect to see residual bacteria around the worm after the diamide treatment.

normal conditions. In Figure 2.6 we show how the preliminary estimation of E_{GSH} values in baseline conditions (along with the values obtained in the more formal quantification presented in chapter 5) relates to the potential of the glutathione pool. The relationship between redox potential and the probability that a given protein thiol is in the oxidized state depends on its midpoint potential for first order reactions. In the case of glutathione, because is a second order reaction, it also depends on the total glutathione concentration. Cytosolic concentrations of total glutathione are consistently reported to be between 1 to 10 mM, which corresponds to E_{GSH} values of -151mV for 1mM $[GSH]_{total}$ to -181 mV for 10mM $[GSH]_{total}$ (Go and Jones 2008; Meyer and Dick 2010). Assuming total concentration of 1 or 10 mM we observe that the baseline levels of E_{GSH} are far from the buffering region of the glutathione couple, indeed they are located in the region of highest sensitivity, so that small changes in the fraction of oxidized glutathione will have a large impact in on E_{GSH}—quite the opposite of a buffering system. Indeed, in order to be in the buffering region, assuming constant pH, a total glutathione concentration of 10 M would be required. This perspective supports the notion of the glutathione pool as a sensitive media, where small changes in the fraction oxidized can be broadcasted to the redox state of proteins contained in a particular compartment.

Acknowledgements

Center for early training. We thank Tim Mitchinson, Gary Ruvkun, and all members of the Fontana lab for comments and discussions.

Author contributions

Catalina Romero (C.R). and Javier Apfeld (J.A.) designed the research; C.R. performed research; C.R., J.A. and Walter Fontana (W.F.) analyzed data; C.R. wrote the text.
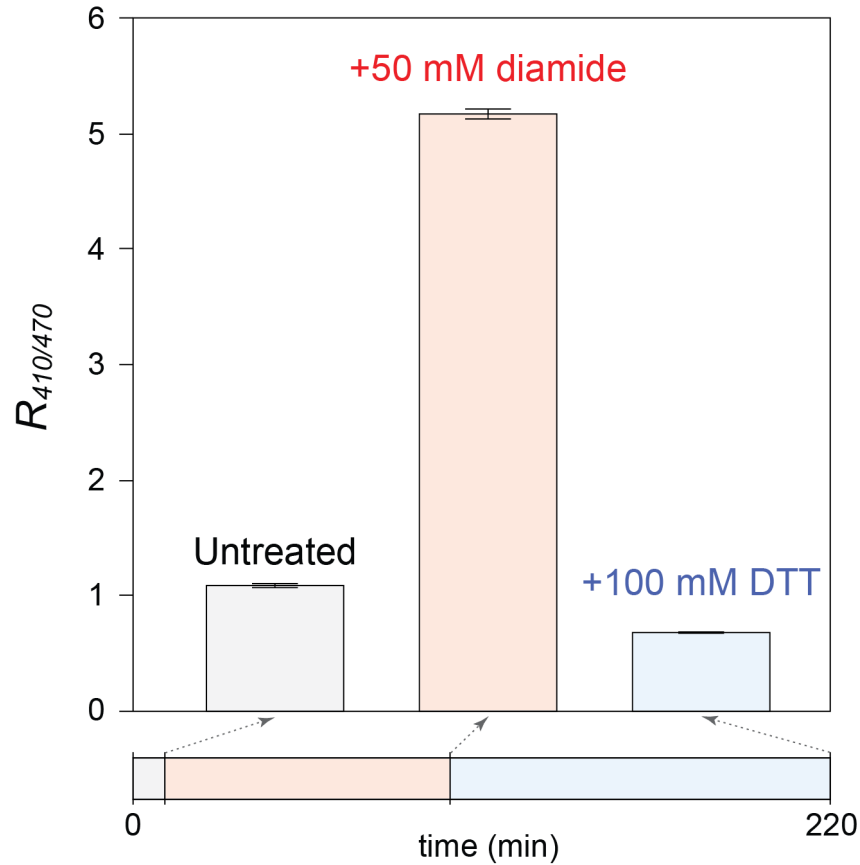
Figure 2.3: Dynamic range and reversible response of roGFP1_R12 *in vivo*. We acquired $R_{410/470}$ time-series in the pharynx of 40 animals being sequential treated with oxidant and reductant agents. Animals were first observed in the absence of treatment, and then treated sequentially with 50 mM diamide for 90 min and 100 mM DTT for 120 min (treatment sequence is schematized by the horizontal bar). Error bars represent the standard error of the mean. Untreated and treatment groups exhibited significant differences in average $R_{410/470}$ ($P < 0.0001$ for all pair-wise comparisons, Tukey HSD test).
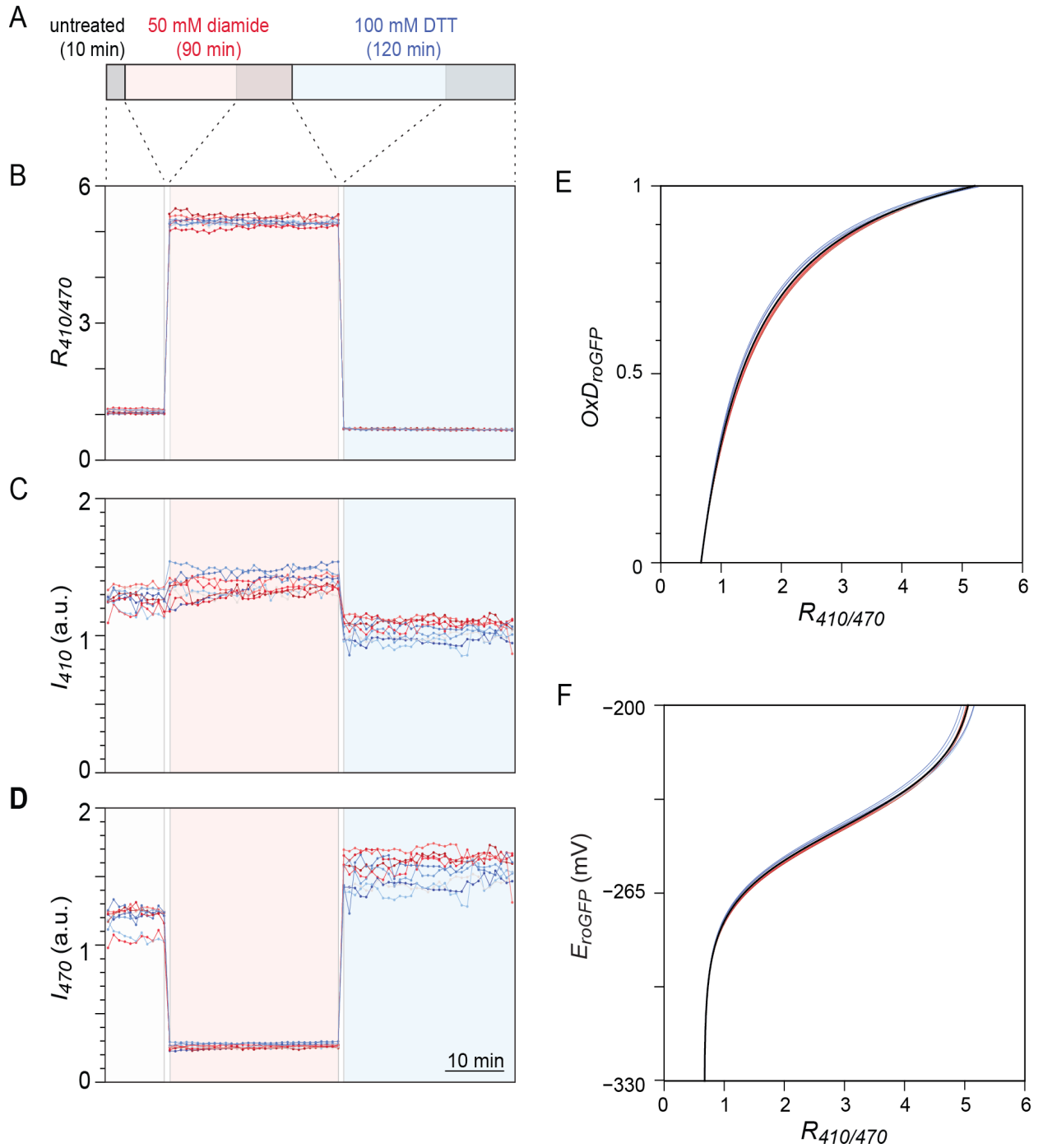
Figure 2.4: Determination of redox potential from ratiometric fluorescence microscopy (A) $R_{410/470}$ time-series acquired in the procorpus muscle group of the pharynx follow the sequence of treatments indicated in the bar. Forty animals were first

(**Figure 2.4** *continued*) observed in the absence of treatment, and then treated

sequentially with 50 mM diamide for 90 min and 100 mM DTT for 120 min. Animals

were imaged for 10 minutes before treatment, and for the last 30 minutes of diamide and

DTT treatments. (B) $R_{410/470}$ time-series for the nine individuals where the sensor was

first maximally oxidized and then maximally reduced, with corresponding fluorescence

intensity traces after illumination with 410 nm light (C) and 470 nm light (D). We note

that the level of fluorescence in each treatment is stable over this time scale. Additionally,

the $R_{410/470}$ values are unaffected by fluctuations in fluorescence intensity due to minor

changes in the focal plane.

(E-F) Relationship between $R_{410/470}$, OxD_{roGFP} and E_{roGFP} values. From each $R_{410/470}$

time-series we determined the three parameters that relate the fraction of roGFP1_R12

molecules with a disulfide bond (OxD_{roGFP}) to $R_{410/470}$ measurements: the value of $R_{410/470}$

when the sensor is fully oxidized (R_{Ox}) and fully reduced (R_{Red}), and the ratio of I_{470}

values when the sensor is fully oxidized versus when it is fully reduced (Instrument

Factor, $IF = I_{470\ Ox} / I_{470\ Red}$). The Nernst equation (*Eq. 3*) was used to calculate E_{roGFP}, the

half-cell reduction potential of the redox couple defined by oxidized and reduced forms

of roGFP1_R12 from OxD_{roGFP}. The relationship between OxD_{roGFP} and $R_{410/470}$ is show

in (E), and (F) presents the relationship between E_{roGFP} and $R_{410/470}$. Curves

corresponding to each animal are shown in color. The curves shown in black represent

the average estimate of R_{Ox}, R_{Red} and IF, and were used throughout this work to calculate

E_{roGFP}.
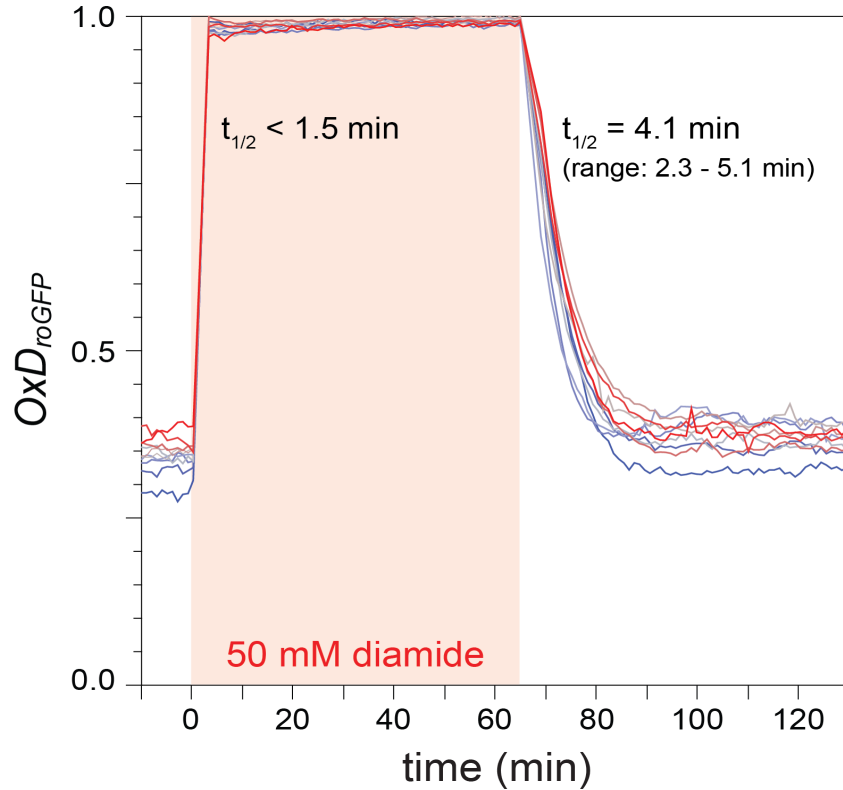
Figure 2.5: *In vivo* kinetics of roGFP1_R12 oxidation and oxidation-recovery.

To examine the sensor's diamide response and recovery kinetics, we acquired OxD_{roGFP} time-series from the procorpus muscles of 10 animals, which were imaged for 10 minutes before treatment, shifted to 50 mM diamide for 60 minutes (shown in red background), and then shifted back to normal conditions for 120 minutes (diamide recovery). Images were acquired once a minute, with gaps of 3 minutes and 4 minutes, respectively, when shifted to and from diamide. Each animal's OxD_{roGFP} time-series is colored by the average value of OxD_{roGFP} before diamide treatment. The average time for a half-maximal response ($t_{1/2}$) is less than 1.5 minutes for diamide treatment, and is 4.1 minutes for recovery from diamide. This experiment also demonstrates that the cytosol of the *C. elegans* feeding muscles can recover quickly and spontaneously from severe oxidative stress, returning to oxidation levels nearly identical to those preceding treatment.
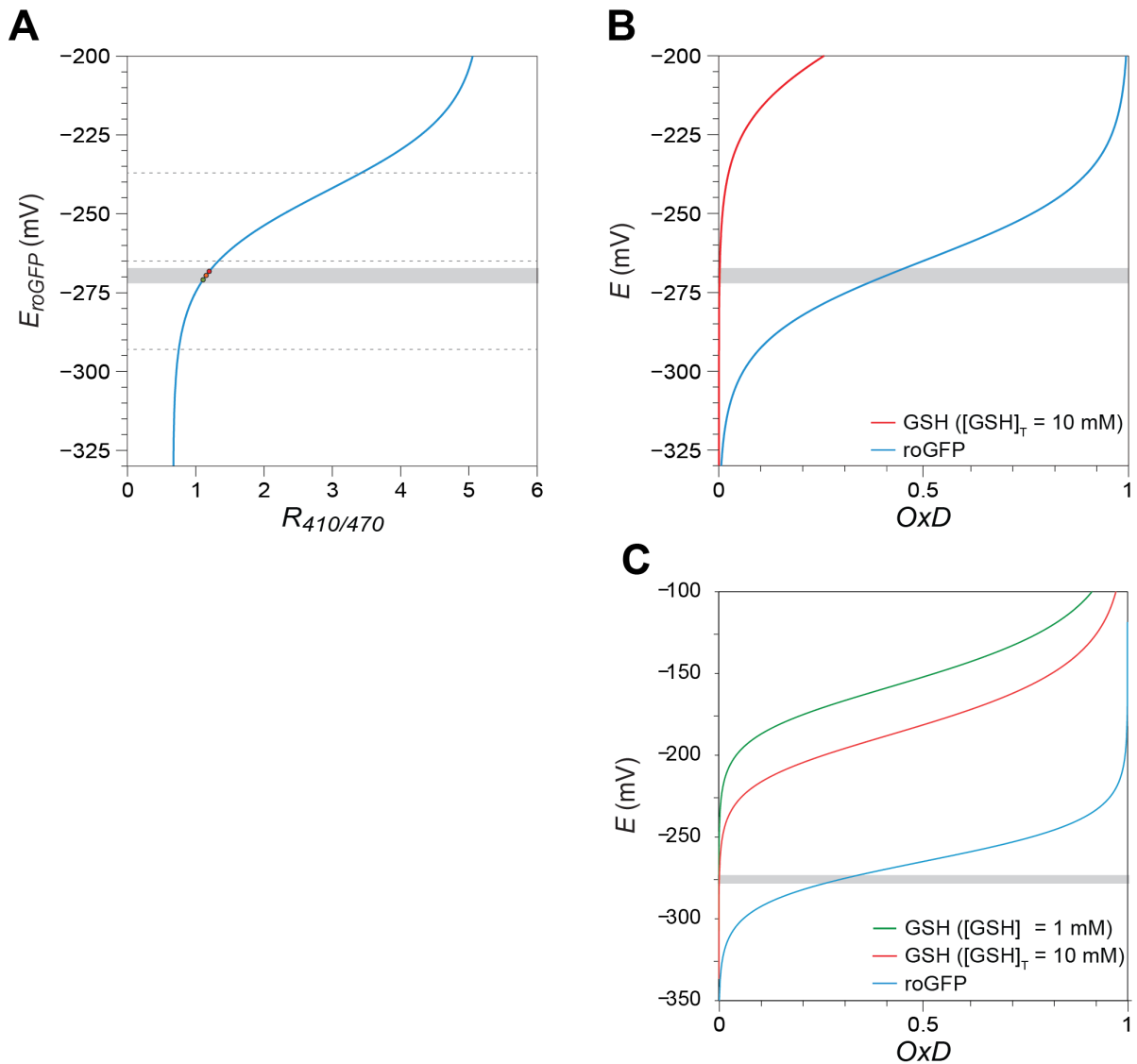
Figure 2.6: Relationship between the sensor and the glutathione redox potentials.

(A) Calculation of cytosolic E_{roGFP} from ratiometric values. The gray area represents the range for the average value of E_{roGFP} measured in wild type, while colored dots represent the average value of E_{roGFP} for the different tissues quantified in this work (see chapter 5): intestine (red), neurons (yellow) and feeding muscles (green). (B-C) Relationship between fraction oxidized (OxD) and potential of the redox couples, defined by the oxidized and reduced form of the sensor, and the glutathione pool. (C) Because the

(**Figure 2.6** *continued)* oxidation of glutathione is a second order reaction, E_{GSH} will depend on total concentration [GSH]$_T$. A 10-times higher concentration of total glutathione will lower the E_{GSH} potential by 30mV.

Chapter 2 – Methods

We built roGFP1_R12 from the vector pPD96_32 (Fire vector kit, Addgene). To generate

roGFP1_R12, we replaced seven residues in this construct (C48S, C65S, S147C, N149K,

S202K, Q204C, F223R) by site-directed mutagenesis (QuickChange, Stratagene). We

used a combination of classical cloning and fusion-PCR to remove the mitochondrial-

targeting sequence in the original plasmid, and to fuse the roGFP1_R12 coding sequence

to specific promoters. The fusion-PCR for the coding region was performed with 12

cycles of amplification to minimize the introduction of sequence errors (Expand High

Fidelity PCR System, Roche), and was cloned into a TOPO BluntII vector. We confirmed

the sequence for all of the injected constructs using DNA sequencing.

We amplified the *myo-2* promoter from pPD80.08 (Fire vector kit, Addgene) with

primers WF45 and WF46, and cloned the PCR product into a TOPO BluntII vector.

roGFP1_R12 was inserted into this vector backbone by restriction with AgeI and

BswiWI, generating *Pmyo-2:: roGFP1_R12*. The plasmid containing *Pmyo-

2::roGFP1_R12* was microinjected using *rol-6(su1006)* as coinjection marker, generating

the exctrachromosomal array *ydEx20*. This array was integrated into the genome by

irradiation with ultraviolet light (254 nm), generating *ydIs1*. After integration the strain

was outcrossed six times to wild type. The list of all the genetic strains used in this work

is presented in Table S1; and the list of primers used in this study are shown in Table S2.

Live fluorescence measurements were done in petri dishes (50 x 9 mm, Falcon). The modified media (NIM, Nematode Imaging Media) does not contain peptone, and contains agarose instead of agar; it also does not contain $CaCl_2$ (to prevent the formation of a precipitate that reduces light transmittance), nor cholesterol and $MgSO_4$ (normally included to support long-term nematode culture, but dispensable in the short time scales required for imaging). To prepare 100 mL of NIM, 2 g agarose and 0.3 g NaCl were dissolved in 96.5 mL of water and melted in a microwave. When the solution cooled to 50 °C, we added 2.5 mL 1 M K_2HPO_4/KH_2PO_4 pH 6.0 and 1 mL levamisole. We poured 7 mL of NIM per petri dish, air dried the plates at room temperature for 1 hour, and then stored them at 4 °C; we used them within two weeks. All of the experiments in this chapter were performed on 1-day-old individuals, which where synchronized by late L4, based in vulva morphology. Before imaging, worms were transferred to NIM plates at room temperature (21-23 °C) for 60 min to ensure immobilization during the time series experiments.

Imaging was conducted on a motorized Axioskop 2 FS plus microscope (Zeiss), using a Plan-Apochromat 10X 0.45 NA 2 mm working distance objective lens (1063-139, Zeiss). Imaging plates were controlled by a motorized stage (ProScan II, Prior) with a stage-mounted customized Petri dish holder. Images were acquired using Metamorph 7.5.3.0 software. All microscopy was performed at 21-23 °C.

roGFP1_R12 is a dual-excitation single-emission ratiometric sensor. Excitation at 410 nm and 470 nm was performed sequentially, with the excitation filters D410/30x and

D470/20x controlled by a high-speed filter changer (Lambda DG-4, Shutter Instrument Company). The filtered light was reflected by a 500dcxr dichroic mirror to illuminate the specimen; the emitted fluorescence passed through the filter HQ535/50m and was detected with a Cool SNAP HQ^2 14-bit camera (Photometrics). All filters were manufactured by Chroma technology Corp. Image processing and segmentation will be explained in the methods section of chapter 3.

We calculated the potential of the redox couple defined by oxidized and reduced forms of roGFP1_R12 using the Nernst equation (Eq. 3), using a standard roGFP1_R12 half-cell reduction potential ($E^{0'}$) of −265 mV (*1*), a cytosolic pH of 7 and a temperature of 22 °C. We note that while the value of E_{roGFP} is influenced by pH (by shifting the midpoint potential of the couple), under physiological conditions these effects are not relevant to understanding the equilibria between the roGFP1_R12 and GSH couple (Meyer & Dick 2010). This is because, under physiological conditions, where pH is well below the pK_a of the reactant thiols (pK_a = 8.92 for GSH and ~9.0 for roGFP1_R12 C147 and C204), the midpoint potentials of these redox couples are affected by pH in the same direction and by essentially the same amount, as they both involve the exchange two protons and two electrons.

Chapter 2 – References

1. Belousov VV, Fradkov AF, Lukyanov KA, Staroverov DB, Shakhbazov KS, et al. (2006) Genetically encoded fluorescent indicator for intracellular hydrogen peroxide. Nat Methods 3: 281-286.

2. Cannon MB, Remington SJ (2006) Re-engineering redox-sensitive green fluorescent protein for improved response rate. Protein Sci 15: 45-57.

3. Dooley CT, Dore TM, Hanson GT, Jackson WC, Remington SJ, et al. (2004) Imaging dynamic redox changes in mammalian cells with green fluorescent protein indicators. J Biol Chem 279: 22284-22293.

4. Fisher-Wellman KH, Neufer PD (2012) Linking mitochondrial bioenergetics to insulin resistance via redox biology. Trends Endocrinol Metab 23: 142-153.

5. Gutscher M, Pauleau AL, Marty L, Brach T, Wabnitz GH, et al. (2008) Real-time imaging of the intracellular glutathione redox potential. Nat Methods 5: 553-559.

6. Gutscher M, Sobotta MC, Wabnitz GH, Ballikaya S, Meyer AJ, et al. (2009) Proximity-based protein thiol oxidation by H2O2-scavenging peroxidases. J Biol Chem 284: 31532-31540.

7. Hanson GT, Aggeler R, Oglesbee D, Cannon M, Capaldi RA, et al. (2004) Investigating mitochondrial redox potential with redox-sensitive green fluorescent protein indicators. J Biol Chem 279: 13044-13053.

8. Herrmann JM, Dick TP (2012) Redox Biology on the rise. Biol Chem 393: 999-1004.

9. Jones DP (2008) Radical-free biology of oxidative stress. Am J Physiol Cell Physiol 295: C849-868.

10. Lukyanov KA, Belousov VV (2013) Genetically encoded fluorescent redox sensors. Biochim Biophys Acta.

11. Meyer AJ, Brach T, Marty L, Kreye S, Rouhier N, et al. (2007) Redox-sensitive GFP in Arabidopsis thaliana is a quantitative biosensor for the redox potential of the cellular glutathione redox buffer. Plant J 52: 973-986.

12. Meyer AJ, Dick TP (2010) Fluorescent protein-based redox probes. Antioxid Redox Signal 13: 621-650.

13. Ostergaard H, Tachibana C, Winther JR (2004) Monitoring disulfide bond formation in the eukaryotic cytosol. J Cell Biol 166: 337-345.

14. Tsien RY (1998) The green fluorescent protein. Annu Rev Biochem 67: 509-544.

15. Wang TA, Yu YV, Govindaiah G, Ye X, Artinian L, et al. (2012) Circadian rhythm of redox state regulates excitability in suprachiasmatic nucleus neurons. Science 337: 839-842.

Chapter 3

Spatial organization of cytosolic redox environment in

the feeding muscle of *C.elegans*

Abstract

Compartmentalization of redox potentials is a universal feature of living systems. While the spatial organization of subcellular redox environments as defined by organelle boundaries is well established; the spatial differences of redox potential at the tissue and organismal scales are not well understood. Below, we show the existence of a tissue-scale pattern of cytosolic redox potential in the pharynx of *C. elegans*. Despite the electrical and physical coupling between the cytosols of feeding muscles, we observe sharp spatial differences in the glutathione pool along the anterior-posterior axis of this tissue. These discrete redox environments align with some, but not all, of the muscle segment boundaries, which suggests that regions with different redox identities exist within a single tissue. We also found that those redox-regions identified at steady state behave as units with different dynamics in response to oxidative stress, and are affected differentially by genetic perturbations. We found that the activity of the insulin receptor oxidizes the glutathione potential in the cytosol of feeding muscles, and that differential regulation of the DAF-16/FOXO transcription factor contributes to the spatial redox pattern of the pharynx.

Chapter 3 – Introduction

To what extent do cells within a tissue coordinate their redox state? Alternatively, to what extent is the redox state of the cytosol an autonomous process determined by the metabolic activity of each cell individually? Gap junctions exist in the majority of metazoan tissues, coupling cellular states such as pH, or concentrations of small metabolites between neighboring cytosols. Furthermore physiological factors, such as endocrine signals or the availability of reducing equivalents based on diet and energy expenditure, are likely to be global variables sensed collectively by the many cells of a tissue. For these reasons, when we began *in vivo* measurements of cytosolic E_{GSH} in *C. elegans*, we expected to observe spatially homogeneous redox potentials at the tissue-level. In the pharynx, the cytosolic redox environment turns out not to be uniform.

In feeding muscles, we observe spatial differentiation of E_{GSH} across the anterior-posterior axis of the pharynx. To our knowledge, this is the first time that an ordered spatial distribution of E_{GSH} at steady state, and across cytosols of connected compartments, has been shown *in vivo*. It stands to reason that these redox regions might be actively maintained and exhibit distinct behaviors. This notion is demonstrated by their differential response to genetic and environmental interventions, as it will be discussed in the second and third part of this chapter.

The pharynx of *C. elegans*

The worm feeds by propelling bacteria into the intestine via a neuromuscular pump called the pharynx. This organ, which is 100 μm long and 20 μm at its widest point, is composed of 60 cells in total: 20 muscle cells, 20 neurons, 4 gland cells, 9 epithelial cells and 7 marginal cells. The pharyngeal muscles (pm) occupy the major part of the organ. Muscle cells are arranged in 8 separate segments (pm1 through pm8), the majority of them composed of 3 radially arranged syncytial cells, and are intercalated with marginal cells (Figure 3.1). Rhythmic contraction of the pharyngeal muscles draws in bacteria in suspension, concentrates them by filtering out liquids, grinds them up, and then passes the debris to the intestine. This cycle is achieved by two types of muscular movements: peristalsis and pumping (Reviewed in Avery and You, 2012; Altun and Hall, 2009).

This organ has 4 regions that are morphologically and functionally distinct: the corpus, formed by the procorpus (pm1 to 3) and metacorpus or anterior bulb (pm4); the isthmus (pm5) and the posterior bulb (pm6 to 8). A pumping cycle starts when the corpus and the posterior bulb contract, opening the pharyngeal channel and drawing in liquids from outside. The muscles then relax, expelling liquid while trapping bacteria in a sieve, which is located in the metacorpus. The isthmus executes a peristaltic movement that moves the bacteria backward; this occurs with a lower frequency than the pumping (once every 3 to 5 pumps). When the bacteria reaches the terminal bulb it is macerated by the grinder, a cuticular structure that serves as the worm's teeth. Finally, the bolus is passed through the intestinal valve, a group of six cells forming a tight cap, connecting the posterior bulb with the intestinal lumen (Altun and Hall, 2009). Besides these contractile properties,

49

pharyngeal muscle cells also exhibit myoepithelial properties: they produce and secrete the specialized cuticle of the pharynx, as will be discussed in detail in Chapter 4.

The pharynx is a surprisingly autonomous system from the rest of the worm. This organ secretes its own cuticle; contains its own muscular system, nervous system, gland cells and structural cells; and is covered by its own basal lamina, separating it from the pseudocoelomic fluid. With the exception of hormonal communication, the two systems seem to operate almost independently (Altun and Hall, 2009). Most surprisingly, this organ can function without nervous input: it continues to pump even after laser ablation of all of its neurons. Of the 20 neurons in the pharynx, 3 of them are particularly important for pumping: MC controls when the contraction starts; M3 controls when the contraction ends; and M4 is necessary and sufficient for normal isthmus peristalsis. The action of only these 3 neurons is enough for the animal to feed normally in laboratory conditions. The other neurons serve to integrate external signals – such as food availability – and internal signals, such as the animal's nutritional status (Avery and Horvitz, 1989; Franks et al., 2006).

Figure 3.1: **The *C. elegans* pharynx** *(following page). Top panel:* DIC microscopy of the tissue, showing the main morphological regions, with associated TEM cross-sections through various regions of the pharynx. *Bottom panel:* schematic arrangement of the 8 pharyngeal muscle cells (pm1-pm8) and the fluorescence image of a transgenic animal expressing a pharyngeal GFP reporter. (Adapted from Altun & Hall, 2009).

B Pharyngeal epithelium

C

D
GI GI
M3 M3
Sieve

E

F
Grinder
pm6

G
Buccal cavity Procorpus Metacorpus Isthmus Terminal bulb
©WormAtlas

pm1
Epithelial cells
I1 neuron
pm6
pm8
A
mc1
mc2
mc3
Nerve cord
pm2
pm3
pm4
pm5
pm6
pm7
©WormAtlas

B
pm3
pm4
pm5
pm6
pm7
*

C
pm6
pm7
pm8
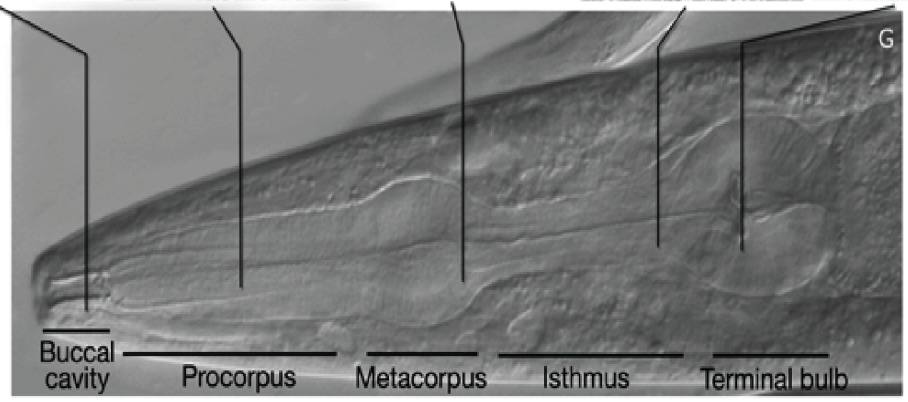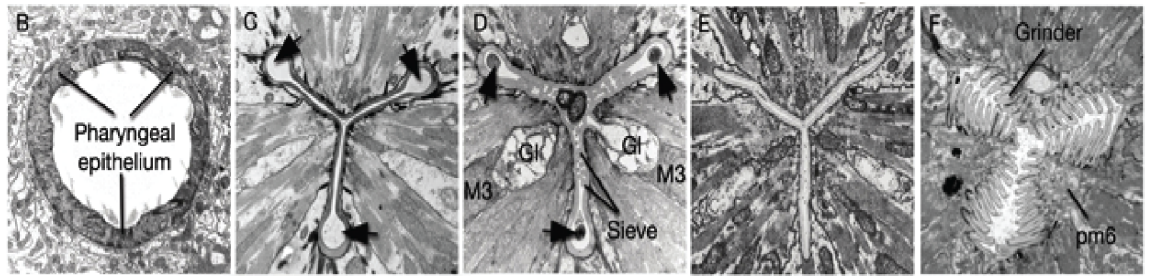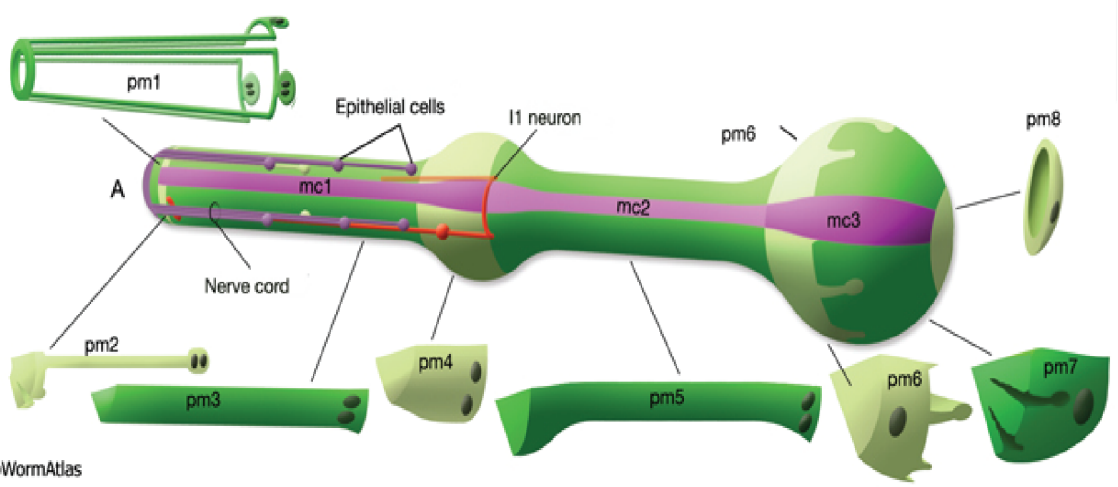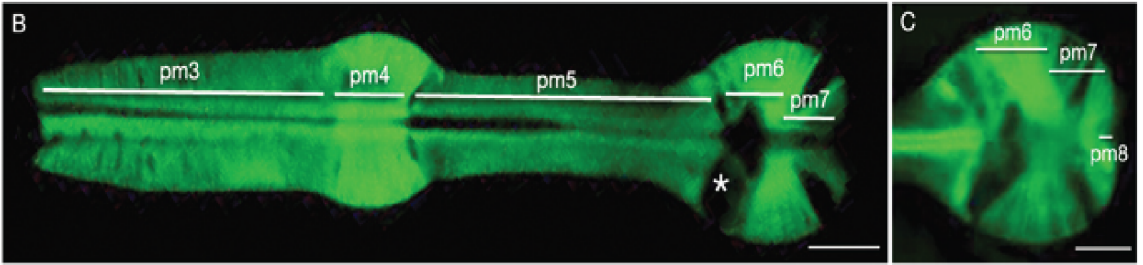
(**Figure 3.1** *continued*)

Gap junctions and their role in pharyngeal muscle contraction

The 20 muscle cells of the pharynx must contract with precise timing to ensure the functionality of this organ. The feeding muscle expresses a complex combinatorial pattern of gap junction proteins, including 9 out of its 25 innexin genes, to create a diverse arrangement of gap junctions. The function of such diversity in connections is still not fully understood (Li et al., 2003), but we do know that some of these junctions electrically couple muscle segments.

Muscle segments have two types of gap junctions: longitudinal, along the anterior-posterior axis, which connects one muscle segment with the next; and lateral, with the intercalated marginal cells, such that the 3 muscle cells within each segment are only connected indirectly through the cytosols of marginal cells. Mutational analysis and vital dye-coupling experiments show that the longitudinal gap junctions, rather than the lateral ones, are the primary route of the electric coupling that coordinates contraction (Altun et al., 2009): gap junctions containing INX-3 are required to coordinate contraction of terminal bulb muscles (Starich et al., 2003); gap junctions containing INX-6 are needed to prevent premature relaxation of procorpus during contraction (Li et al., 2003); and gap junctions containing EAT-5 are required for the coordination of corpus and terminal bulb contraction (Altun et al., 2009). In the last case, it is still unknown how the electrical coupling between the procorpus and the posterior bulb can coordinate the contraction of the two regions without triggering the isthmus contraction.

Gap junctions are a ubiquitous form of intercellular communication, present in almost all metazoan tissue types, with the exception of differentiated skeletal muscles in vertebrates. Despite the divergent sequence in gap junction proteins between vertebrates (connexins) and invertebrates (innexines), they share structural features, such as the conservation of two to three invariant cysteines in the extracellular loop, which might suggest conserved regulatory mechanisms (Panchin et al., 2000). Peptides like glutathione with a molar mass of 307 Da are expected to diffuse freely though gap junctions, which in invertebrates have an exclusion limit of approximately 1000 Da. The extent to which gap junctions in the feeding muscle of *C.elegans* are modulated by chemical or voltage gating is unknown.

Symmetry breaking and pattern formation

The survival of organisms critically depends upon the production and maintenance of ordered structures and patterns, which are intimately related with functional diversification (Li and Bowerman, 2010). Ordered structures at the macroscopic level are often composed by symmetry breaking at smaller scales, where simple interactions of individual parts relying on local information can generate complex levels of organization at a larger scale (Camazine et al., 2001). Consider for example how asymmetries at the level of the cell (cell polarity, or directionality in cell motility) are based upon the molecular asymmetry of the cytoskeleton components (like tubulin and actin). Thus, symmetry breaking is a widespread phenomenon in biology, occurring at all levels of organization: from molecular assemblies, to cell type determination, tissue architecture and body plan axes.

A pattern is an organized arrangement of objects in space or time (Camazine et al., 2001). As opposed to a random arrangement of molecules, these improbable configurations require an investment of energy to maintain the reduction of entropy they entail. In developmental biology the term *pattern* has a more specific meaning, and refers to the process of differentiation and organization of cell types over space and time. In this chapter we will discuss the existence of spatial differences in the redox state of muscle cells across the anterior-posterior axis of the pharynx. Contrary to the homogeneity expected across connected compartments, we find a spatial regularity that is highly consistent between individuals, regardless of the overall oxidation level of the tissue; in other words, we observe a tissue-scale pattern of the glutathione redox potential in the pharynx. This region specificity in cytosolic E_{GSH} raises the question of how cells of the same cell-type with connected cytosols can differentiate their 'redox-identities'.

In the second and third part of this chapter we will examine how the redox-regions identified at steady state exhibits different dynamics under oxidative stress and respond differently to genetic manipulation. The consistencies in the spatial boundaries defining regions with different redox behaviors under those other conditions make us think that the cell is actively producing and maintaining these redox differences between regions. It is unknown to us what are the functional consequences of this asymmetry in the redox environment for the tissue, and how this serves an adaptative role to have evolved and to be, at least partially, under genetic control.

Chapter 3 – Results

Tissue-scale pattern of cytosolic redox environment in the feeding muscle of

C.elegans

To probe the variability of the cytosolic redox environment, we decided to measure the glutathione redox potential in pharyngeal muscles. The linear arrangement of this cylindrical organ, and the large size of its muscle cells, grant enough spatial resolution to discriminate between muscle segments (Figure 3.2A). We quantified E_{GSH} in different muscles belonging to the four morphological regions of the pharynx: the procorpus (*PC*), the metacorpus (*MC*), the isthmus (*I*) and the posterior bulb (*PB*). In Figure 3.3 we show the redox potential profiles along the anterior-posterior axis of the pharynx for 394 wild-type individuals – traces are colored based on their average value. In panel 3.2B we show the color map for the same population, where each horizontal line represents the E_{GSH} profile of a wild-type individual, arranged in decreasing order of average redox potential.

First we observe that isogenic populations of synchronized 2-day-old adults exhibit a wide variation in the glutathione redox potential between individuals, with differences of up to 11mV (Figure 3.3). While the E_{GSH} observed in each muscle segment varies widely between individuals (Figure 3.2C and 3.3), there is a strong correlation between the E_{GSH} of the muscles segments within the pharynx (Figure 3.4). This evidence suggests that there is a common mechanism determining the overall redox potential at the tissue level. These spatial correlations of redox potentials are not surprising: given that adjacent

55

muscles are connected via gap junctions, as shown by dye diffusion and electric coupling (Altun et al., 2009), it is expected they exchange oxidants and reductants.

It is surprising, however, to find discrete redox environments within this series of connected cytosols. The glutathione redox potential is generally lower in the procorpus (*PC*) than in the isthmus (*I*) muscles, and is highest in the posterior bulb (*PB*) muscles (Figures 3.2 and 3.3 and Table 3.1). These anterior-posterior differences are not part of a gradient: we observe a sharp transition in the redox state between the metacorpus and the isthmus, and between the isthmus and the posterior bulb. These well-defined, discrete redox regions are readily visualized upon removing the average redox potential of each pharynx from the anterior-posterior pharyngeal redox profiles (Figures 3.2D).

Next we asked about the difference in potential between pairs of muscle segments within the pharynx. In other words, what current would be observed if an alternate route for the equilibration of potentials were provided? We can think of this difference in potential as the amount of energy stored in the spatial pattern: between procorpus and posterior bulb we observe average $\Delta E_{PC\text{-}PB}$ of -3.1 mV, with up to -7.5 mV differences between muscles of the same pharynx (Figure 3.2E); between procorpus and isthmus we observe average $\Delta E_{PC\text{-}I}$ of -1.8 mV, with a maximal difference of -4.8 mV; and between procorpus and metacorpus we observe average $\Delta E_{PC\text{-}MC}$ of -0.2 mV. This last comparison sets a reference for the expected magnitude of ΔE between what we consider to be undifferentiated regions (Figure 3.2C and E).

When we compare the delta between procorpus and isthmus ($\Delta E_{PC\text{-}I}$) with the delta between isthmus and posterior bulb ($\Delta E_{I\text{-}PB}$) within each individual, we observe that they vary independently, suggesting that multiple, independent determinants give rise to this regional variability in redox potential (Figure 3.5).

We notice that spatial differences in redox potential are present, regardless of the average E_{GSH}. To illustrate the occurrence of large redox potential differences between pharyngeal muscles, in individuals spanning all levels of overall oxidation, we focused on a subpopulation of worms where the difference between procorpus and isthmus was at least 3.4 mV (Figure 3.6B, shaded area). From those, we selected seven individuals that were spaced at equal intervals between the minimum and maximum average redox potential along the medial axis of the pharynx ($\bar{E}$) (Figure 3.6A black dots). The three columns in panel C show how the overall E_{GSH} level for the whole tissue varies, while the features of the profile remain consistent. The magnitude of the difference in potential between regions also varies (Figure 3.2E). To illustrate this variability between procorpus and isthmus muscles, we selected seven individuals spaced at equal intervals between the minimum and maximum redox potential difference for those two muscles (Figure 3.7A, black dots). In Figure 3.7 we plot the anterior-posterior profile for this individuals.

In summary, our study shows that the cytosolic redox environment within the feeding organ of *C. elegans* is spatially structured. This discovery raises questions: how are these differences in redox potential established? Are they a passive consequence of the properties of the tissue, or does the cell actively maintain these differences? Given the order of these muscle-specific differences in E_{GSH}, it is unlikely they are related to each

muscle's rate of contraction. During pumping, the metacorpus and terminal bulb contract synchronously, experiencing the same frequency of movement; yet the two regions show different steady-state levels of E_{GSH}. In contrast, peristalsis occurs every 3 to 5 pumps, so the isthmus contracts less frequently than the metacorpus and the posterior bulb; yet this region has higher levels of E_{GSH} than the procorpus, and lower levels of E_{GSH} than the posterior bulb. Neither do we consider these spatial differences to be related to the shape or mechanical properties of the tissue. For instance, procorpus and metacorpus have indistinguishable E_{GSH} levels, yet they differ in size, shape, aspect ratio, direction of muscle filaments and channel diameter when open, among other parameters.

In Chapter 4, we discuss how this spatial distribution of E_{GSH} changes, both in postembryonic development and during adulthood: 10-day-old *daf-2(e1370)* mutants, for example, exhibit higher E_{GSH} in the procorpus than in the isthmus and the posterior bulb, proving that the polarity of the pattern can revert. Thus, the spatial differences in E_{GSH} are not invariant over time, nor intrinsic to the pharynx, so we do not think they are a passive consequence of the shape of the tissue. The fact that these redox-regions exhibit distinct behaviors under environmental (Part 2) and genetic (Part 3) perturbations supports the notion that cellular mechanisms actively maintain their redox-identity.
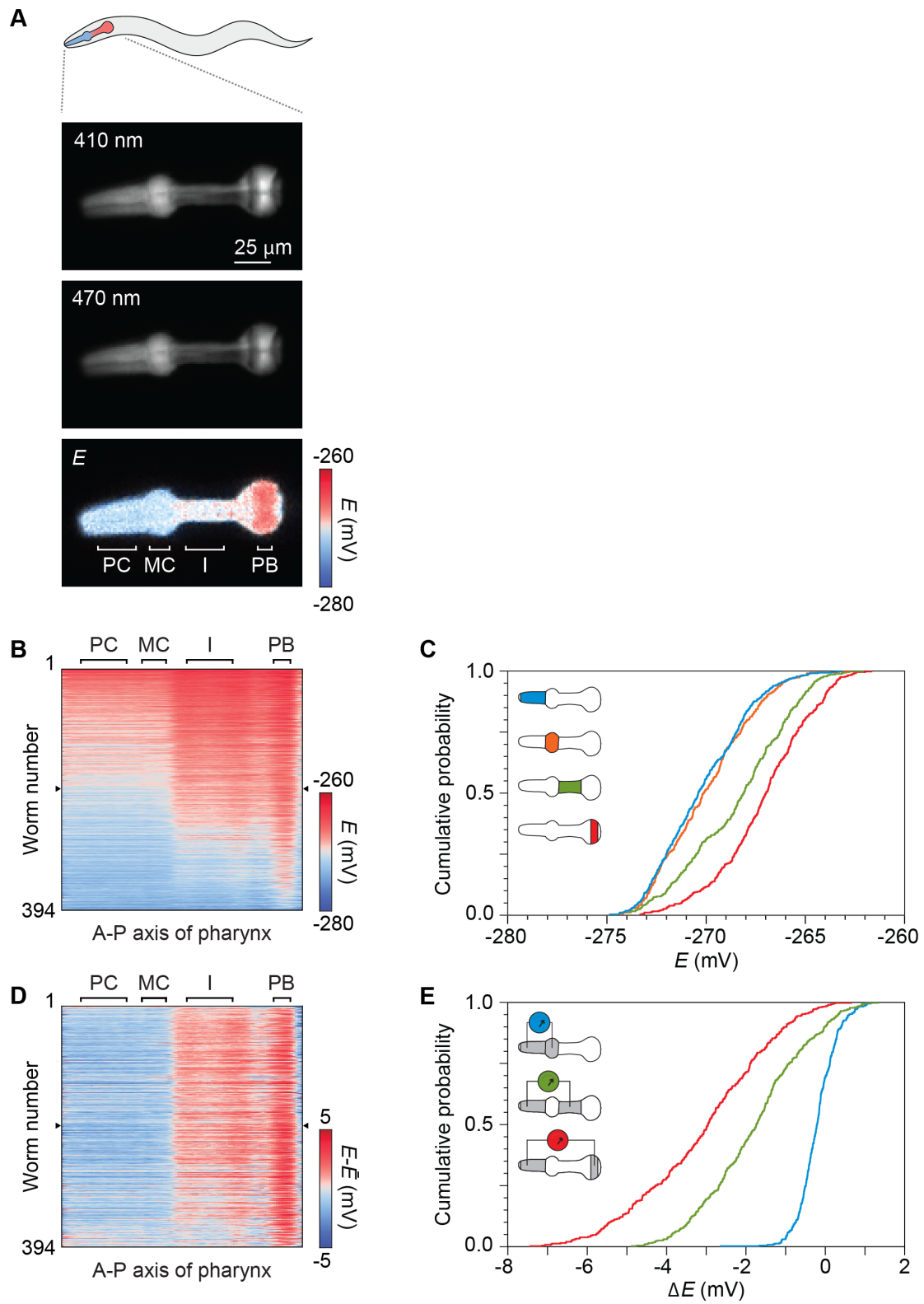
Figure 3.2: Spatial differences of the cytosolic redox environment in feeding

muscles. (A) Fluorescence images of animals expressing roGFP1_R12 in the muscles

(**Figure 3.2** *continued*) of the pharynx after illumination with 410 and 470 nm light. Visualization of the pixel-by-pixel redox potential E is derived from these images. Brackets denote the boundaries used to quantify the redox potential of specific muscle groups: PC is the procorpus, MC the metacorpus, I is the isthmus, and PB is the posterior bulb.

(B) Anterior-posterior differences in redox potential of feeding muscles. Each horizontal line represents the redox profile of a wild-type individual along the anterior-posterior axis of its pharynx (n=394). The profiles are sorted by their average, from highest (top) to lowest (bottom). Arrows denote the profile of the representative individual in panel A.

(C) Cumulative distributions[9] of E values for the four muscle groups is shown. For statistics see Table 3.1.

(D) Average-normalized redox profiles. Redox profiles are sorted in the same order as in panel B, but with their average values subtracted. Arrows denote the profile of the individual in panel A.

(E) Cumulative distributions of the potential difference between pairs of muscle pairs. For statistics see Table 3.2

---

[9] We plot our results as cumulative distributions (defined as the likelihood that E is less than or equal to the value in the x-axis) because it readily allows comparison between several distributions within a single panel.
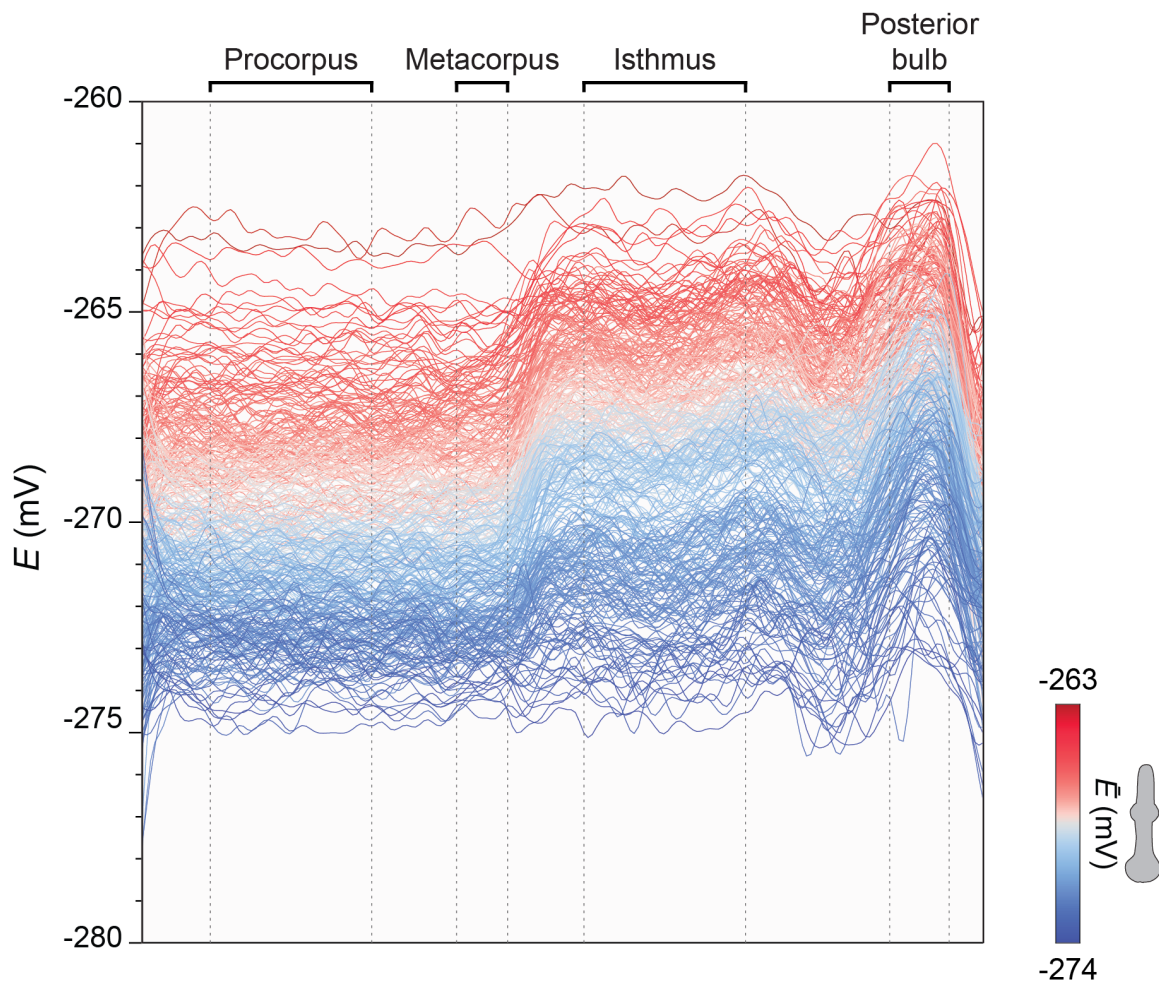
Figure 3.3: Redox profiles across the anterior-posterior axis of the pharynx.

Profiles of E for each of the 394 wild-type animals shown in Figure 3.2. Each profile is the best-fit functional representation of the observed E values using a B-spline basis (see methods). Profiles are colored based on their average value ($\bar{E}$). Boundaries used for measurements of each pharyngeal muscle segment are denoted by brackets. For statistics see Table 3.1

61
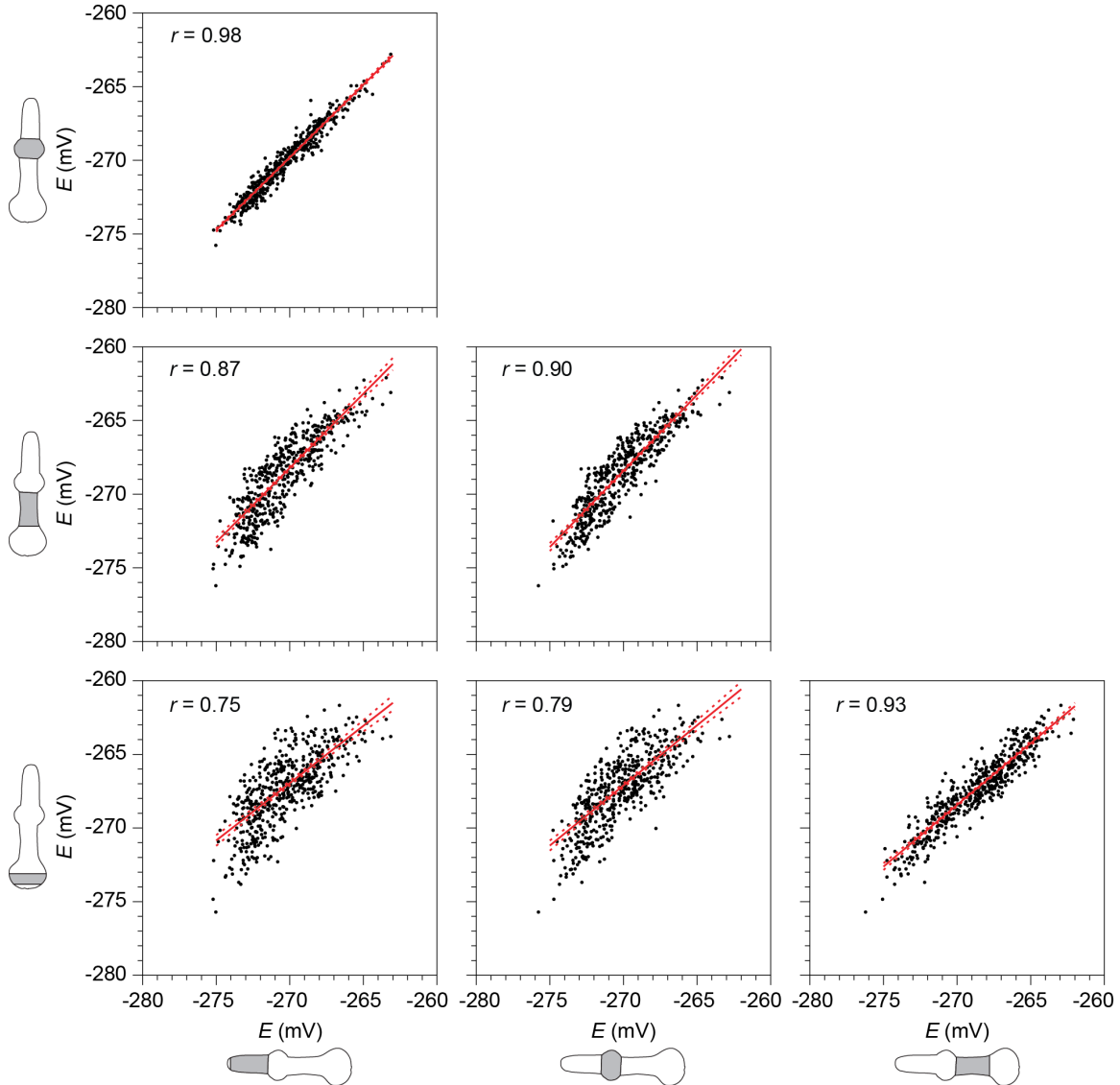
Figure 3.4: Correlations between the redox potentials of pharyngeal muscles.

Scatter-plot matrix of E values in procorpus, isthmus and posterior bulb muscles. The diagrams depict the muscles plotted in the ordinate and abscissa. Linear regression best-fits are shown as solid lines, bounded by dashed lines denoting the 95% confidence interval of the fit. The statistical significance of each correlation coefficient (r, top left) is denoted in red for $P < 0.0001$.
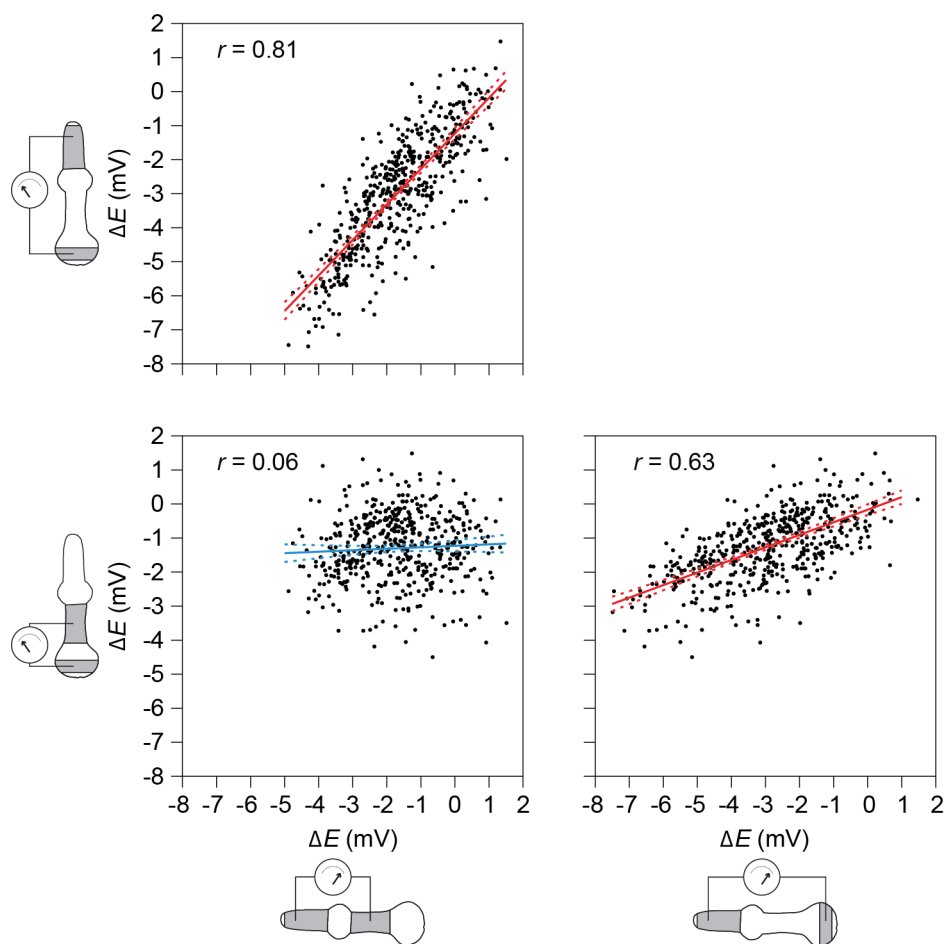
Figure 3.5: **Correlations between the redox potential-differences of pharyngeal muscle pairs.** Scatter-plot matrix of ΔE values between pairs of pharyngeal muscles. The diagrams depict the muscle pairs used to calculate the ΔE values plotted in the ordinate and abscissa. Linear regression best-fits are shown as solid lines bounded by dashed lines denoting the 95% confidence interval of the fit. The statistical significance of each correlation coefficient (r, top left) is denoted in red for $P < 0.0001$ and blue for $P > 0.05$.
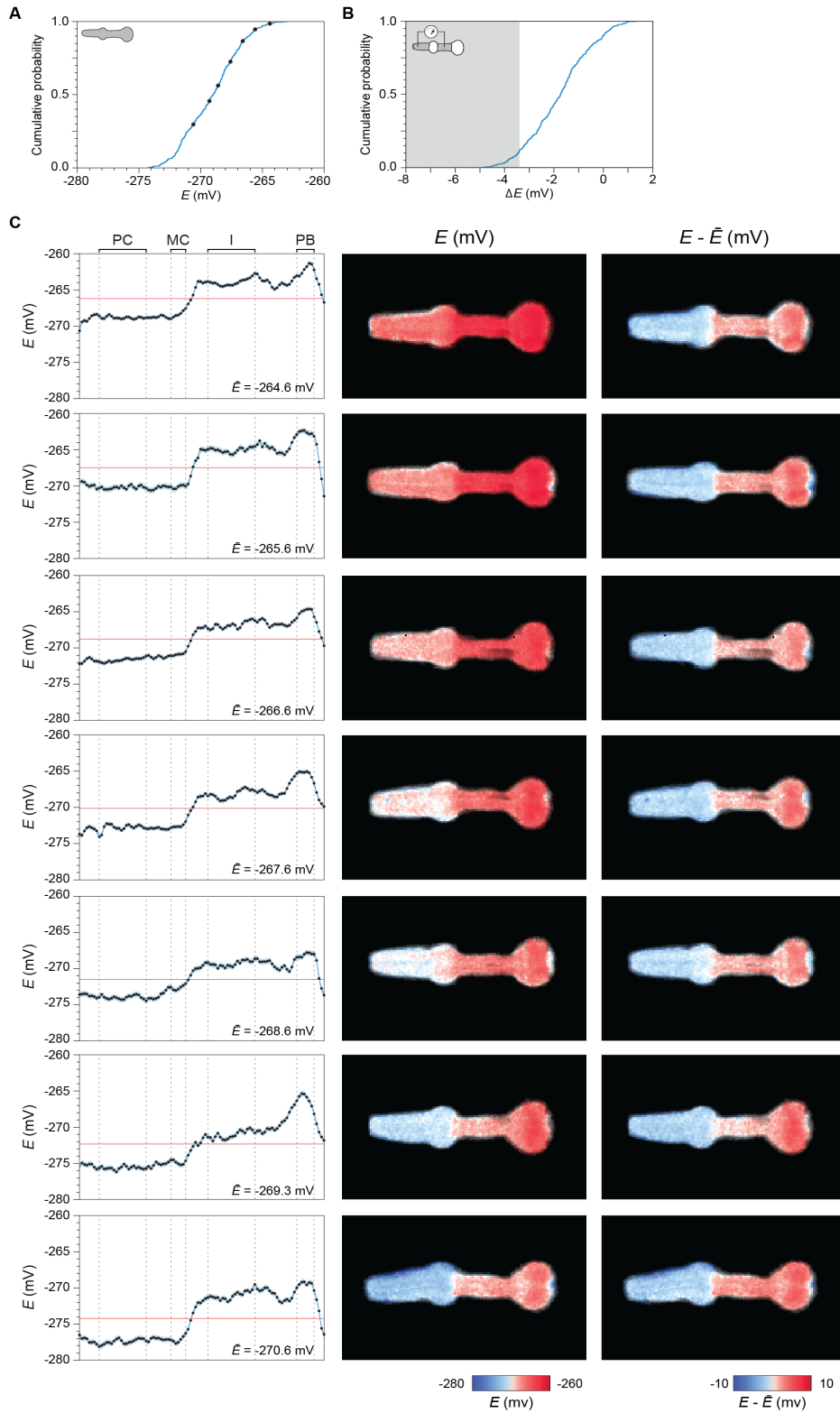
Figure 3.6: Spatial differences in redox potential over all levels of pharyngeal muscle oxidation. Spatial differences in redox potential occur in animals over all

(**Figure 3.6** *continued*) levels of pharyngeal muscle oxidation**.** (A-B) To illustrate this point, we selected seven animals spaced at equal intervals along the medial axis of the pharynx, between the minimum and maximum average redox potential ($\bar{E}$) (panel **A**, black dots); we chose them from animals whose potential difference between procorpus and isthmus muscles was lower than 3.4 mV (panel B, shaded area). (C) Each row represents one of the selected animals, and contains three panels:

Panel 1: Profile of pharyngeal muscle E along the anterior-posterior axis of the pharynx. The profile (blue line) is the best-fit functional representation of the observed E values (black dots) using a B-spline basis. The shaded area denotes the point-wise 95% confidence interval for the fit. The red line denotes the average value, $\bar{E}$. Boundaries used for the measurement of each pharyngeal muscle group are indicated by brackets.

Panel 2: Image of the pharynx colored based on the pixel-by-pixel value of E.

Panel 3: Image of the pharynx colored based on the pixel-by-pixel value of $E - \bar{E}$

Figure 3.7: Variability of the differences in redox potential along the pharynx. (*following page*). (A) To illustrate the variability of the redox potential differences between procorpus and isthmus muscles, we selected seven animals among the 394 wild-type animals shown in Figure 3.2E. These animals were spaced at equal intervals between the minimum and maximum redox potential difference for those muscles (panel **A**, black dots). (B) Each row contains two panels for each of the selected animals:

<u>*Panel 1*</u>: Average subtracted profile ($E - \bar{E}$) along the anterior-posterior axis of the pharynx. The profile (blue line) is the best-fit functional representation of the observed E values (black dots) using a B-spline basis. The shaded area denotes the point-wise 95% confidence interval for the fit. ΔE is labeled to the bottom right. Boundaries used for measurements of each pharyngeal muscle group are denoted by brackets.

<u>*Panel 2*</u>: Image of the pharynx, colored based on the pixel-by-pixel value of $E - \bar{E}$.

(**Figure 3.7** *continued*)

67

Chapter 3 – Results

Spatio-temporal dynamics in the response to oxidative stress

The notion of a redox-region is further supported by the dynamic response to oxidative

insult. We recorded time series of 64 individual animals before and after shifting them to

plates containing 5 mM of the oxidant tert-butyl hydroperoxide (t-BuOOH); during

oxidative insult we observe that the cells of the tissue do not respond in unison. Figure

3.8A shows a representative kymograph, illustrating the spatio-temporal changes

observed in E_{roGFP} in the first hour of response[10]. The key observation here is that we

discern spatial boundaries delimiting regions with different dynamics of response (Figure

3.8 and 3.9), and those spatial boundaries coincide with the redox regions observed in

baseline conditions (*PC, I, PB*).

To obtain the average redox dynamics for each region, we performed a functional

regression, by first converting the traces into functions using a spline basis. Because we

wanted to analyze the dynamics of response independently of the initial differences

between individuals or between regions, we baseline-corrected each individual trace

(Figure 3.9). Functional regression of these E_{roGFP} traces indicates that the redox

environment of procorpus, isthmus and posterior bulb muscles exhibit distinct dynamics

(Figure 3.8B). This analysis, however, does not give us information about the modes of

---

[10] After 1h in 5-mM *t*BuOOH all individuals survive. A similar dose (6-mM *t*BuOOH)
kills half of the population in approximately 18 h (Stroustrup et al., 2013)

variation between the responses of different individuals, masking the considerable variability that exists between individual traces (Figure 3.9).

To investigate the modes of variation, we focused on the traces in the *PB* muscles: we identified the dimensions underlying this variation using functional principal component analysis (Figure 3.8). The major modes of variation between individuals are: *i)* time-dependent differences in overall response amplitude; *ii*) the timing of the oxidative peak and the attainment of a new steady-state; and *iii*) the magnitude and breadth of that peak.

This analysis also shows the extent to which baseline potentials (measured prior to oxidant exposure) can predict specific features in the response to oxidative insult (Figure 3.10).

Figure 3.8: spatio-temporal dynamics in response to oxidative stress.

(following page). We acquired E_{roGFP} time-series of the procorpus, isthmus and posterior bulb of 64 animals before and after oxidant treatment, tracked individually. These animals were observed in the absence of treatment for 10 minutes, and then treated with 5 mM *tert*-butyl hydroperoxide (*t*-BuOOH). Images were acquired every 30 seconds with a 6 minute gap between treatments. This treatment sequence is denoted by the diagram below each plot.

(A) Representative kymograph of a single individual, showing the spatial and temporal response of the E_{roGFP} to treatment with the oxidant t-BuOOH. Each column represents the redox profile of the individual along the anterior-posterior axis of its pharynx at a specific time (30 sec acquisition rate for 1 h). Brackets denote the boundaries utilized to quantify redox potential of specific muscle groups: PC – procorpus, MC – metacorpus, I – isthmus, and PB – posterior bulb.

(B) Muscles exhibit different dynamic response to oxidant treatment: functional regression of the effect of each muscle group. The lines denote the average response of the cytosolic potential of each muscle group as a function of time, minus the average potential of the muscle before oxidant treatment ($E(t) – E_b$) in 64 individuals. Shaded areas denote the 68% point-wise confidence interval (1 SD from the mean) of $E(t) – E_b$ for each muscle group.
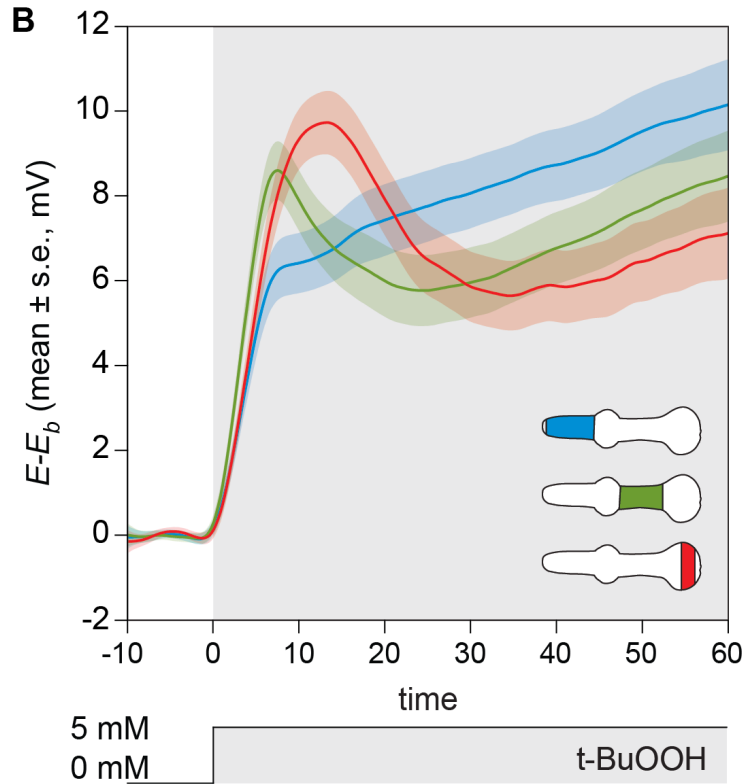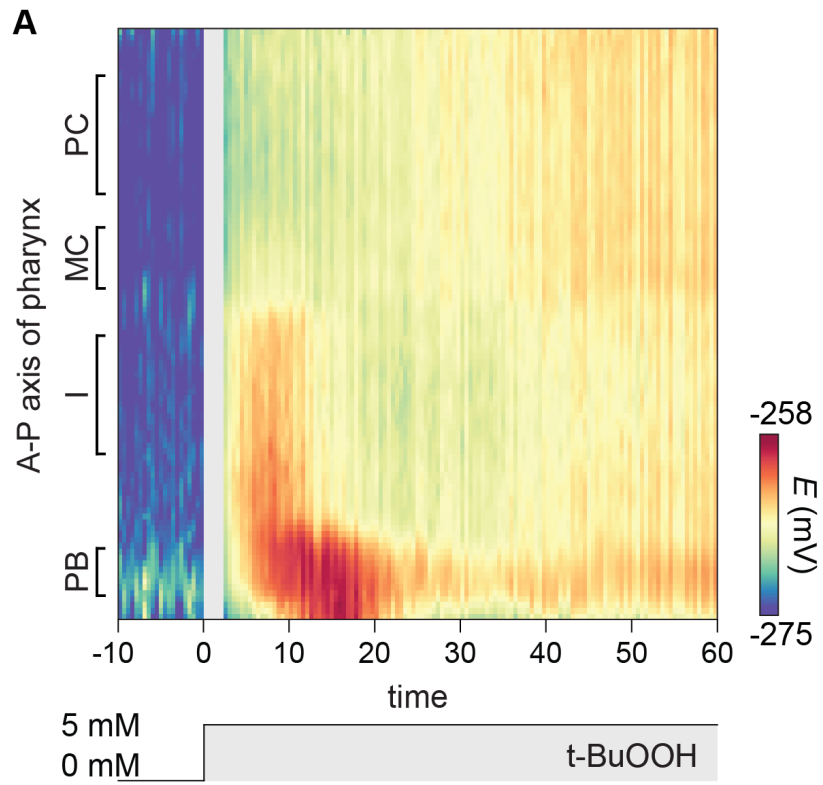
(**Figure 3.8** *continued*)

71
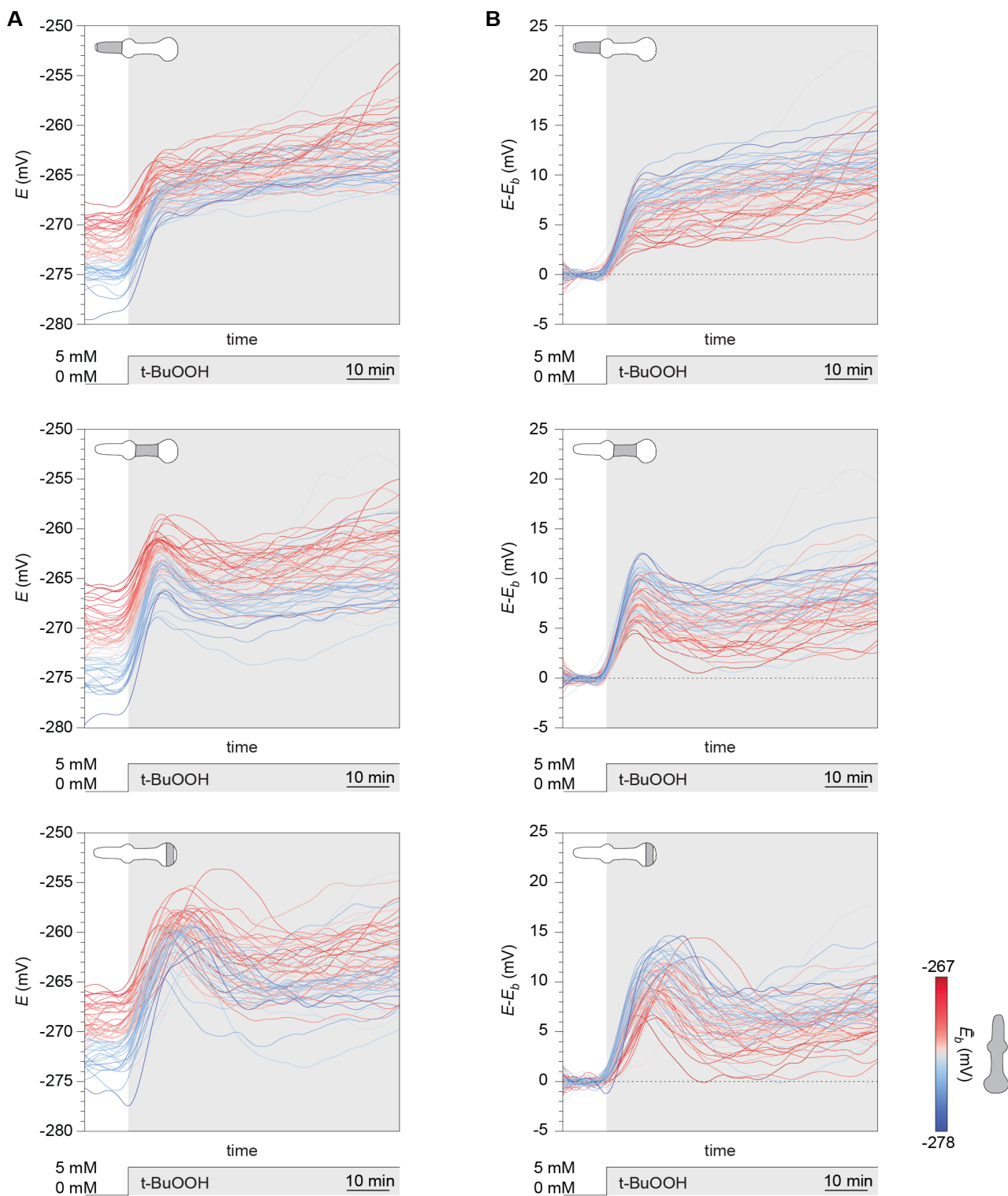
Figure 3.9: Individual variability in the response to oxidative stress. (A) Temporal E

(**Figure 3.9** *continued*) dynamics. The diagram in the top left depicts the observed muscles. Each curve is the best-fit functional representation of the observed $E(t)$ values using a B-spline basis. Curves are colored based on the average value of the redox potential in baseline conditions (E_b). (B) Temporal $E(t) – E_b$ dynamics. Trajectories in panel (A) where baseline-normalized by subtracting the E_b value per region.

Figure 3.10: Modes of variation in the response to oxidative stress. *(following page)*

(A) Individual baseline-subtracted traces ($E(t) – E_b$) exhibit considerable variation in their dynamic response to exogenous oxidants, independently of the initial baseline variability. (B-D) We perform functional principal components analysis (fPCA) on the traces for posterior bulb PB shown in panel (A). The three major axes of variation correspond to: *i)* response amplitude; *ii)* timing of the oxidative peak and the attainment of a new steady-state; and *iii)* the magnitude and breadth of that peak.

(E-G) Scatter-plot of the initial value of baseline, E_b, and the score for each principal component. Linear regression best-fits are shown as solid lines bounded by dashed lines denoting the 95% confidence interval of the fit. The statistical significance for each correlation coefficient (r, top left) is denoted in red for $P < 0.05$ and blue for $P > 0.05$.

A
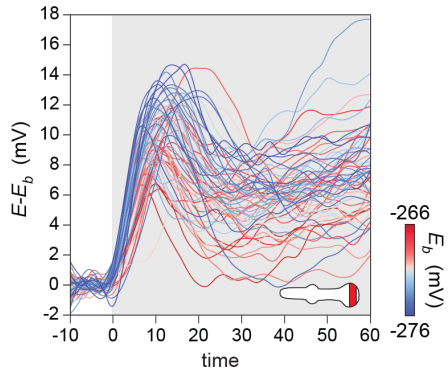
B PC function 1
(accounts for 56% of $E\text{-}E_b$ variance)
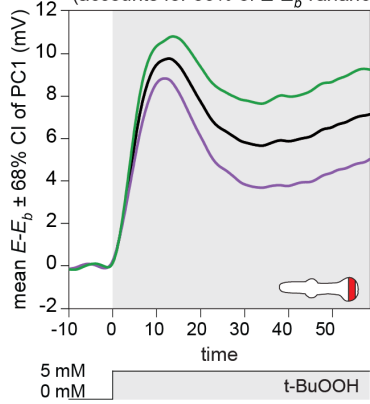
C PC function 2
(accounts for 27% of $E\text{-}E_b$ variance)
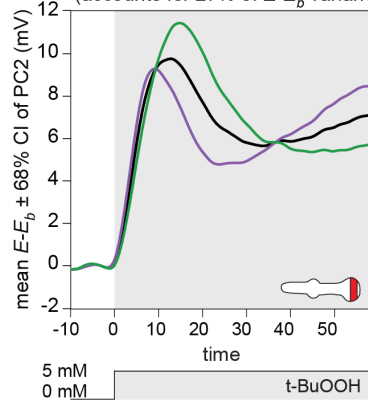
D PC function 3
(accounts for 9% of $E\text{-}E_b$ variance)

E $r = -0.35$, $p = 0.011$

F $r = -0.26$, $p = 0.11$

G $r = -0.38$, $p = 0.006$
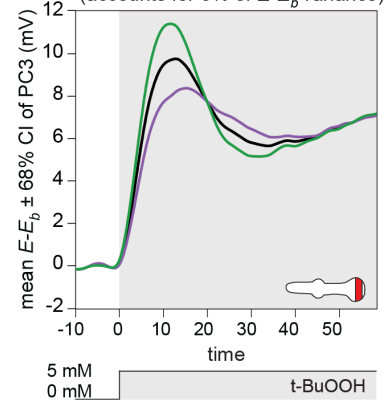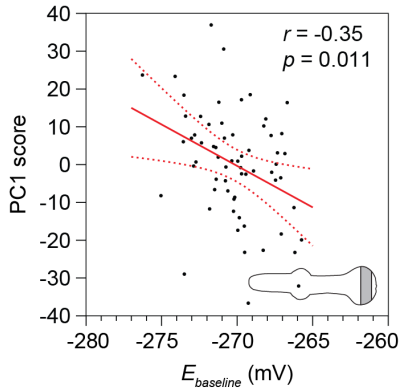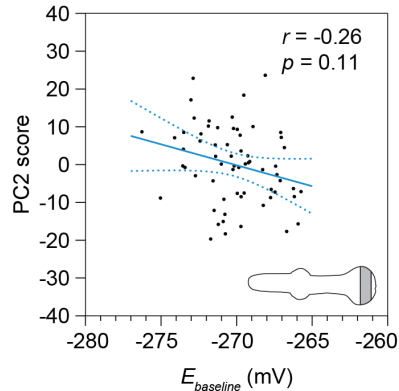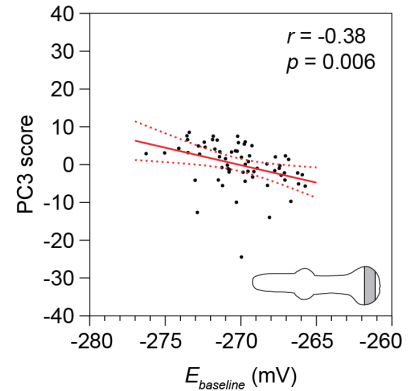
(**Figure 3.10** *continued*)

Chapter 3 – Results

Region-specific effects of insulin signaling in the feeding muscle redox environment

To explore the possibility that spatial differences in the glutathione pool are actively

maintained, we investigated the role of insulin/IGF-1 signaling. Beside its role in the

regulation of energy metabolism, this pathway has evolutionarily conserved effects on

survival under oxidative stress and aging. *C. elegans* has only one insulin/IGF-1 receptor

gene, *daf-2*, whose reduction of function by mutation can more than double lifespan

(Kenyon et al, 1993) and survival upon exposure to environmental oxidants (Tullet et al.,

2008). The *daf-2(e1370)* allele, which affects the kinase domain of the receptor and leads

to a strong loss of function, lowers E_{GSH} in all pharyngeal regions, by an average of 2.4 to

3.1 mV depending on the muscle (Figure 3.11 and Table 3.3). Another mutation, *daf-*

2(m579), which affects the ligand binding domain of the receptor and causes type A

insulin resistance in humans (Hamer et al., 2002; Patel et al., 2008), yields a similar effect

(Figure 3.12 and Table 3.4). Thus, in wild-type animals, the redox potential of the

glutathione pool is influenced by the oxidizing action of the DAF-2 receptor. The fact

that the activity of the insulin receptor, a major control node in the regulation of energy

homeostasis, has an oxidizing effect in the glutathione pool is in agreement with the

hypothetic coupling between metabolism and the redox cytosolic environment. This

perspective supports the notion of E_{GSH} as being an integrative variable that is responding

to metabolic changes, rather than a buffering system that by definition should be stable

and unresponsive.

Next, we investigated whether insulin/IGF-1 signaling specifies the E_{GSH} differences between muscles. The FOXO transcription factor DAF-16 mediates the effects of signaling by DAF-2 on survival (Kenyon et al., 1993) and oxidative conditions (Honda and Honda, 1999; Tullet et al., 2008). We found the same to hold for the pharyngeal redox potential: *i*) E_{GSH} in *daf-16(mu86); daf-2(e1370)* double mutants is indistinguishable from that of *daf-16(m86)* mutants (Figure 3.11); *ii*) and restoring expression of *daf-16(+)* exclusively in pharyngeal muscle of *daf-16(mu86); daf-2(e1370)* is sufficient to lower E_{GSH} in all pharyngeal regions (Figure 3.13 and Table 3.5).

The key observation is that in *daf-16(mu86)* null mutants, we observe a region-dependent effect: E_{GSH} oxidation levels are higher than wild type in procorpus and isthmus muscles, but are indistinguishable from wild type in posterior bulb (Figure 3.11). This result indicates that DAF-16 is normally active in procorpus and isthmus muscles, but is kept inactive by DAF-2 in posterior bulb muscles. We conclude that insulin signaling quantitatively affects different muscle regions by the differential regulation of DAF-16, thus contributing to the spatial redox pattern of the pharynx.

Acknowledgements

Author contributions

Catalina Romero (C.R), Javier Apfeld (J.A.) and Walter Fontana (W.F.) designed research; C.R. performed research; C.R., J.A. and W.F. analyzed data; C.R. wrote the manuscript.
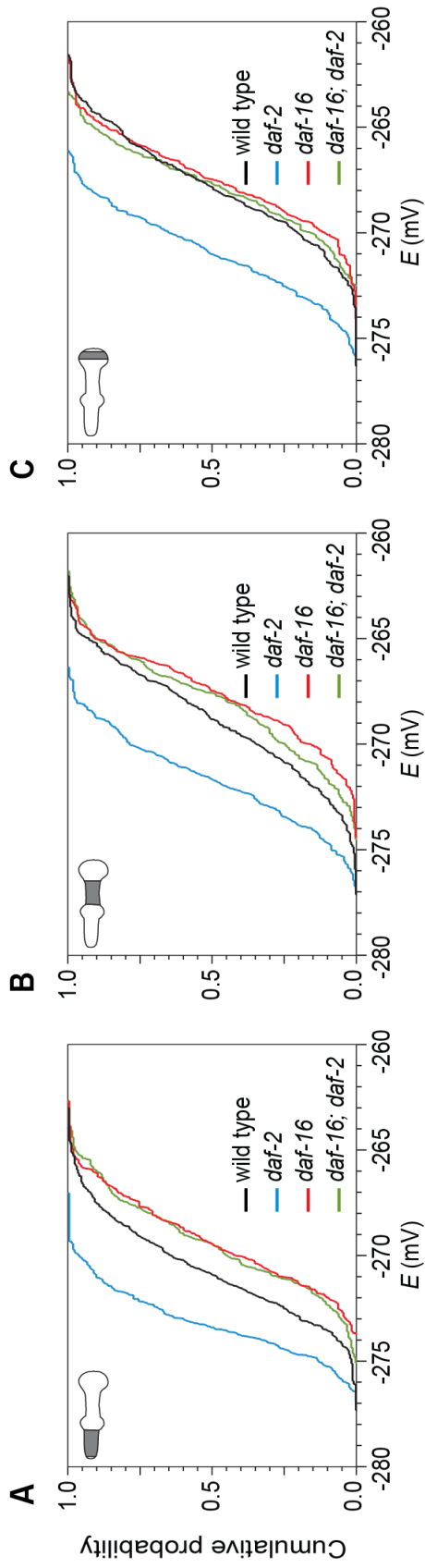
Figure 3.11: Insulin signaling has region-specific effects on the redox potential of feeding muscles. (A–C) *daf-2(e1370)* mutants exhibit lower cytosolic E_{GSH} in all feeding muscles compared to wild type. This effect is dependent on the FOXO/DAF-16 transcription factor: E_{GSH} in *daf-16(mu86); daf-2(e1370)* double mutants is indistinguishable from that of *daf-16(m86)* single mutants in all muscle segments examined. Compared to wild type *daf-16(mu86)* mutants have a more oxidizing cytosolic E in procorpus and isthmus (A-B), but not in posterior-bulb muscles (C). For statistics see Table 3.3
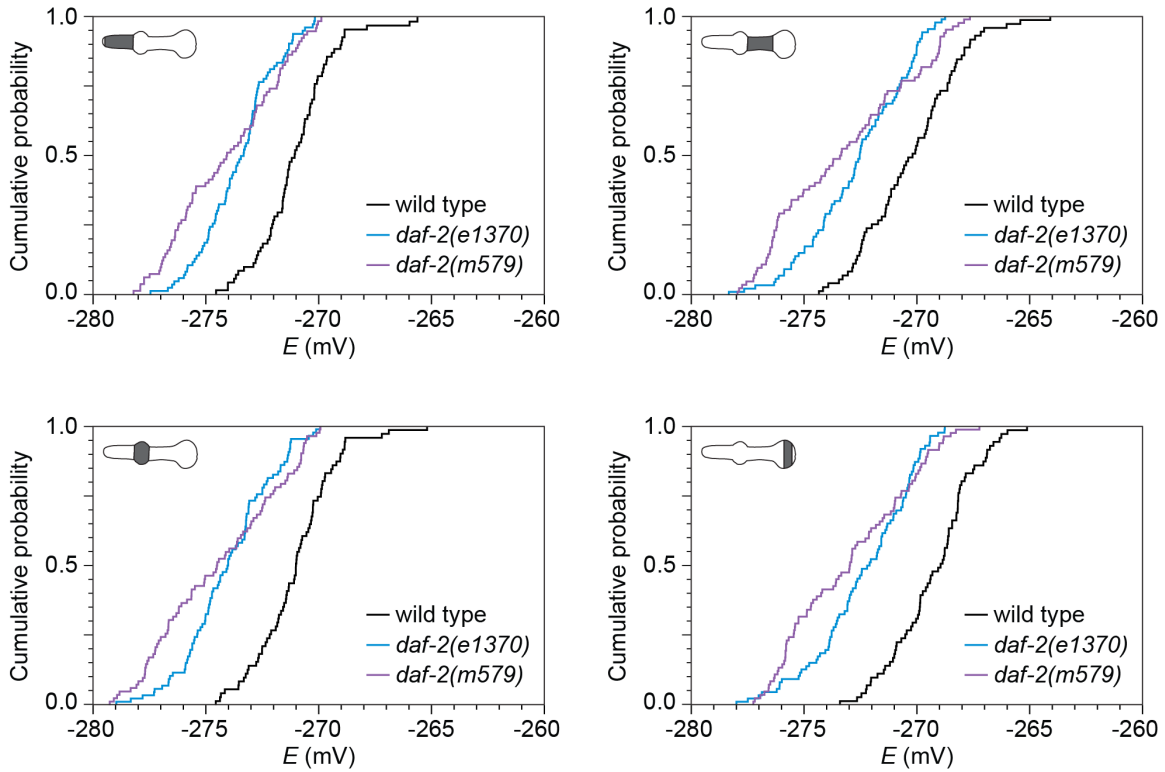
Figure 3.12: Lower cytosolic redox potential in pharyngeal muscles of ligand-binding and kinase-domain *daf-2* mutants.

The *e1370* allele encodes a strong loss-of-function point mutation affecting the *daf-2* protein's kinase domain. The *m579* allele encodes a loss-of-function *daf-2* ligand-binding-domain point mutation that causes type A insulin resistance in humans. Both *daf-2* mutant alleles exhibit lower cytosolic *E* in feeding muscles, compared to wild-type animals. For statistics see Table 3.4
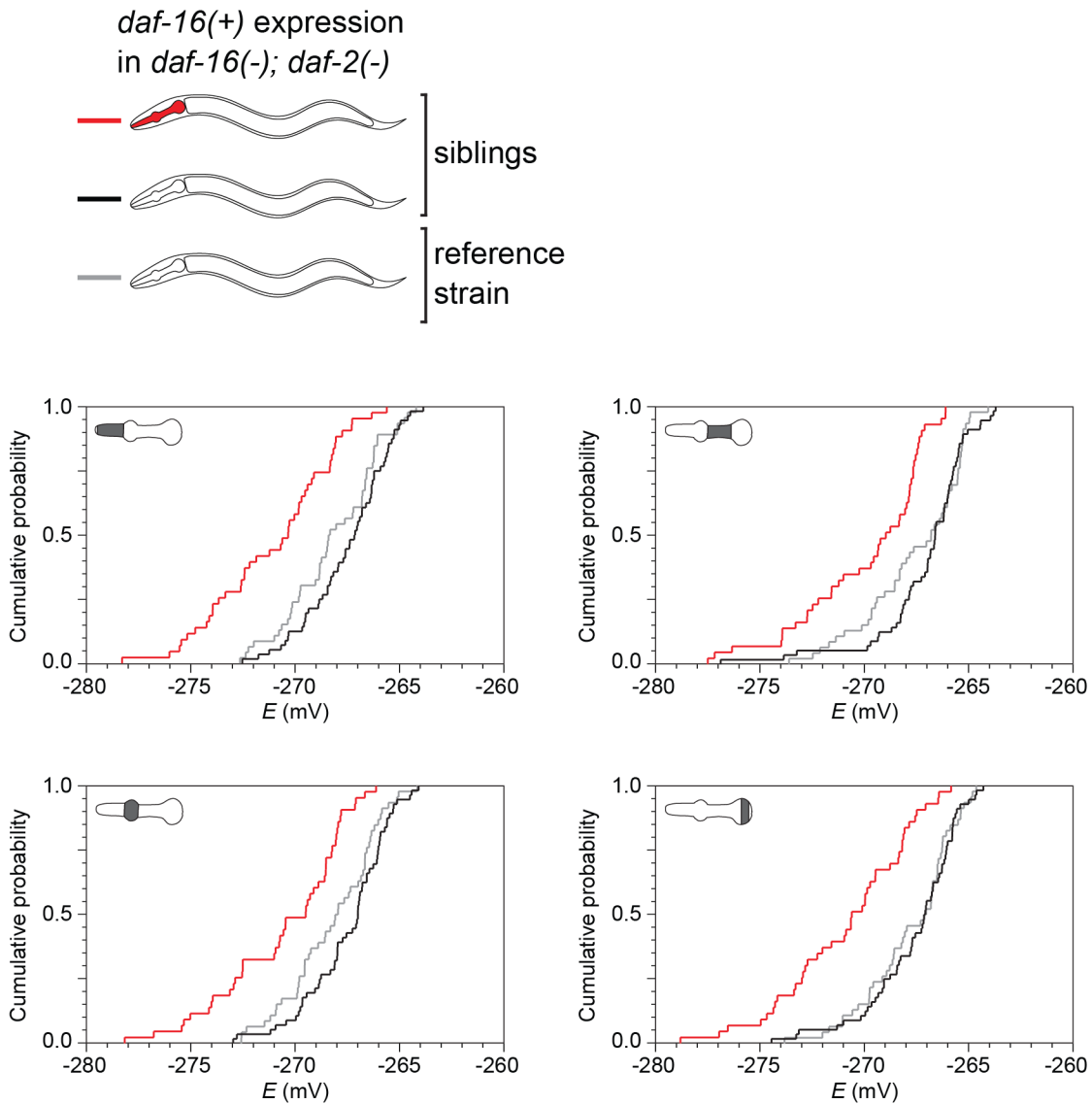
Figure 3.13: *daf-16(+)* **acts locally to lower cytosolic redox potential.**

Restoring *daf-16(+)* expression exclusively in the feeding muscles of *daf-16(mu86); daf-2(e1370)* double mutants is sufficient to lower the cytosolic redox potential in specific pharyngeal muscles, denoted by the diagrams in the top left of each panel. Individuals carrying the *ExYW[Pmyo-2::daf-16d/f::Cherry; rol-6 (su1006)]* extrachromosomal transgene in red; siblings without the transgene in black; and a *daf-16(mu86); daf-2(e1370)* reference strain in grey. For statistics see Table 3.5

Table 3.1 – Measurements of redox potential in feeding muscle

A) Descriptive statistics. Potentials reported as [mean ± s.d. (n), mV]

Genotype	Pharyngeal region	E
wild type	(region 1)	-270.2 ± 2.3 (394)
	(region 2)	-270.0 ± 2.3 (394)
	(region 3)	-268.4 ± 2.6 (394)
	(region 4)	-267.1 ± 2.4 (394)

B) Statistical comparisons between pharyngeal regions. Reported as [mean ± s.e., mV]

Genotype	Pharyngeal regions		Δ(E)	p-value
wild type	(region 1)	(region 2)	-0.2 ± 0.2	0.6409
	(region 1)	(region 3)	-1.8 ± 0.2	< 0.0001
	(region 2)	(region 4)	-3.1 ± 0.2	< 0.0001
	(region 2)	(region 3)	-1.6 ± 0.2	< 0.0001
	(region 2)	(region 4)	-2.9 ± 0.2	< 0.0001
	(region 3)	(region 4)	-1.3 ± 0.2	< 0.0001

Table 3.2 – Measurements of redox potential differences

A) Descriptive statistics. Potentials reports as [mean ± s.d. (n), mV]
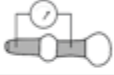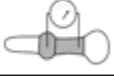
Genotype	Pharyningeal region pair	ΔE
		-0.2 ± 0.5 (394)
		-1.8 ± 1.3 (394)
wild type		-3.1 ± 1.6 (394)
		-1.6 ± 1.1 (394)
		-2.9 ± 1.5 (394)
		-1.3 ± 1.0 (394)

Table 3.2 *(continued)* – Measurements of redox potential differences

B) Statistical comparisons between potential different across all pharyngeal regions. Reported as [mean ± s.e., mV]
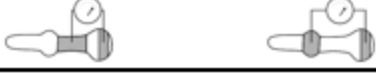
Genotype	Pharyngeal region pairs		$\Delta(\Delta E)$	*p*-value
			-1.6 ± 0.1	<0.0001
			-2.9 ± 0.1	<0.0001
			-1.4 ± 0.1	<0.0001
			-2.7 ± 0.1	<0.0001
			-1.1 ± 0.1	<0.0001
			-1.3 ± 0.1	<0.0001
			-1.1 ± 0.1	<0.0001
wild type			-0.2 ± 0.1	0.1915
			-1.5 ± 0.1	<0.0001
			-1.3 ± 0.1	<0.0001
			-0.2 ± 0.1	0.1915
			-0.5 ± 0.1	<0.0001
			-1.8 ± 0.1	<0.0001
			-0.3 ± 0.1	0.0223
			-1.6 ± 0.1	<0.0001

Table 3.3 – Measurements of redox potential in insulin-pathway mutants

A) Descriptive statistics. Potentials reported as [mean ± s.d. (n), mV]

Genotype	N				
wild type	(273)	-270.8 ± 2.4	-270.2 ± 2.5	-268.9 ± 2.8	-267.9 ± 2.6
daf-2(e1370)	(225)	-273.2 ± 1.7	-273.1 ± 1.8	-271.7 ± 2.2	-271.0 ± 2.2
daf-16(mu86)	(224)	-269.4 ± 2.2	-269.0 ± 2.2	-267.7 ± 2.3	-267.5 ± 2.2
daf-16(mu86); daf-2(e1370)	(209)	-269.5 ± 2.4	-269.2 ± 2.4	-268.1 ± 2.6	-267.8 ± 2.1

B) Parameter estimates for linear models of each pharyngeal region.
Reported as [Est ± s.e. (mV)] and [p-value]

Term				
Intercept	-270.8 ± 0.1	-270.2 ± 0.1	-268.9 ± 0.2	-267.9 ± 0.1
	< 0.0001	< 0.0001	< 0.0001	< 0.0001
daf-2	-2.5 ± 0.2	-2.8 ± 0.2	-2.8 ± 0.2	-3.1 ± 0.2
	< 0.0001	< 0.0001	< 0.0001	< 0.0001
daf-16	1.4 ± 0.2	1.3 ± 0.2	1.2 ± 0.2	0.4 ± 0.2
	< 0.0001	< 0.0001	< 0.0001	0.0555
daf-2 * daf-16	2.4 ± 0.3	2.6 ± 0.3	2.4 ± 0.3	2.7 ± 0.3
	< 0.0001	< 0.0001	< 0.0001	< 0.0001

Model: E = Intercept + daf-2 + daf-16 + daf-2 * daf-16 + ε

Table 3.4 – Pharyngeal redox measurements in *daf-2* alleles

A) Descriptive statistics. Potentials reported as [mean ± s.d. (n), mV]

Genotype	N				
wild type	(71)	-271.0 ± 1.7	-271.0 ± 1.7	-270.2 ± 2.1	-269.3 ± 1.8
daf-2(m579)	(82)	-274.1 ± 2.3	-274.4 ± 2.7	-273.3 ± 3.0	-273.0 ± 2.7
daf-2(e1370)	(86)	-273.5 ± 1.6	-274.0 ± 1.9	-272.6 ± 2.2	-272.4 ± 2.2

B) Statistical comparisons between genotypes, Δ E [mean ± s.e., mV] and p-value

Genotype pair					
wild type	daf-2(m579)	-3.0 ± 0.3 < 0.0001	-3.4 ± 0.4 < 0.0001	-3.0 ± 0.4 < 0.0001	-3.8 ± 0.4 < 0.0001
wild type	daf-2(e1370)	-2.5 ± 0.3 < 0.0001	-3.0 ± 0.3 < 0.0001	-2.4 ± 0.4 < 0.0001	-3.1 ± 0.4 < 0.0001
daf-2(m579)	daf-2(e1370)	-0.5 ± 0.3 0.161	-0.4 ± 0.3 0.395	-0.6 ± 0.4 0.247	-0.6 ± 0.3 0.157

Table 3.4 *(continued)* – Pharyngeal redox measurements in *daf-2* alleles

C) Statistical comparisons between pharyngeal regions, Δ E [mean ± s.e., mV]

and p-*value*

Pharyngeal regions		wild type	daf-2(m579)	daf-2(e1370)
		0.0 ± 0.3	0.4 ± 0.4	0.5 ± 0.3
		1.000	0.834	0.441
		-0.8 ± 0.3	-0.8 ± 0.4	-0.9 ± 0.3
		0.053	0.209	0.018
		-1.8 ± 0.3	-1.1 ± 0.4	-1.2 ± 0.3
		< 0.0001	0.062	0.001
		-0.8 ± 0.3	-1.2 ± 0.4	-1.4 ± 0.3
		0.064	0.028	< 0.0001
		-1.8 ± 0.3	-1.4 ± 0.4	-1.6 ± 0.3
		< 0.0001	0.005	< 0.0001
		-1.0 ± 0.3	-0.2 ± 0.4	-0.3 ± 0.3
		0.009	0.947	0.839

Table 3.5 – Transgenic rescue of pharyngeal *daf-16* expression in feeding muscle

A) Descriptive statistics. Potentials reported as [mean ± s.d. (n), mV], (experiments performed in 2-days-old individuals).

Grp	Parental strain	N	daf-16(+) expression				
A	daf-16(mu86); daf-2(e1370); Ex[Pmyo-2::daf-16(+); Pmyo-2::mCherry]	(43)	pharynx	-271.1 ± 3.0	-270.6 ± 3.0	-269.9 ± 3.0	-270.9 ± 3.1
B		(56)	none	-267.5 ± 2.0	-267.5 ± 2.0	-267.1 ± 2.3	-267.6 ± 2.2
C	daf-16(mu86); daf-2(e1370)	(46)	none	-268.2 ± 2.2	-268.2 ± 2.1	-267.6 ± 2.4	-267.8 ± 2.1

B) Statistical comparisons, p-value

Groups					
A	B	<.0001	< 0.0001	< 0.0001	< 0.0001
C	B	0.31	0.26	0.59	0.93

Methods

C. elegans were cultured under standard conditions at 20 ºC. Wild-type *C. elegans* was Bristol N2. Double and triple mutants were generated by standard genetic methods. The 25°C Daf-c phenotype was used to identify *daf-2* mutants. *daf-16(mu86)* and *daf-16(+)* were distinguished by PCR (*2*). *ydIs1* was identified based on the presence of green fluorescence in the pharynx. *ExYW [Pmyo-2::daf-16d/f::Cherry; rol-6 (su1006)]* was identified based on the presence of red florescence in the pharynx.

Live fluorescence microscopy was performed as described in chapter 2. Animals were staged by transferring late L4 larvae to NGM plates with 4.5 µg/ml FUDR, and imaging was conducted between 44 and 52 hours after transfer (day 2 of adulthood). Before imaging, worms were transferred to NIM plates at room temperature (21-23 °C) for 80 min. We optimized exposure times to use at least two thirds of the dynamic range of the camera. This step ensures that image segmentation is performed consistently across all experimental conditions and for all imaged tissues. The fluorescence images for part 1 were acquired with 2x2 binning using an average exposure time of 165ms. The fluorescence images for part 2 and part 3 of this chapter were acquired with 4x4 binning using an average exposure time of 40 ms. In control experiments we imaged 20 animals sequentially with 2x2 and 4x4 binning and found that the resulting estimates of the ratio of fluorescence ($R_{410/470}$) are highly correlated ($r = 0.961$).

Image processing was conducted in ImageJ (NIH) and Matlab (Mathworks). We performed background subtraction by removing the mode intensity value of the entire image from each pixel (since the fluorescent regions were small relative to the total area imaged, the vast majority of pixels correspond to background). To segment the images, we defined regions of interest (ROI) by applying a threshold in the 410 nm excitation images. We used the same intensity value for the segmentation across all conditions. We use the ROIs to quantify both the 410 nm and 470 nm excitation images (I_{410} and I_{470} images, respectively). We obtained nearly identical estimates of $R_{410/470}$ are by segmenting on either I_{410} or I_{470} image ($r = 0.999$, p < 0001 for the 394 animals in Figure 3.2).

For the ratiometric measurements, we calculated $R_{410/470}$ by computing the ratio of the total fluorescence between the segmented I_{410} and I_{470} regions. To study how $R_{410/470}$, OxD_{roGFP} and E_{roGFP} vary along the anterior-posterior (A-P) axis of the pharynx, we generated $R_{410/470}$ profiles along the midline of this tissue using automated scripts in ImageJ. First, the segmented I_{410} and I_{470} regions were rotated, centered and reflected to orient them along their A-P axis. We then constructed a polyline in the I_{410} image along the midline of the pharynx using features of five morphological pharyngeal landmarks (procorpus, metacorpus, anterior half of isthmus, posterior half of isthmus and posterior bulb). Boxes centered on the average locations for each landmark were drawn automatically and their centroids were connected. The most anterior and most posterior pharyngeal coordinates were identified as those in which the perimeter of the ROI intersects with the extension of the first and last segments of the polyline. The resulting

6-segment polyline was visually inspected and, when necessary, manually adjusted to ensure the quality of the fit to the midline of each pharynx. We refer to this polyline as the medial axis of the pharynx. We measured the intensity along the medial axis in I_{410} and I_{470} images, using a line width of 5.16 μm (2 pixels) for 4x4 binning images and a line width of 7.74 μm (6 pixels) for 2x2 binning images. The resulting intensity vectors were exported to Matlab using the Multi Plot command in ImageJ.

The intensity vectors were length-normalized using bilinear interpolation. We determined the E profile along the A-P axis of the pharynx, from the computed element-wise intensity ratios (I_{410}/I_{470}) between these two vectors using Eq.1 and 2. We note that the average value of E for the medial axis approximates very closely that of the whole pharynx ($r = 0.9988$, $p < 0001$ for the 394 animals in Fig. 2), therefore we use this value as the average value for the tissue. To generate the average subtracted A-P E profiles we subtracted the E medial axis from the element-wise E vector.

To calculate the value of E for individual muscle segments, we identified muscle boundaries based on the position of the morphological landmarks of the pharynx in the length-normalized intensity vectors. The selected boundaries are shown in brackets in Figure 3.2 and onwards. We computed E from the ratio of the 410 and 470 nm total intensities within each region.

Pixel-by-pixel E images, computed from the raw unsegmented I_{410} and I_{470} images, provide a valuable visualization tool that complements the formal image analysis and

quantification described above. We computed E from pixel-by-pixel $R_{410/470}$ values, and generated RGB images by mapping E values to a colormap. We wanted these images to provide information about the magnitude of the intensity signals utilized; de-emphasizing pixels were the signal was below specific cutoffs. To this end, we adjusted the brightness of pixels whose intensity values in the I_{410} or I_{470} images were below the value of the intensity cutoff used for segmentation (equal to 2000 in all images shown). Images were transformed to the hue-saturation-brightness (HSB) color space, and pixels with intensity values above the cutoff were assigned a brightness value of 1, while those with intensities below the cutoff were assigned a brightness value equal to their intensity divided by the cutoff value. The resulting HSB image was transformed to RGB for visualization. We used the cool-warm and similar diverging colormaps to color-code images and pharyngeal E profiles, as these colormaps are perceptually linear and behave well for observers with color-deficient vision.

For the oxidative stress assays, we treated animals with 5 mM *tert*-butyl hydroperoxide (*t*-BuOOH), in freshly made NIM plates (used within 4 hours of preparation). The *tert*-butyl group increases the stability and fat-solubility of this oxidant compared with hydrogen peroxide. In contrast to diamide, *t*-BuOOH does not oxidize protein thiol groups directly (Winterbourn and Metodiewa, 1999); rather, it is thought to act by oxidizing glutathione thiol (GSH) into glutathione disulfide (GSSG), which, in turn, leads to the formation of an intramolecular disulfide bond within roGFP1_R12. $R_{410/470}$ time series in untreated individual worms were acquired for 10 min prior to *t*-BuOOH treatment. Individual worms were then transferred to plates with 5 mM *t*-BuOOH and

imaged for additional 60 min, with a gap of 3 to 6 minutes between treatments. Images were acquired every 30 seconds.

All statistical analyses were performed in JMP (SAS) and Matlab (Mathworks). We tested for differences in the average E among groups using ANOVA. We used the Tukey HSD post-hoc test to determine which pairs of groups in the sample differ, in cases where more than two groups were compared. We used least-squares regression to quantify genetic interactions between wild-type and mutant alleles of *daf-2* and *daf-16* using the following linear model: E = Intercept + *daf-2* + *daf-16* + *daf-2* * *daf-16* + ε, and to quantify genetic interactions between presence and absence of *daf-16(+)*-expressing transgenes in the pharynx and intestine using the linear model: E = Intercept + pharynx + intestine + pharynx * intestine + ε. The second to last term in each of these models quantifies the existence, magnitude and type (synergistic or antagonistic) of genetic interaction between, respectively, *daf-2* and *daf-16* mutant alleles, and pharyngeal and intestinal *daf-16(+)* expression.

For the functional data analysis (FDA) perform in the oxidative stress assay, we used the FDA statistical package in Matlab to model and analyze positional-series of E values in pharyngeal A-P profiles and time-series of E values in the response to *t*-BuOOH. The basic idea of this approach is to express discrete spatial or temporal series of observations in the form of a function. These functions are then treated as single observations, which are analyzed statistically applying concepts of multivariate analysis (Ramsay et al., 2009). Time series of E values consisted of 21 observations under baseline conditions and

113 observations in the presence of 5 mM t-BuOOH for each of three pharyngeal muscle segments (procorpus, isthmus and posterior bulb) in 64 animals. For the functional regression, we first subtracted the average value of E under baseline conditions for each muscle segment. The data were represented using a B-spline basis consisting of 82 order 6 polynomials. Smoothing was achieved by penalizing curve curvature using GCV minimization to identify the optimal level of smoothing. We then performed functional regression, a technique that is the functional equivalent of ANOVA where functional responses are decomposed into functional effects, using the functional linear model:

$E_{mw}(t) = \mu(t) + \alpha_m(t) + \varepsilon_{mw}(t)$, satisfying the constrain $\Sigma_m \alpha_m(t) = 0$ for all t (Ramsay et al., 2009) In this model, the function μ represents the grand mean across all 64 worms (w) and three muscle segments (m), and the effect functions α_m represent departures from the grand mean specific to each of the three muscle segments. The residual functions ε_{mw} capture unaccounted variation. The regression functions were represented using a B-spline basis consisting of 82 order 6 polynomials. Smoothing of the regression functions was achieved by penalizing curve curvature and optimized by the cross-validation method. Point-wise 68.3% confidence intervals were calculated for each regression function by adding and subtracting 1 standard error of the regression function parameter-vector estimates, calculated from the covariance of the residual functions.

For the functional principal components analysis (PCA), we first subtracted the average value of E under baseline conditions from the posterior-bulb E traces. The data were represented using a B-spline basis consisting of 70 order 6 polynomials. Smoothing of the functional representation of the data and of the PCA functions was achieved by

93

penalizing curve curvature. At the interval boundaries spline function values are entirely determined by a single B-spline coefficient, resulting in instability of the PCA functions at the interval boundaries. Therefore, to optimize the PCA fits, we maximized the coefficient of determination between the data and the prediction from the PCA, over the interval ending at 58 minutes in t-BuOOH. This required a three-way optimization among the number of B-splines used to represent the data and the smoothing penalties for the functional representation of the data and for the PCA functions.

References

1. Albertson DG, Thomson JN (1976) The pharynx of Caenorhabditis elegans. Philos Trans R Soc Lond B Biol Sci 275: 299-325.

2. Altun ZF, Chen B, Wang ZW, Hall DH (2009) High resolution map of Caenorhabditis elegans gap junction proteins. Dev Dyn 238: 1936-1950.

3. Altun ZF, Hall DH (2009) Alimentary System, Pharynx. In: Herndon LA, editor. WormAtlas. July 21, 2012. ed.

4. Avery L (1993) The genetics of feeding in Caenorhabditis elegans. Genetics 133: 897-917.

5. Avery L, Horvitz HR (1989) Pharyngeal pumping continues after laser killing of the pharyngeal nervous system of C. elegans. Neuron 3: 473-485.

6. Avery L, You YJ (2012) C. elegans feeding. WormBook: 1-23.

7. Camazine S, Deneubourg JL, Franks NR, Sneyd J, Theraulaz G, et al. (2002) Self-Organization in Biological Systems.

8. Franks CJ, Holden-Dye L, Bull K, Luedtke S, Walker RJ (2006) Anatomy, physiology and pharmacology of Caenorhabditis elegans pharynx: a model to define gene function in a simple neural system. Invert Neurosci 6: 105-122.

9. Hamer I, Foti M, Emkey R, Cordier-Bussat M, Philippe J, et al. (2002) An arginine to cysteine(252) mutation in insulin receptors from a patient with severe insulin resistance inhibits receptor internalisation but preserves signalling events. Diabetologia 45: 657-667.

10. Honda Y, Honda S (1999) The daf-2 gene network for longevity regulates oxidative stress resistance and Mn-superoxide dismutase gene expression in Caenorhabditis elegans. FASEB J 13: 1385-1393.

11. Hu X, Dahl G (1999) Exchange of conductance and gating properties between gap junction hemichannels. FEBS Lett 451: 113-117.

12. Kenyon C, Chang J, Gensch E, Rudner A, Tabtiang R (1993) A C. elegans mutant that lives twice as long as wild type. Nature 366: 461-464.

13. Li R, Bowerman B (2010) Symmetry breaking in biology. Cold Spring Harb Perspect Biol 2: a003475.

14. Li S, Dent JA, Roy R (2003) Regulation of intermuscular electrical coupling by the Caenorhabditis elegans innexin inx-6. Mol Biol Cell 14: 2630-2644.

15. Panchin Y, Kelmanson I, Matz M, Lukyanov K, Usman N, et al. (2000) A ubiquitous family of putative gap junction molecules. Curr Biol 10: R473-474.

16. Patel DS, Garza-Garcia A, Nanji M, McElwee JJ, Ackerman D, et al. (2008) Clustering of genetically defined allele classes in the Caenorhabditis elegans DAF-2 insulin/IGF-1 receptor. Genetics 178: 931-946.

17. Ramsay OJ, Hooker G, Graves S (2009) Functional data analysis with R and MATLAB Dordrecht; New York: Springer.

18. Starich TA, Miller A, Nguyen RL, Hall DH, Shaw JE (2003) The Caenorhabditis elegans innexin INX-3 is localized to gap junctions and is essential for embryonic development. Dev Biol 256: 403-417.

19. Stroustrup N, Ulmschneider BE, Nash ZM, Lopez-Moyado IF, Apfeld J, et al. (2013) The Caenorhabditis elegans Lifespan Machine. Nat Methods 10: 665-670.

20. Tullet JM, Hertweck M, An JH, Baker J, Hwang JY, et al. (2008) Direct inhibition of the longevity-promoting factor SKN-1 by insulin-like signaling in C. elegans. Cell 132: 1025-1038.

Chapter 4

Changes in the spatial pattern of cytosolic redox potential

during development and aging

Abstract

The spatial and temporal control of E_{GSH} *in vivo* is not well understood. Our previous work on young individuals shows spatial differences across the anterior-posterior axis of the pharynx. To learn when this spatial pattern arises, and whether it changes over time, we measured cytosolic E_{GSH} in feeding muscle during development and aging. We found that the spatial pattern observed in 2-day-old individuals arises in early adulthood. However, in a few cases, spatial differences could be observed during postembryonic development: this group of individuals has unusually high levels of oxidation, and exhibit steep differences between muscle segments, with an anterior-posterior delta of up to 15mV. We hypothesize that this phenotype is related to the action of NADPH oxidases during molting.

In aging, we observe a complex time-dependent dynamic for wild type animals. We see no net increase in the level of oxidation during the first 10 days of adulthood; instead, we observe an increase in the variance in old populations. A mutation decreasing the activity of the insulin receptor dramatically changes this age-dependent phenotype. *daf-2(e1370)* mutants show a monotonic decrease in E_{GSH} during the first 10 days of adulthood. We also observe a time-dependent change in the anterior-posterior differences of E_{GSH} potential during aging, where both genotypes present a similar dynamic. Lastly, we show that the spatial differences in potential are correlated with remaining lifespan, while the absolute level of E_{GSH} in different muscles remains uncorrelated. This suggests a mechanistic link between the process that determines spatial anterior-posterior differences in potential and the process that determines probability of survival.

Chapter 4 – Introduction

In chapter 3, we show the existence of a tissue-scale pattern of cytosolic redox potential in the feeding muscle of 2-day-old adults. This pattern could be an intrinsic characteristic of the mechanical or structural properties of the tissue, invariant over time (e.g. shape, fibers alignment or differences in the contractile properties of procorpus and terminal bulb). Alternatively, the pattern might reflect a functional role in the biology of the tissue and the organism that is not merely structural and that changes over time. We reasoned that examination of redox spatial differences over time could help us discern between these two hypotheses. In this chapter, we will investigate the anterior-posterior cytosolic redox pattern in the pharynx during development and aging, and discuss how changes in the pattern inform us about its function.

We begin by asking when the tissue-scale pattern of cytosolic redox potential is formed. If the spatial pattern has been there since the organogenesis of the pharynx, it would suggest that the redox difference is 'intrinsic' to the existence of this organ. If the spatial pattern appears in postembryonic development – where the pharynx is already formed and functioning in larval stages – it would suggest the pattern arises as a specialization or further specification of feeding muscles cells, but still as part of their developmental program. Lastly, if the tissue-scale pattern of the cytosolic redox potential is established during adulthood, it could reflect functional changes occurring to the tissue throughout its life that are not part of its developmental program *per se*.

Next we ask whether the absolute level of oxidation of the pharynx or the spatial differences in the cytosolic redox potential of wild type are constant throughout adulthood, or whether these two variables change with age. In chapter 3, we established that insulin signaling modulates the cytosolic redox potential of the pharynx, through the downstream transcription factor FOXO/DAF-16. We also showed how this transcription factor has a muscle-type specific effect, and contributes to the spatial differences of the cytosolic redox potential. Because insulin signaling has evolutionarily-conserved effects in the regulation of longevity and survival under oxidative stress, we decided to measure the cytosolic redox potential in feeding muscle throughout adulthood, both in wild type and in the insulin receptor mutant *daf-2(e1370),* the most comprehensive model for the study of longevity in the worm. We wanted to test whether the absolute level of oxidation in the pharynx, or the spatial differences of the cytosolic redox potential, were age-dependent phenotypes. If we found this to be so, we would investigate how decreased insulin signaling affected those changes.

In the field of aging biology, researches are actively looking for biomarkers– that is, physiological variables that could reduce uncertainty about the time of death. To test whether there is a link between the redox state of the pharynx and the probability of survival of the whole organism, we asked whether the absolute level of oxidation of the pharynx or the spatial differences of the cytosolic redox potential were correlated with the remaining lifespan in wild type.

Chapter 4

Part 1 – Cytosolic redox potential and anterior-posterior redox pattern in the pharyngeal muscle during development

The embryonic development of *C.elegans*

Many factors make *C.elegans* a great choice as a model organism, including a short life cycle (~3 days) and a completely stereotyped development. The cell lineages relating the first zygotic cell to the nearly 1000 somatic cells in the adult animal have been mapped out exactly (Sulston 1988). The development of the nematode is composed of two phases: an embryonic phase, where the basic body plan of the adult animal is established; and a postembryonic stage where the worm grows and develops sexually, passing through four larval stages delimited by molting (Figure 4.1).

In the embryonic phase of development cell proliferation and organogenesis take place. At 20°C the first cleavage happens 40 min after fertilization. Cell proliferation from the 2-cell to the 30-cell stage takes place within the mother's uterus. 150 min post fertilization, the eggs are laid at the gastrulation stage. At this point the embryo is structured in three developmental layers: ectoderm, which generates hypodermis and neurons; mesoderm, which gives rise to pharynx and muscle; and endoderm, which gives rise to germline and intestine (Altun and Hall, 2009).

During organogenesis, taking place between 6 h to 12 h after fertilization, terminal differentiation of cells occurs, forming tissues and organs without many additional cell divisions. The first pharyngeal pumps are observed after 800 min from the first cleavage at 20°C, and the worm hatches from the egg at 840 min (Sulston et al, 1983; Bird and Bird, 1991). The result of the embryonic development is a small worm of 558 cells inside an eggshell, with basically the same somatic architecture of the adult animal. This general body plan does not change during postembryonic development.

A

Fertilization — 0
2-cell — 50
4-cell
8-cell — 100
26-cell, beginning of gastrulation — 150
Eggs laid outside
44-cell
87-cell — 200
99-cell
174-cell
190-cell — 250
Excretory cell born — 300
Ventral cleft closed, end of gastrulation — 310 330 360
Bean stage — 350
Comma stage — 400
1.5 fold (Tadpole) stage — 430 450
Twitching starts — 460 470
2-fold (Plum) stage — 490 510
Visible sexual dimorphism
3-fold (Pretzel) stage — 550 690
Synthesis of larval cuticle starts — 700
Pharyngeal pumping starts — 750
Hatching (558 cells) — 800 840

Cell migrations: Ea, Ep — 150; P4, MS; D; C; AB
Elongation
Gastrulation

©WormAtlas

B

Z4 Z3 Z2 Z1 — C
D
E
F
u, v — G
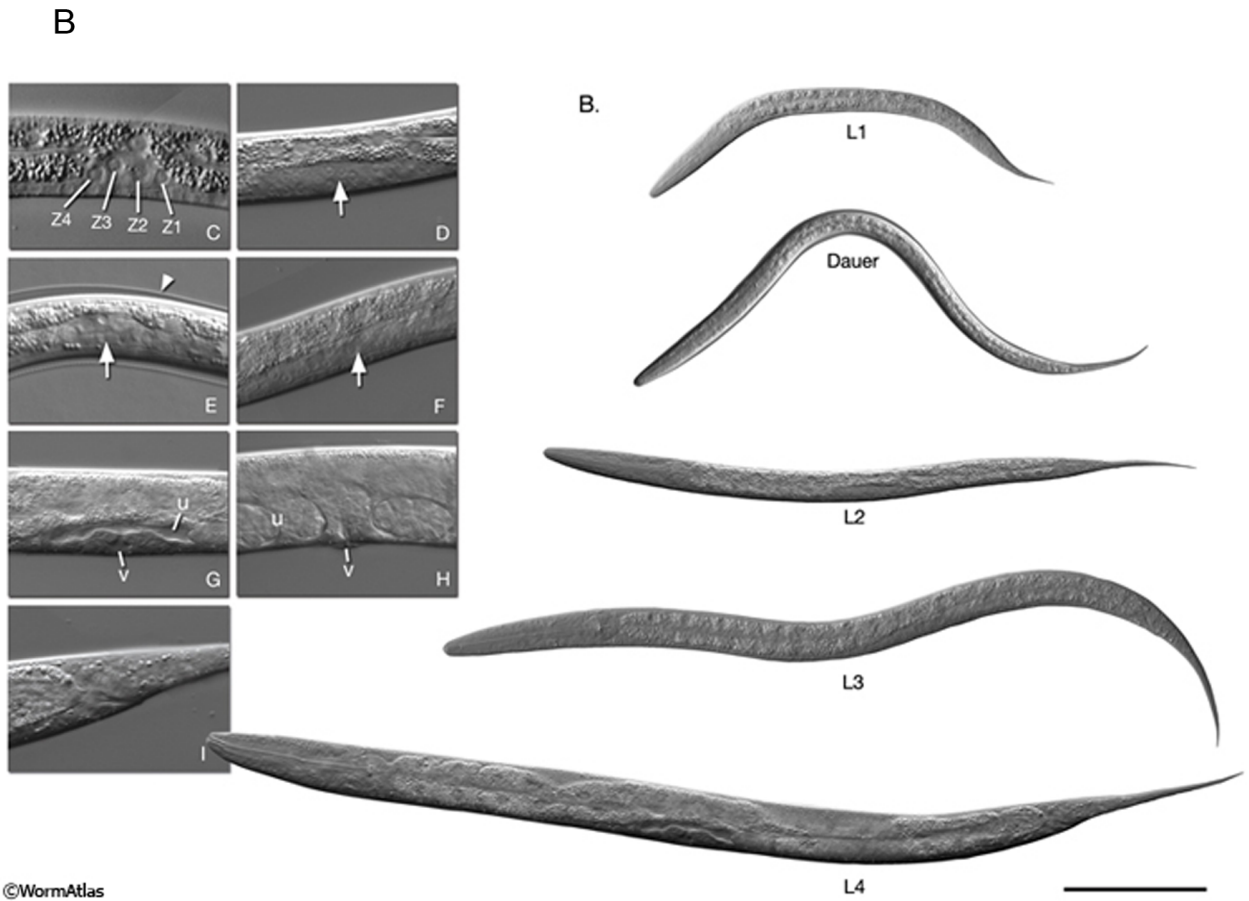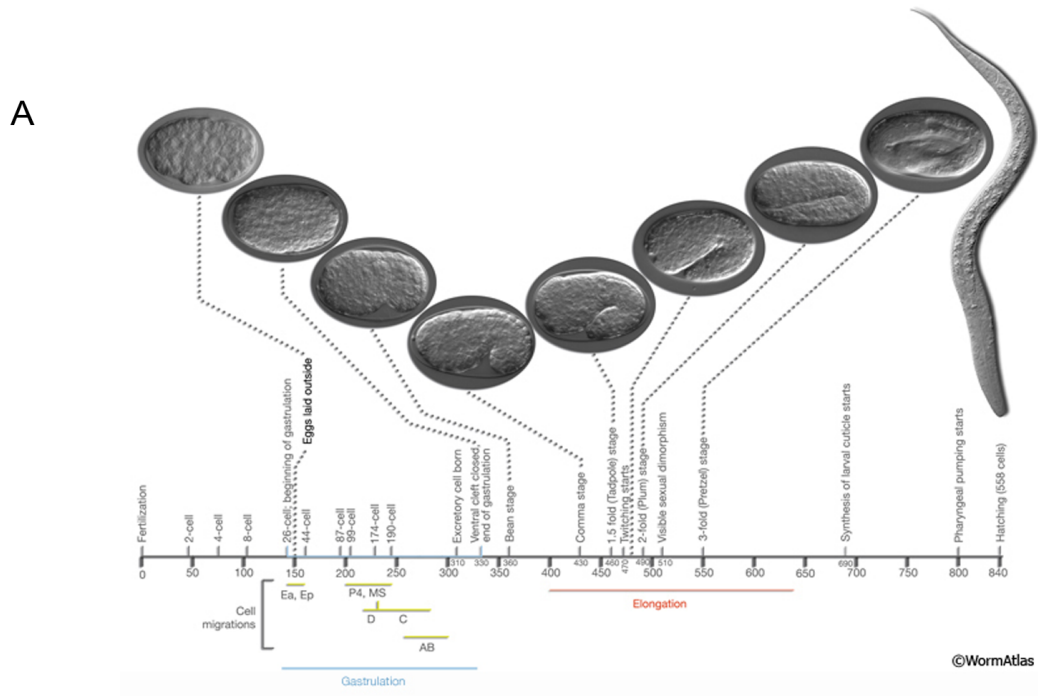u, v — H
I

©WormAtlas

B.
L1
Dauer
L2
L3
L4

Figure 4.1: *C. elegans* **development.** (A) Embryonic development. Numbers below the

103

(**Figure 4.1** *continued*) horizontal axis show approximate times in minutes after fertilization at 20-22˚C. Yellow bars indicate the period of time where cells from a certain lineage migrate towards inside of the embryo. The first cells that move inwards from the ventral surface are gut precursors (E), followed by germline (P4) and mesoderm (MS) precursors. Blue bar indicates gastrulation.

(B) Post-embryonic development. DIC images of each stage larva. Bar 0.1 mm. (C- H) Enlarged DIC images of gonad development for each stage, respectively. Sizes are not to scale. Arrows point to gonads in D-F, v: vulva, u: uterus. (C) Four primordial gonad cells are labeled in L1. (D) Germ cells increase in number in L2. (E) The gonad is similar to an early L2 stage gonad in dauer. Arrowhead points to dauer specific cuticle. (F) Gonad has extended along the ventral body in L3. (G) hermaphrodite somatic structures have formed by mid-L4 stage. (H) Vulva is open to outside and uterus is full of fertilized eggs in adult. (I) The thin, tapered tail of an L4 hermaphrodite. (Adapted from Altun & Hall, 2009)
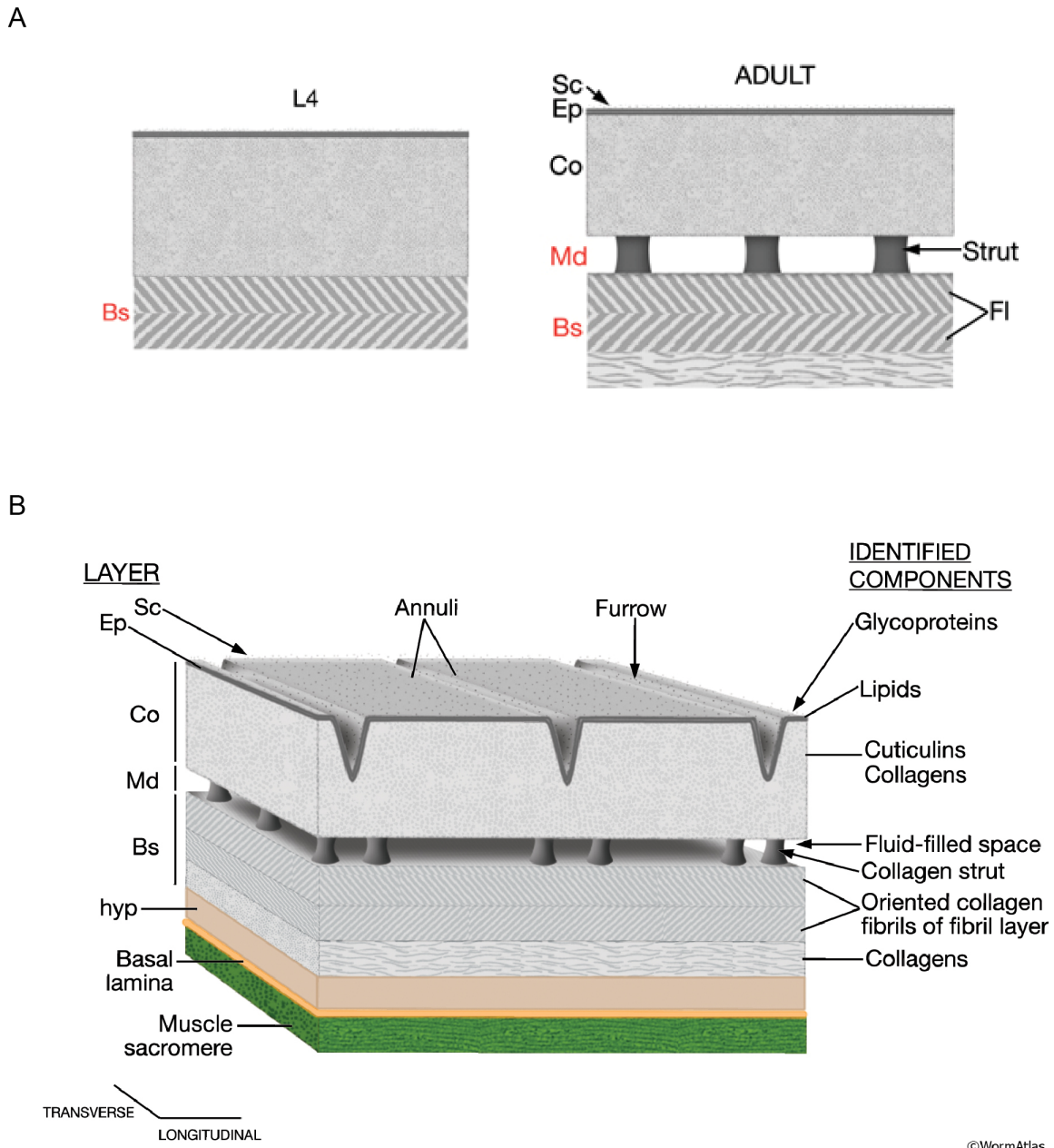
Figure 4.2: The cuticle of the worm. (A) Schematic view of the layer organization in L4 larvae and adults. (B). Detailed view of the adult cuticle layers (right column) and molecular components in each layer (left column): (Sc) Surface coat; (Ep) epicuticle; (Co) cortical zone; (Md) medial zone; (Bs) basal zone. (from Altun & Hall, 2009)
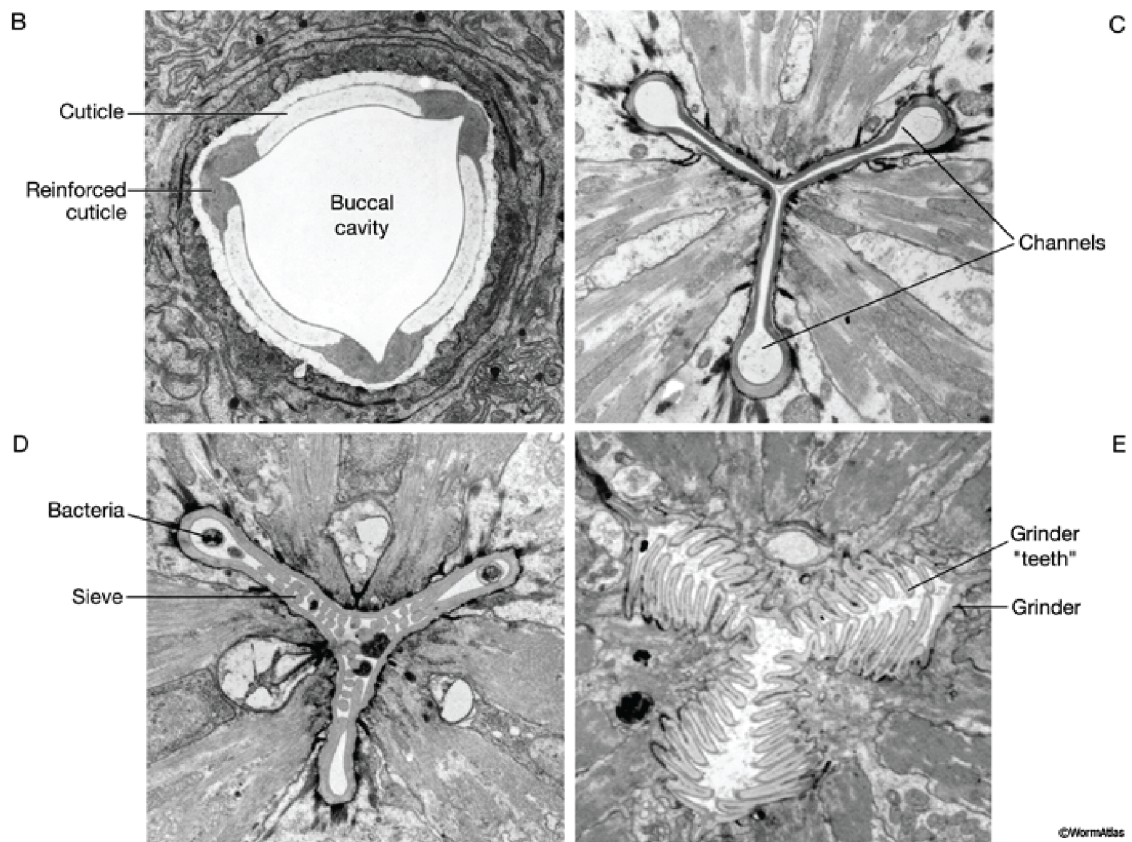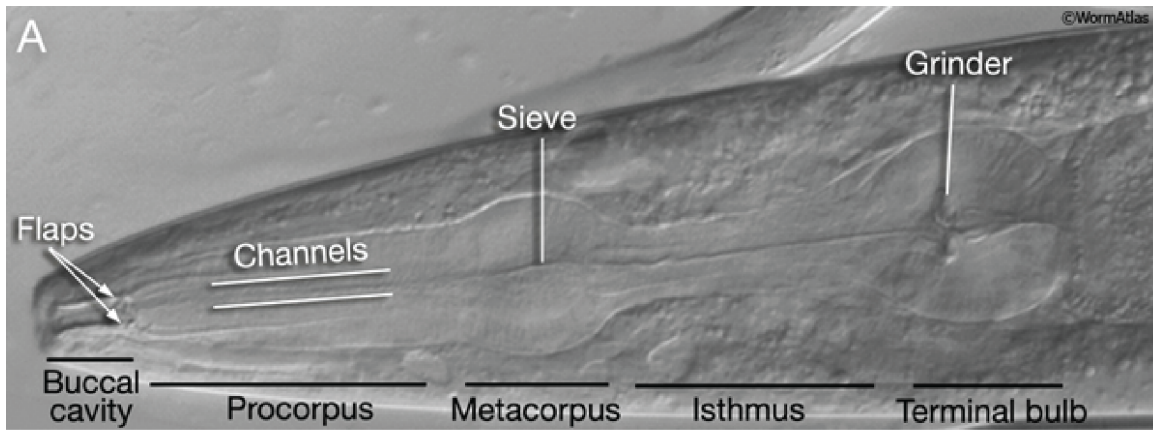
Figure 4.3: Cuticular structures of the pharynx. (A). DIC image of an adult animal head, showing the main morphological compartments of the pharynx (black labels) and the various structures found in lumen cuticle lining (white labels). (B-E) ultrastructure of cuticle specializations in the pharynx (B) Buccal cavity, (C) Procorpus, (D) Metacorpus. (E) Posterior bulb (Adapted from Altun & Hall, 2009)

106

The postembryonic development of *C.elegans*

In the postembryonic phase a sexually mature hermaphrodite, with 959 somatic nuclei, develops. This phase, which takes place in 46 h after hatching, is triggered by feeding. If food is absent upon hatching, the L1 larvae enter in arrest, which can last up to 6 to 10 days. If food becomes available development is resumed (Johnson et al., 1984). In postembryonic development the worm elongates and increases sizes passing through four larval stages (L1 to L4), demarcated by a molting process. During each molt, the worm experiences a period of physical inactivity called lethargus, when it stops moving and feeding. Lethargus precedes the separation of the old cuticle, called apolysis. Then the worm rotates rapidly around its longitudinal axis, loosening the old cuticle, and emerges. This last step is called ecdysis (Singh and Sulston, 1978). The cuticle of the worm (Figure 4.2) *i)* functions as a highly impermeable barrier between the animal and its environment, *ii)* is essential in maintaining the body morphology and its integrity, and *iii)* plays a critical role in motility, through the attachments of body wall muscle (Johnstone, 2000). In each larval stage, the new external cuticle is being secreted by the underlying epithelium in anticipation of and concurrently to the molting process. In the case of the pharynx, an organ that contains its own cuticular system, the pharyngeal muscle cells secrete the new cuticle. The details about the specialized structures of the pharyngeal cuticle will be covered later on in this chapter (Figure 4.3).

The *C.elegans* cuticle (Figure 4.2) is made of cross-linked collagens, insoluble proteins called cuticlins, and associated glycoproteins and lipids (Page and Johnstone 2007). These molecules are highly crossed-linked, assembling into higher order complexes,

107

which determine the structural properties and impermeability of the cuticle. The connectivity of these components is determined in part through intramolecular disulfide bridges, and in part through nonreversible di- and tri-tyrosine cross-links (Stenvall et al., 2011). The collagens, which make up 80% of the soluble proteins of the cuticle, are part of a gene family with more than 170 members. The temporal expression pattern of these genes is tightly controlled in multiphasic waves, with an early peak (4 h prior molting), a middle peak (2 h prior molting) and a late peak (concurrent with molting) (Frand et al., 2005). Some of these proteins are expressed only in certain developmental stages; other proteins make up part of every molting cycle.

Besides the cyclical renewal of the *C. elegans* exoskeleton, the main process taking place in the larval stages is the development of the reproductive system:

- In L1 larval stage (12 h), the somatic gonad precursors (Z1 and Z4) and the germ cells precursors (Z2 and Z3) start to divide. In L1 larvae there is further differentiation of the nervous system and coelomocyte system.
- In L2 larval stage (8 h), the division of germ cells continues. The somatic and germ cells of the gonad are still intermingled spatially.
- In L3 larval stage (8 h), the general organization of the gonad is established (Kimble and Hirsh, 1979). The gonad arms start to elongate, the uterus and the spermatheca start to form, and the sex muscle cells and vulval fate precursors are specified.
- In L4 larval stage (10 h), the gonadogenesis is completed. Meiosis starts at the L3/L4 molt, and the germ cells start to differentiate into sperm. In the late L4 stage, sperm production stops and the remaining germ line cells differentiate into oocytes. The

hallmark of this larval stage is the morphogenesis of the vulva. During late L4, upon

attachment of vulval muscles, the vulva extrudes, generating the adult vulva (Sulston

and Horvitz, 1977). This feature serves as a morphological marker of the transition

to adulthood and is routinely used to synchronize population of worms.

- At 20°C 50 h after hatching, the sexually mature hermaphrodite starts laying eggs.

  The adult hermaphrodite reproductive lifespan is about 4 days, producing

  approximately 300 progeny, and then lives post-reproductively for 10 to 15 days

  (Huang et al., 2004).

Changes in redox biology during development

Metabolic gradients and oxidative gradients, through the endogenous generation of ROS,

are hypothesized to be major factors governing developmental changes (Allen and Balin,

1989). In 1908, marine biologist Otto Warburg observed that fertilization of sea urchin

eggs resulted in a sudden, nearly six-fold increase, in oxygen consumption. He

hypothesized that this increase in oxygen consumption was caused by respiratory activity

during cell proliferation; in fact, later on he won the noble prize for understanding the

"nature and mode of action of the respiratory enzyme". A century later, we have come to

realize that this increase in oxygen consumption is not related to cell proliferation, but

instead is due to the specific use of oxygen by a NADPH oxidase on the egg's surface,

producing nanomolar concentrations of hydrogen peroxide (Wong et al., 2004).

Changes in the redox state associated with metabolic cell activity have also been shown

during development, in other organisms. E_{GSH} changes markedly in different stages of the

life cycle: under proliferative conditions cytosolic values of E_{GSH} are near -260mV; it increases to -220mV under differentiated conditions and to -170mV during apoptosis (Cai and Jones 1998; Kirlin et al.,1999). Similarly, in the zebrafish development, E_{GSH} increases exponentially from -230mV to -190mV in the first 12h after fertilization, oscillates around -190mV during organogenesis and then decreases to -220 mV after hatching, where it remains stable thereafter (Timme-Laragy et al., 2013).

Chapter 4 – Results

Part 1 – Cytosolic redox potential and anterior-posterior redox pattern in the pharyngeal muscle during development

We decided to investigate when formation of the spatial pattern in the cytosolic redox environment occurs. To test whether the spatial pattern exists from organogenesis of the pharynx, or appears later on during postembryonic development or early adulthood, we measure the level of oxidation of the sensor in populations at different developmental stages. Before hatching, the observed levels of expression of *Pmyo2::roGFP1_R12* were too low, so we could not measure this phenotype directly during embryogenesis. We measured the cytosolic E_{GSH} in feeding muscle in the four larval stages of postembryonic development, and in 1- and 2-day-old adults.

During postembryonic development we observe complex changes in the spatial pattern of cytosolic redox potential in feeding muscle. In larval stages, with exception of L1, we observe a small subpopulation of individuals that behave very differently from the rest. These unusual cases affect the interpretability of the average result. Therefore we will discuss our results in three steps: first we address whether E_{GSH} changes during development, comparing the average E_{GSH} for the 6 developmental stages. Next we look at the anterior-posterior difference for the median case within each developmental group, establishing the phenomenon in the majority of the population. So finally, we inspect the

anterior-posterior profiles for all individuals in each developmental stage, to put the observed phenotypes of the deviant individuals in context.

We began by measuring whether the cytosolic E_{GSH} of each muscle segment changes during development (Table 4.1). At the level of the whole tissue we observe that L4 is significantly more oxidized than L3 larvae (p<0.001); all the other comparisons between groups are not statistically significant (Table 4.1). That is also the case in the comparison for the values in the procorpus. For isthmus and posterior bulb we see that not only L4, but also 2-day-olds are significantly more oxidized than L3; while all the other comparisons between groups were not statistically significant. These results suggest that there is an increase of E_{GSH} associated with the L4 stage for all the regions of the tissue; and that there is a second increase in E_{GSH} in early adulthood (2-days-old) that is region specific.

We asked whether the cytosolic redox potential of the pharyngeal regions were statistically different from each other, within each developmental group (Table 4.2). For larval stages, the distributions of potential are indistinguishable between regions. The distributions of redox potential for the pharyngeal regions begin to differentiate from one another by day 1. By day 2, the differences between the anterior and posterior regions are greater (Table 4.2). We conclude that at the population level, pharyngeal muscle segments begin to differentiate their redox potential by the first day of adulthood.

Next, we considered the differences in potential between pairs of muscles within each individual (Table 4.3), and arrived at a similar conclusion. In 1-day-old adults, the difference between procorpus and posterior bulb becomes apparent (Figure 4.4C). In 2-day-old adults we observe a marked difference between procorpus and isthmus, and procorpus and posterior bulb (Figure 4.4B to C). In contrast, the majority of the individuals in each larval stage have a near-zero difference between muscle pairs, suggesting that cytosolic E_{GSH} in their feeding muscle is spatially more homogeneous across the anterior posterior axis. However, for larval stages L2, L3 and L4, we notice that a fraction of the individuals have extreme anterior-posterior differences, as indicated by the heavy long tails to the left in the cumulative probabilities curves (Figure 4.4). We will discuss this phenomenon in the next section, when we inspect the anterior-posterior profiles for all the individuals.

There are two additional points to be made regarding Figure 4.4. Similar to our findings for 2-day-olds in Chapter 3 (Figure 3.2), we observe no difference in potential here between procorpus and anterior bulb. The cumulative probabilities of $\Delta E_{PC\text{-}MC}$ for the six groups are close to zero (Figure 4.4A and Table 4.2), which sets an expectation of how these curves would look if no spatial differences existed. Note, however, that the difference between procorpus and isthmus (Figure 4.4B), and procorpus and posterior bulb (Figure 4.4C) in larval stages is close to zero, but not centered around zero: in fact, the differences between regions have slightly positive values, ranging from 0.5 to 0.9 mV. This shift shows that there is a more nuanced spatial difference in larval stages,
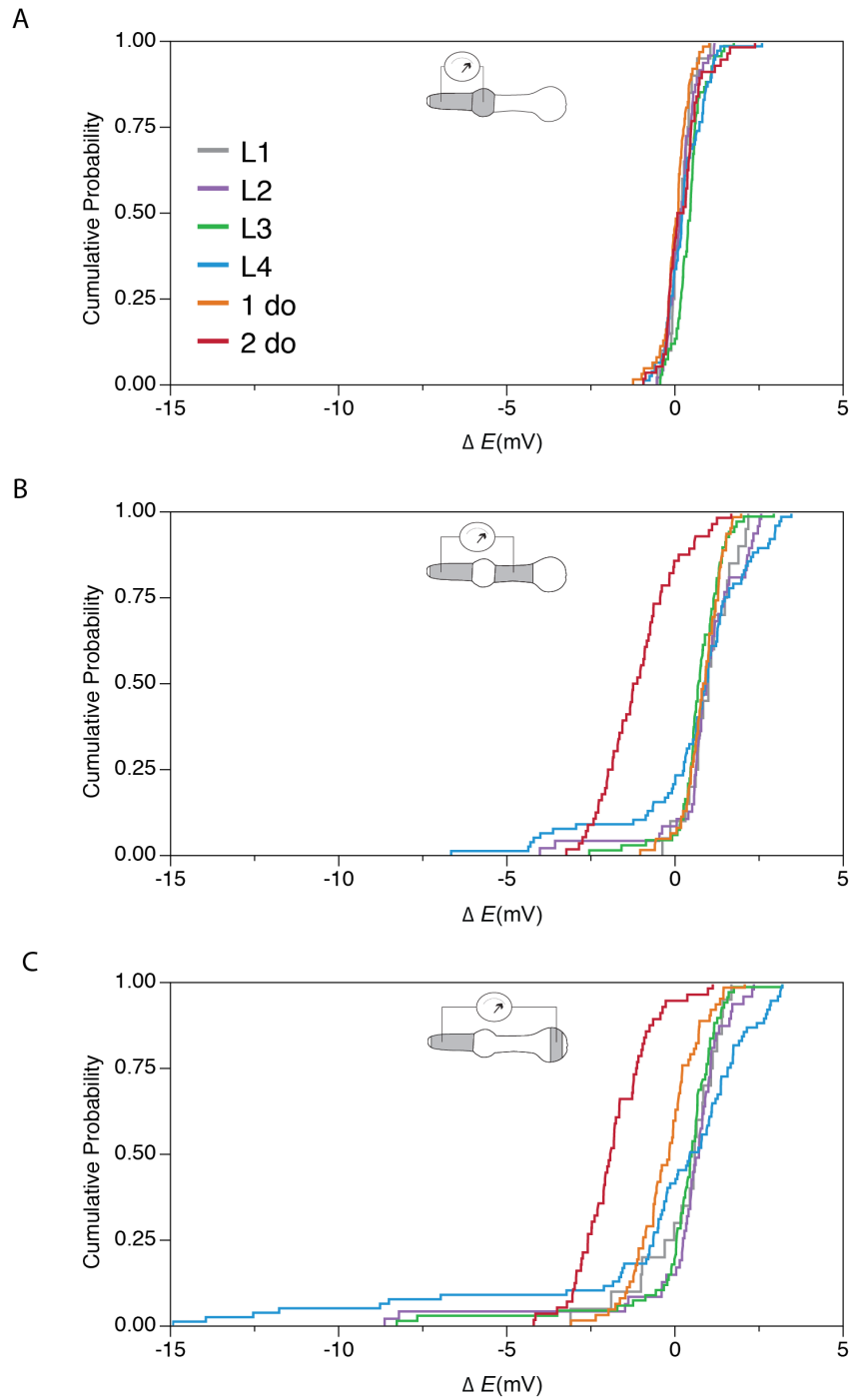
113

Figure 4.4: Differences in potential between pharyngeal regions during post-embryonic development. Cumulative distributions ΔE for the region pair depicted in each panel. Larval stages (L1 to L4); adult stages (1 day old and 2 days old). For statistics see Tables 4.1 to 4.2.
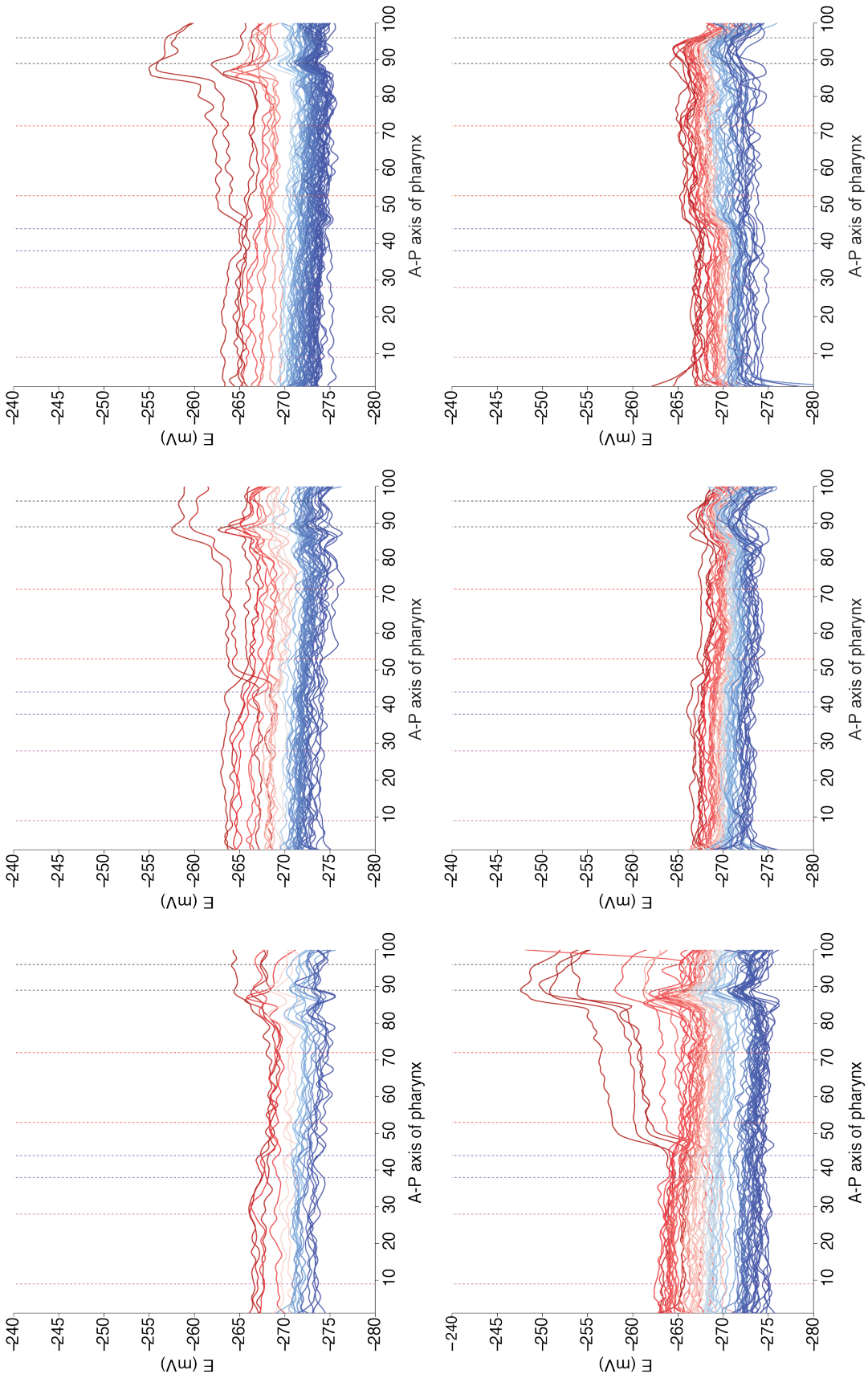
Figure 4.5: Redox profiles across the anterior-posterior axis of the pharynx in post-embryonic development.

(**Figure 4.5** *continued)* Each profile is the best-fit functional representation of the observed E values using a B-spline basis. Profiles are colored based on their average value ($\ddot{E}$). Dotted lines denote the boundaries used to quantify the redox potential of specific muscle groups: procorpus – PC, metacorpus – MC, isthmus – I, and posterior bulb – PB.

Figure 4.6: Average subtracted redox profiles across the anterior-posterior axis of the pharynx in post-embryonic development. *(following page)* Each profile is the best-fit functional representation of the observed E values using a B-spline basis, after average $(E - \bar{E})$. Profiles are colored based on their average value ($\bar{E}$). Dotted lines denote the boundaries used to quantify the redox potential of specific muscle groups: procorpus – PC, metacorpus – MC, isthmus – I, and posterior bulb – PB.
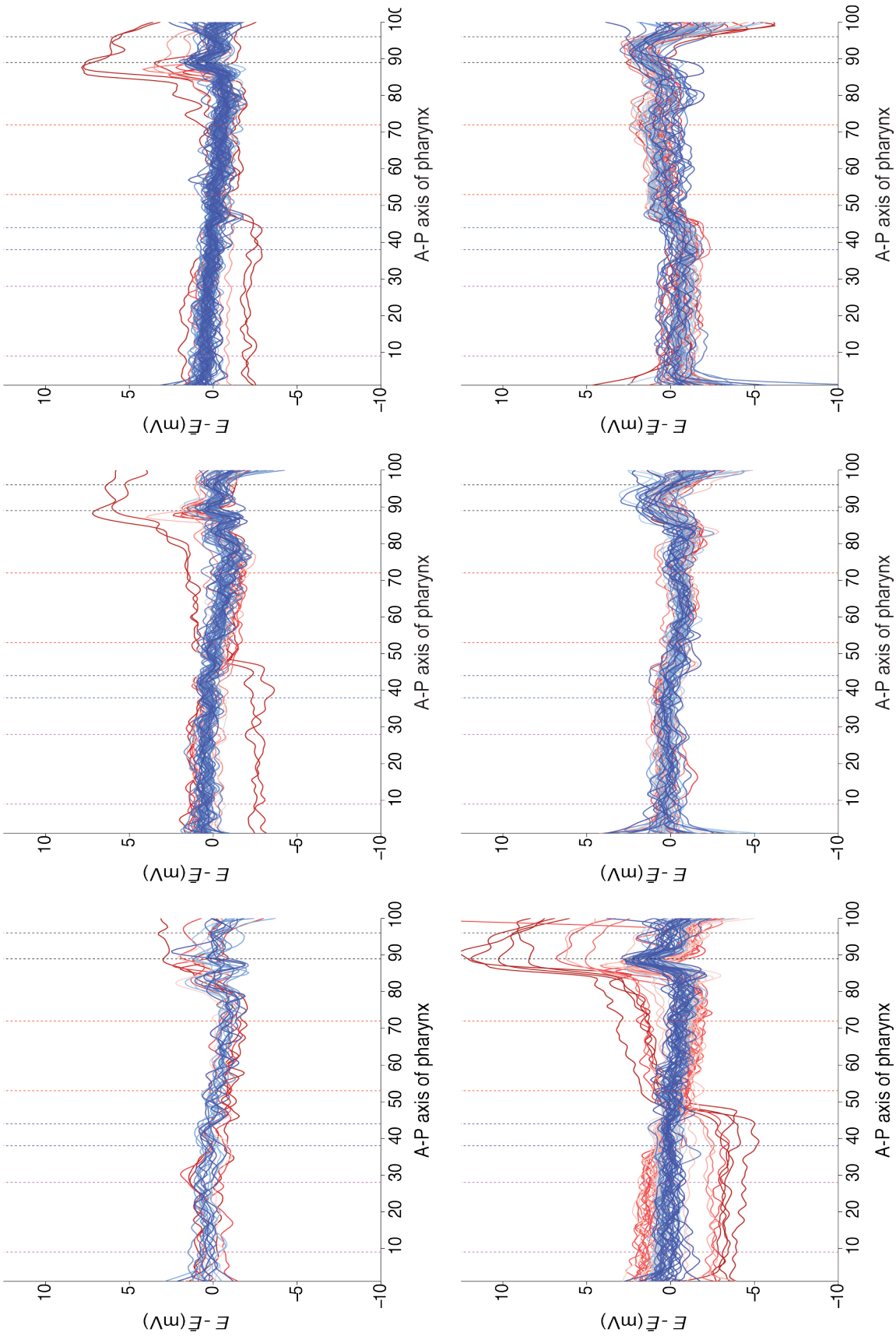
(Figure 4.6 *continued*

117

where the procorpus tends to have higher redox potential than the isthmus and the posterior bulb.

Afterwards, we examined the complete anterior-posterior profile of cytosolic redox potential for all individuals (Figure 4.5), as well as the average subtracted (Figure 4.6). In the panels for L2, L3, and L4 we note a few individuals with unusually high levels of oxidation (consider the change in the y-axis scale compared to the figures in Chapter 3). These individuals also exhibit unusually steep transitions of the redox potential between both anterior bulb and isthmus, and isthmus and posterior bulb, with differences of up to 15 mV from the anterior to the posterior end of the tissue. The sharpness of these spatial boundaries highlights the discreteness that the cytosolic E_{GSH} redox phenotype can achieve within this tissue, in spite of the gap junctions between muscle segments.

The 15 mV spatial difference in redox potential is similar in magnitude to the changes in redox potential observed in response to oxidative stress when using 5mM t-BOOH exogenously (Chapter 3). A plausible hypothesis is that these high levels of oxidation, observed in a few individuals during postembryonic development, correspond to the oxidative events associated with protein polymerization and collagen cross-linking, the last step in the maturation of the newly synthesized cuticle (Edens, et al., 2001).

The final step in collagen maturation during cuticle biosynthesis involves structural cross-linking, catalyzed mainly by the action of the dual oxidase enzyme DUOX1/BLI 3. This large, membrane-bound enzyme contains an N-terminal peroxidase domain and a C-

terminal superoxide-generating NADPH-oxidase domain. The proposed mechanism of action involves the generation of superoxide, using cytosolic NADPH, to drive the extracellular cross-link of free tyrosine and collagens (Thein et al., 2009). Although the production of the superoxide anion ($O_2^{\cdot-}$) will take place outside the cell, this reactive oxygen species is rapidly dismutated into H_2O_2, which can readily cross the cell membrane through the aquaporin channels. The superoxide anion ($O_2^{\cdot-}$) can also enter the cell membrane through anion channels like the Cl^- channel-3, ClC-3 (Fisher 2009).

There are two circumstantial points that support this hypothesis:

1) The grinder is a highly specialized pharyngeal structure that functions as the "teeth" of the worm (Figure 4.3). Composed of cuticle which is secreted mainly by the pm6 muscle segment, it is composed of serrated margins, arranged in 3-fold symmetry, that interlock and rotate when the muscles of the posterior bulb contract, macerating the food and working as a one-way valve to regulate its passage into the intestinal valve (Altun and Hall, 2009). Notice that for L2, L3 and L4, we consistently observe a small peak in oxidation in pm6 (before pixel 90). This area of higher oxidation corresponds to the expected location and shape of the grinder. Given the degree of specialization, it is reasonable to expect a dedicated process of collagen maturation in this specific region. Although the grinder is an extracellular structure, transmission electron microscopy in this area shows a highly specialized apical region in the cytosol of pm6, just under the plasma membrane immediately underlying the grinder. This specialized region of the pm6 cytosol contains an abundance of electro dense tubules and dense core

vesicles (Altun and Hall 2009). So far, we have not observed a peak in oxidation for this location of the pharynx for any other condition or in any of the measurements performed on adult individuals.

2) We observe the most dramatic phenotypes in the L4 larval stage. It is precisely in this transition that the cuticle undergoes the greatest rearrangement and specialization (Figure 4.2). While the cuticle of larval stages need only be functional for a few hours, this last molt has to produce a structure that remains functional for the entire lifespan of the worm. In the last molt the thin larval cuticle, composed of 2 layers (cortical and basal zones), is transformed into a 0.5 μm thick structure with 5 layers: a surface coat, containing glycoproteins; an epicuticle layer, containing lipids; a cortical zone, containing cuticlin and collagens; and the medial and basal zones, which also contain collagens (Cox et al., 1981).

The subpopulation that exhibits unusually high oxidation may explain the results of Knoefler et al., 2012 (reviewed in the section *"The contribution of redox biology to aging"* in the second part of this chapter). They observe a higher proportion of oxidized thiols in L4 larval stage using the OxICAT method, and an increased ratio of HyPer sensor in larval stages compared to day 2 adults.

In the near future, we would like to test whether the oxidative peaks observed in cytosolic redox potential during postembryonic development are caused by the action of NADPH

oxidases. We would do this by measuring cytosolic redox potential in *bli-3,* as well as in

other mutants known to have defects in the cuticle crosslinking.

Table 4.1 – Measurements of redox potential in feeding muscles during development and early adulthood

A) Descriptive statistics. Potentials reported as [mean ± s.d. (n), mV]

Age					
L1 (20)	-271.1±2.2	-270.7±2.1	-270.9±2.0	-271.7±2.0	-271.0±2.6
L2 (47)	-270.7±2.7	-270.3±2.6	-270.5±2.5	-271.2±2.7	-270.6±3.5
L3 (67)	-271.7±2.6	-271.4±2.5	-271.8±2.4	-272.1±2.5	-271.6±3.3
L4 (77)	-269.1±3.6	-268.9±3.5	-269.2±3.2	-269.5±3.7	-268.5±5.1
1do (62)	-270.5±1.5	-270.3±1.6	-270.3±1.6	-271.1±1.5	-270.0±1.4
2do (56)	-269.9±1.9	-270.5±1.9	-270.7±1.8	-269.4±2.2	-268.7±1.9

B) Levels

Col 1				Col 2				Col 3				Col 4				Col 5		
L4	A			L4	A			L4	A			2do	A			L4	A	
2do	A	B		1do		B		1do	A	B		L4	A			2do	A	
1do		B	C	L2		B		L2		B	C	1do		B		1do	A	B
L2		B	C	2do		B		2do		B	C	L2		B		L2		B
L1		B	C	L1	A	B		L1	A	B	C	L1		B		L1	A	B
L3			C	L3		B		L3			C	L3		B		L3		B

(levels not connected by the same letter are significantly different, Tukey HSD test, *p<0.05)*

Table 4.2 – Comparison between regions in each developmental group
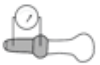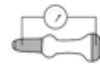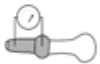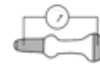
Genotype	Pharyngeal regions		L1	L2	L3	L4	1 day old	2 days old
			0.17 ± 0.7	0.20 ± 0.6	0.43 ± 0.5	0.29 ± 0.6	0.03 ± 0.3	0.25 ± 0.4
			1.00 ± 0.7	0.91 ± 0.6	0.75 ± 0.5	0.61 ± 0.6	0.83 ± 0.3	1.09 ± 0.4
wild type			0.26 ± 0.7	0.30 ± 0.6	0.21 ± 0.5	0.41 ± 0.6	0.27 ± 0.3	1.83 ± 0.4 $p<0.0001$
			0.83 ± 0.7	0.71 ± 0.6	0.32 ± 0.5	0.31 ± 0.6	0.79 ± 0.3	1.34 ± 0.4
			0.09 ± 0.7	0.10 ± 0.6	0.22 ± 0.5	0.70 ± 0.6	0.30 ± 0.3	2.07 ± 0.4 $p<0.0001$
			0.74 ± 0.7	0.61 ± 0.6	0.53 ± 0.5	1.01 ± 0.6	1.10 ± 0.3 $p<0.0006$	0.74 ± 0.4

Table 4.3 – Measurements of redox potential differences

A. Descriptive statistics. Potentials reported as [mean ± s.d. (n), mV]

Age						
L1 (20)	0.172 ± 0.36	1.001 ± 0.68	0.263 ± 1.21	0.828 ± 0.56	0.090 ± 1.19	-0.738 ± 0.87
L2 (47)	0.198 ± 0.40	0.910 ± 1.23	0.296 ± 2.01	0.712 ± 1.15	0.098 ± 1.96	-0.614 ± 1.02
L3 (67)	0.430 ± 0.44	0.746 ± 0.75	0.214 ± 1.68	0.315 ± 0.71	-0.217 ± 1.66	-0.532 ± 1.10
L4 (77)	0.294 ± 0.58	0.608 ± 1.88	-0.407 ± 3.76	0.314 ± 1.77	-0.701 ± 3.67	-1.015 ± 2.03
1do (62)	0.034 ± 0.41	0.827 ± 0.57	-0.271 ± 0.98	0.793 ± 0.51	-0.304 ± 0.97	-1.098 ± 0.70
2do (56)	0.245 ± 0.60	-1.090 ± 1.11	-1.827 ± 1.09	-1.335 ± 0.97	-2.072 ± 1.00	-0.737 ± 0.70

B. Levels

L3	A		L1	A	L2	A	L1	A	L2	A	L3	A
L4	A		L2	A	L1	A	1do	A	L1	A	L2	A
2do	A	B	1do	A	L3	A	L2	A	L3	A	2do	A
L2	A	B	L3	A	1do	A	L3	A	1do	A	L1	A
L1	A	B	L4	A	L4	A	L4	A	L4	A	L4	A
1do		B	2do	B	2do	B	2do	B	2do	B	1do	A

(levels not connected by the same letter are significantly different, Tukey HSD test, *p<0.05)*

124

Chapter 4 – Part 1

Methods

We synchronized 1- and 2-day-old adults by picking late L4, using vulva morphology as a marker. For larval stages, we picked animals with approximately the expected size and morphology for each larval stage. After immobilization[11], we staged them using transmitted light microscopy and used the protocol of image acquisition and image analysis, described previously in Chapter 3. Due to the different sizes of tissue in each larval stage, and the associated differences in integrated fluorescence intensity, we adjusted exposure times to obtain similar counts of intensities across the 6 groups measured. Also, because of these size differences, we extracted the anterior-posterior profiles of intensities using a line width of 5.16 μm (4 pixels) for the 2x2 binning images, instead of the 7.74 μm used previously in adults.

---

[11] The time in anesthesia before imaging – between 80 and 120 minutes for the experiments with 2-day-old adults described in Chapter 3– is a considerable fraction of the total length of each larval stage, therefore we shortened the time in anesthesia for this experiment to 55 to 95 minutes.

Chapter 4

Part 2 – Age-dependent changes in cytosolic redox potential are regulated by insulin signaling

Genetic studies of aging

Aging has fascinated human thinkers since time immemorial, and probably in every culture around the world. However, the study of the genetics of aging really began only a few decades ago, after it was discovered that a single-point mutation could double the lifespan of an organism. Before this time, biological aging was considered to be merely a passive process, a description of the wear and tear expected to occur in any machine or ordered system, whether alive or inert. It was thought that the death of an organism took place through an arbitrary sequence of events; that this entropic process was intractable or futile to study; and, most importantly, that it could not be altered by genetic means. Indeed, from the point of view of evolutionary biology, it was commonly accepted that any process taking place after reproduction, such as aging, could not possibly respond to selective pressure, and therefore could not have evolved to be under genetic regulation.

In the 1970s, this notion began to be challenged (Goodrich, 1975). In 1977, Michael Klass performed the first genetic screen looking for long-lived mutants in *C.elegans* (Klass 1977; Klass 1983). His elegant work set the stage, conceptually and methodologically, for the study of longevity in the worm. He first established that environmental factors, such as diet and temperature, have considerable effect on the

lifespan of the worm. As was observed for rodents in the 1930s, dietary restriction also extended the lifespan of the worms, which hinted at the evolutionary conservation of some of the physiological mechanisms affecting aging. He also showed that the worms retain memory of the temperature in which they grew, and this memory affects the lifespan of the adult (Klass 1977).

Although Klass successfully isolated strains with extended longevity, he did not follow through to the characterization of such mutants. Instead, he dismissed the result with the hypothesis that these mutations only affected life span indirectly, by causing metabolic changes. As he elegantly put it: "*On the one hand, there is the belief that aging is simply the result of the conglomerate of biochemical reactions within the organism and that life span is directly coupled to this metabolic rate. The alternative hypothesis is that life span is controlled by a limited number of very specific "life span" genes.*" (Klass 1977). He interpreted his results in favor of the first hypothesis.

A turning point occurred when it was proven that a single point mutation could double the lifespan of *C. elegans* (Kenyon et al., 1993). In the years that followed, the joint effort of several groups of researchers elucidated other genes involved in the pathway, establishing their molecular identities: *daf-2* was the insulin receptor, *age-1* was the phosphatidyl inositol 3-kinase (PI3K kinase), and *daf-16* was a forkhead-family FOXO transcription factor (Morris et al. 1996; Kimura et al. 1997; Lin et al. 1997; Ogg et al. 1997). The sequence identification of the forkhead-family (FOXO) transcription factor DAF-16 was also a valuable contribution to the scientific community studying diabetes

and cancer, since it was the first transcription factor known to be downstream of insulin signaling (Kenyon 2011).

The discovery that insulin signaling is a pathway involved in lifespan determination was a breakthrough. Later, the effect of insulin receptor activity in lifespan modulation for *Drosophila* and mice confirmed the evolutionary conservation of this mechanism (Clancy et al., 2001; Tatar et al., 2001; Holzenberger et al., 2003; Bluher et al., 2003). It has also been shown that the level of circulating IGF-1 of 30 inbreed lines of mice is inversely correlated with lifespan (Leduc et al., 2010). Candidate gene studies in humans also support the involvement of insulin signaling in human longevity, although the effects of orthologous genes are small (Slagboom, et al., 2011). Polymorphisms in the FOXO transcription factors sequences has been linked to longevity in very diverse human populations, while impaired IGF-1 receptor has been genetically linked to centenarians in populations of Ashkenazi Jews (Kojima et al., 2004; Willcox et al. 2008; Anselmi et al., 2009; Flachsbart et al., 2009; Li et al., 2009).

The role of insulin signaling in aging was the first indication that genes with roles in nutrient sensing and energy regulation could also affect the rate of aging. Other signaling pathways, such as TOR kinase pathway, have since been shown to modulate aging as well (Jia et al., 2004; Kapahi et al., 2004; Harrison et al., 2009). The fact that these signaling pathways affect the rate of aging in an evolutionarily conserved manner redefined the aging field and laid the groundwork for understanding the molecular basis of aging in humans.

The study of age-related changes in *C. elegans*

The aging process is the progressive accumulation of degenerative changes that leads to a loss of functionality in an organism. At the level of a population, aging can be defined precisely as a time-dependent acceleration in the probability of dying. At an individual level, however, the 'aging phenotype' is still poorly defined. To say the least, it is unclear what variables can be measured in order to assess how old or young an individual is, let alone predict its probabilities of survival.

One of the difficulties is that aging occurs at all scales of biological organization: the accumulation of degenerative changes can be observed at molecular, cellular, physiological, organismal and behavioral levels. It is a challenging question to answer how changes of organization at the molecular and cellular scales translate into physiological, organismic and behavioral changes related to aging. It would be particularly useful to have observables to help us bridge this gap between these microscopic and macroscopic levels of organization.

Ideally, we would like to have observables 1) at an intermediate level between molecular changes and organismal changes, such us cell-level or tissue-level phenotypes; 2) that are time-dependent variables; and 3) that can be measured in individual worms in a nondestructive manner, allowing us to investigate how the present physiological state of an organism, while it is alive, relates to its future life expectancy. We attribute great importance to this last point, as a tool for studying the causal mechanisms in aging.

In natural populations, the variability of lifetime distributions may arise from a combination of genetic and environmental factors. However, even isogenic populations raised in a common environment and protected from extrinsic mortality have a marked variability in lifespan. Even under optimal growing conditions, the variability of lifespan in worms is as much as three-fold (Kirkwood et al., 2005). This variability is thought to be caused by the stochastic nature of cellular and molecular mechanisms that control the rate of aging. Because of their non-destructive nature, *in vivo* measurements of cytosolic redox potential in *C.elegans* provide an excellent opportunity to investigate the correlation between this variable and the remaining lifespan observed in single individuals.

The contribution of redox biology to aging

Historically, the role of biological oxidation has been prevalent in our explanation of aging. It is fairly intuitive, after all: over time metals get rusty, oils get rancid, humans grow old. The first connection between oxidation and longevity was made in 1908 by Max Rubner. In the era following the Industrial Revolution, it had become evident that the more a machine works, the sooner it will wear out. Rubner extended this idea to living systems, proposing that metabolic rate, as a measure of the work performed by an animal, is linked to how long it will live. The idea that oxygen consumption and basal metabolic rates were inversely proportional to maximal lifespan gained significant momentum in 1928, when Raymond Pearl published the book *The Rate of Living*. Then, in the 1950s Denham Harman provided a mechanistic link between energy metabolism

and aging (Harman, 1956): the "Free-radical theory of aging" proposes that free-radical species, produced by aerobic metabolism, cause oxidative damage to macromolecules, and that the accumulation of this damage over time causes aging. Since then, this 'radical' idea has provoked much thought. The theory has been extended to include radical and non-radical oxidants and refined to incorporate mechanistic insight into how endogenous sources of oxidants, such as the Electron Transport Chain in mitochondria (Harman, 1972), can affect the structure and function of the cell over time.

However, the prediction that changing the rate in which oxidative damage accumulates can affect lifespan does not hold. During the past decade, evidence against oxidative damage in macromolecules as a causal factor of aging has been growing. In the worm, for instance, treatments that increase levels of reactive oxygen species (ROS) or levels of oxidative damage extend lifespan, rather than to shorten it (Schulz et al., 2007; Heidler et al., 2010; Van Raamsdonk and Hekimi, 2012). Manipulation of antioxidant enzymes, such as overexpression of catalase, cytoplasmic superoxide dismutase (Cu/Zn SOD), and mitochondrial superoxide dismutase (MnSOD), alone or in combination, has little or no effect on lifespan in mice (Perez et al., 2009a; Perez et al., 2009b). In humans, large-scale intervention trials with scavenging antioxidant supplements show inconclusive, sometimes even detrimental, results (Jones, 2008). Some argue that one of the difficulties with such experiments is the lack of specificity in the subcellular compartments being targeted; for example, an antioxidant treatment meant to protect against molecular damage in the cytosol could induce ER stress.

An alternative hypothesis for the role of redox biology in the aging process, termed the

"Redox hypothesis", focuses on the regulatory role of oxidative modification in cellular

regulation (Jones, 2008). It proposes that alterations in redox biology affect aging, not

through the accumulation of unspecific oxidative damage, but through the de-regulation

of redox switches in the cell. Redox modifications of proteins are often used as

mechanisms to regulate the activity, interactivity, structure and stability of proteins

(Herrmann and Dick, 2011). Redox sensitive thiols are critical components of regulatory

mechanisms in many cellular processes, such as signaling (e.g. Ras, PTP-1B),

transcription factor activity (e.g. Nrf-2, nuclear factor - κB), receptor activation (e.g.

Insulin receptor, αIIβ3 integrin in platelet activation), etc. The redox activity of these

elements needs to be coordinated by redox control nodes (e.g., thioredoxin, GSH) which

are spatially and kinetically isolated. Jones 2008 proposes that the disruption of this redox

circuits by either the specific reaction with a particular redox-sensitive thiol switch, or by

the global changes in the redox control nodes, is central to aging and age-related diseases.

Previous studies in *C. elegans* show that the GSH total concentration decays with age

faster in wild type that in *daf-2(e1370)* (Brys et al., 2007). More recently, Back et al.,

2012 and Knoefler et al., 2012 have used the roGFP2_Grx1 and HyPer sensors *in vivo* to

estimate GSH/GSSG and H_2O_2 levels, respectively. In Chapter 2 we discussed the

chemical mechanisms of these two sensors, the interpretation of such measurements, and

some technical considerations about their methodology. In this chapter we will briefly

summarize their results:

1) Back *et al.*, 2012 used the HyPer sensor (a cyclically permutated YFP designed to measure H_2O_2,) and the roGFP2_Grx1 sensor (a modified version of roGFP fused to human Glutaredoxin 1) to assess the oxidative status of worms during development and aging. They expressed these sensors ubiquitously under the large ribosomal subunit L17 protein (*rpl-17*) promoter. Based on spectrophotometric measurements of populations, they report a decline in GSSG/2GSH ratios during larval development, which stays at similar levels in 0 and 1 days old adult populations. However, they could not measure roGFP2_Grx1 during aging due to decreased expression levels of the roGFP2_Grx1 sensor, and an increase in autofluorescence level in adult populations. They also inspected individual worms through confocal microscopy, and report lower ratios of GSSG/2GSH in spermatheca compared to the total ratiometric value for the whole. To draw this conclusion, however, the authors only used 4 worms for statistical comparison.

With the HyPer sensor, based on spectrophotometric measurements of populations, they report: *a)* similar[12] levels of H_2O_2 between L2, L3, L4, 0 and 1-day-old adults, suggesting stable levels of H_2O_2 during postembryonic development and early adulthood; and *b)* an increase in the levels of H_2O_2 between day 1 and day 7. They observe that this effect is delayed in populations under dietary restriction. Next, they used confocal microscopy to inspect individual worms expressing HyPer. For young individuals, they report spatial differences in the HyPer ratio in canal associated neurons, body-wall muscle and hypodermis, compared to the total ratio for the animal. The authors based this statistical comparison on the quantitation of 9 individuals. For the HyPer sensor they also used

---

[12] The two studies, using the same genetic strain *jrIs1[Prpl-17::HyPer]*, show conflicting results in this regard.

confocal microscopy to measure the ratiometric values for young (day 0) and old individuals (day 6). They report a "remarkable population heterogeneity" in the H_2O_2 levels and its spatial distribution in old individuals. In Figure 3B they document this variability, without further quantitation, using a colormap image of a mixed population of young and old individuals expressing the HyPer sensor.

2) Knoefler et al., 2012 expressed the HyPer sensor in the body-wall muscle(using the *unc-54* promoter) and ubiquitously (using the *rpl*-17 promoter). For the latter case, they used the genetic strain built by Back et al., 2012 (*jrIs1[Prpl-17::HyPer]*). In both transgenes they observe higher H_2O_2 levels during postembryonic development than during adulthood[2]. They also quantify the levels of peroxides in worm extracts, using Amplex UltraRed reagent, and confirm that L3 larvae exhibit a 40-fold increase in peroxide level, compared to 2-day-old adults.

During wild type aging each transgene shows different results: the *unc-54::HyPer* shows no difference between ages 2, 8, 15 and 20 days old (at 15°C); while the *Prpl-17::HyPer* shows a gradual age-dependent increase in ratio, though all values in adulthood are lower than the levels measured in larval stages. Additionally, they compared the measurements of *unc-54::HyPer* in wild-type, *daf-2* mutants and *daf-16* mutants, showing how insulin pathways affect the levels of H_2O_2 in body wall muscle during adulthood.

This group also performed proteomic measurements of thiol oxidation in worm extracts using the OxICAT method, providing a list of 170 proteins with their respective

thiol/disulfide ratio for each cysteine detected. Many of the proteins identified were known to contain cysteines that are sensitive to oxidation; others were shown for the first time to be redox sensitive. Interestingly, they identified as redox sensitive the Phosphoinositide 3-kinase AGE-1, protein involved in insulin signaling, and whose deletion confers lifespan extension.

During postembryonic development, they observe a higher level of thiol oxidation in L4 larval stages measured with the OxICAT method, consistent with the HyPer measurements discussed above. From these results they conclude that "oxidative stress is an early event in life". An alternative explanation is that this increase in thiol oxidation is part of the developmental program of the worm, as each molting process requires extensive crosslinking of collagen molecules in their cuticle – a structure which is synthesized continuously, and replaced every 8 to 10 h during larval development.

This proteomic study shows no significant increase in the level of thiol oxidation between day 2 and day 8 of adulthood, but shows a significant increase between day 2 and day 15 (for worms growing at 15°C). From the 170 total proteins identified through the OxICAT method, 19 were identified as cytosolic proteins expressed in pharynx, and six 6 of them showed a 1.5 fold increase in their cysteine oxidation level from day 2 to day 8 of adulthood.

These two pieces of work, in particular the proteomic results using the OxICAT technique, set the expectation that differences in E_{GSH} potential would be observed during development and aging.

Chapter 4 – Results

Part 2 – Age-dependent changes in cytosolic redox potential are regulated by insulin signaling

During adulthood, the pharynx exhibits noticeable morphological and functional changes, suggestive of progressive decline (Huang et al., 2004; Johnston et al., 2008). We first quantified the functional changes of this tissue by measuring the pharyngeal pumping rates in single individuals, longitudinally throughout their adulthood (Figure 4.7). 2-day-old adults displayed pharyngeal pumping rates of 157 ± 50 pumps per minute; the pumping rate increased to 228 ± 19 pumps per minute by day 3, a period that coincides with the maximum rate of reproduction at $20\°C$ (Klass, 1977). After this point, the pharyngeal pumping rates decline gradually from day 3 to day 10 of adulthood, when it plateaus at around 35 pumps per minute (Table 4.4). By day 10, while 95% of the population is still alive, 30% of the worms feed very slowly and 20% do not to feed at all (Figure 4.7). We chose to focus in the first 10 days of adulthood, an age-range where we observe the majority of functional changes taking place.

To quantify the impact of aging on the cytosolic redox environment *in vivo*, we measured E_{GSH} in the pharyngeal muscles of wild-type animals and long-lived *daf-2(e1370)* mutants, using synchronous adult populations from day 1 to day 10 of adulthood. We find that in wild-type animals E_{GSH} exhibits a complex age-dependent

dynamic, whose main features involve a first peak in E_{GSH} levels by day 3, and a second yet smaller peak by day 9 (Figure 4.8). We also observe a three-fold increase in E_{GSH} variance from day 2 to day 8 (Table 4.5); as a result, a significant proportion of older animals exhibit E_{GSH} levels lower than on day 1.

In contrast to wild-type animals, *daf-2* mutants exhibit a clearer age-dependent phenotype: E_{GSH} decreases monotonically during the first 10 days of adulthood. Under diminished insulin signaling, the cytosolic E_{GSH} decreases sharply from day 2 to day 5, and more gradually thereafter (Figure 4.8). Depending on the muscle segment, these changes represent a 4 to 7 mV decrease in average E_{GSH} from day 1 to day 10 in *daf-2*
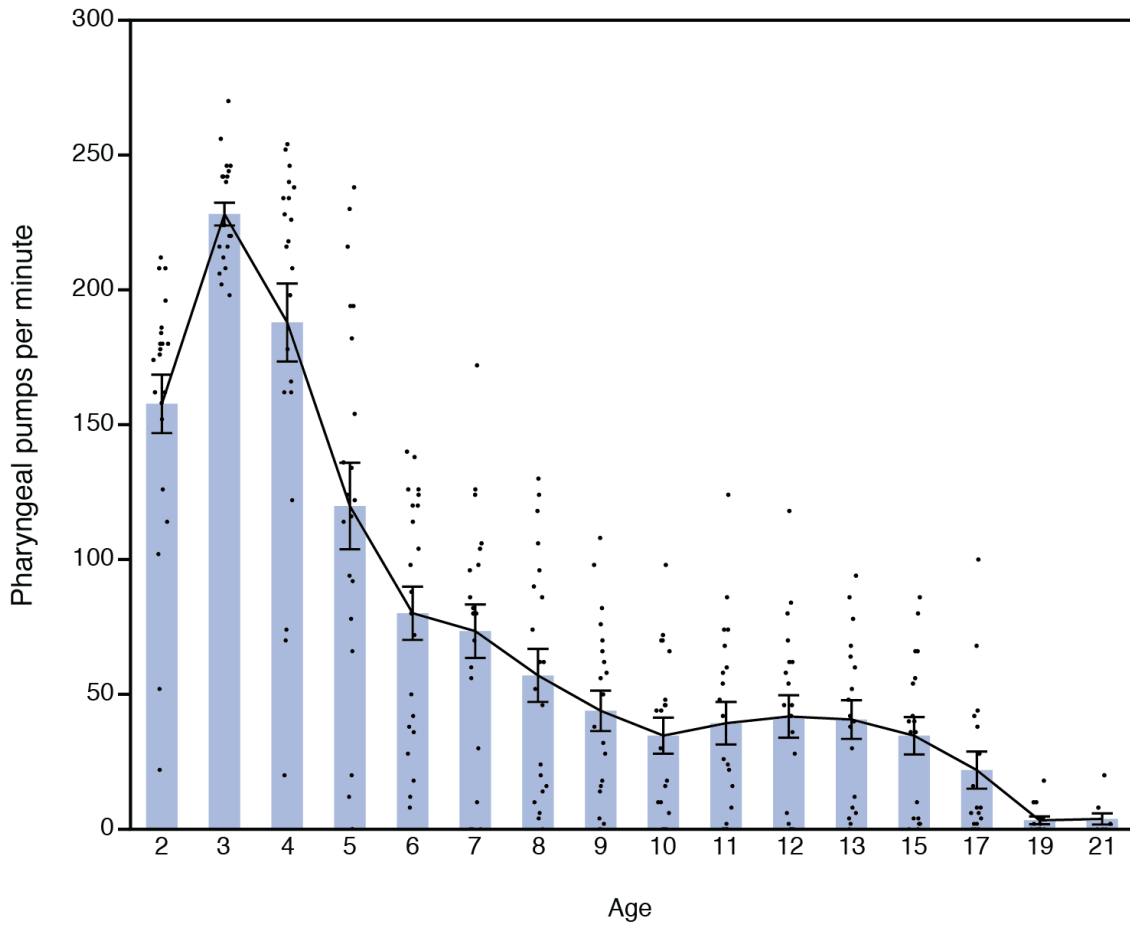
Figure 4.7: Age-dependence of pharyngeal pumping rate. Pumps-per-minute, where tracked in single individuals during the first 20 days of adulthood (n=20, Table 4.4). The peak around day 3 coincides with the reproductive peak.

mutants (Table 4.6); thus, the difference in average E_{GSH} between *daf-2* mutants and wild-type animals triples during that period. These results generalize the effect we see in 2-day-old *daf-2* mutants (Chapter 3) to other ages: decrease in insulin signaling causes a progressively more reducing cytosolic environment through the first 10 days of adulthood.

We also examined how aging and insulin/IGF-1 signaling affects the spatial differences in the pharyngeal redox environment. Differences in E_{GSH} between muscles of the same pharynx exhibit simpler age-dependencies, which are unique for each pair of muscles (Figure 4.9). For example, between posterior bulb and procorpus muscles in wild-type animals, ΔE_{GSH} increases 2.6 mV monotonically from day 1 to day 8, and decreases slightly thereafter. In *daf-2(e1370)* mutants, these spatial E_{GSH} differences exhibit a similar trends (Figure 4.9, Table 4.7), but have a more positive values at all ages. This suggests that, at all ages, *daf-2* normally functions to promote a more oxidative environment in posterior compared the anterior muscles.

Once we determined there was age-dependence to changes in the pharyngeal cytosolic redox environment, we were eager to test whether those changes were mechanistically linked to the process that determines lifespan. We measured E_{GSH} in 141 day 6 days-old individuals, recovered the animals after microscopy, and determined their lifespans. We found that the absolute E_{GSH} in procorpus, isthmus and posterior bulb muscles have no correlation with remaining lifespan (Figure 4.8). Surprisingly, however, we found that the anterior-posterior difference in potential between certain pairs of muscle segments did

show a correlation with remaining lifespan (Figure 4.9). We discovered that knowing the difference in E_{GSH} between procorpus and isthmus, or between procorpus and posterior bulb, reduces the uncertainty of the remaining lifespan by 18% to 20%. In contrast, the E_{GSH} differences between isthmus and posterior bulb muscles have no correlation with remaining lifespan. The results suggests two possibilities: either the differences in E_{GSH} between muscle segments is a causative factor of aging, or a shared regulatory mechanism mediates the probability of survival and the spatial differences in the redox potential in the pharynx. We think the second alternative is more likely.
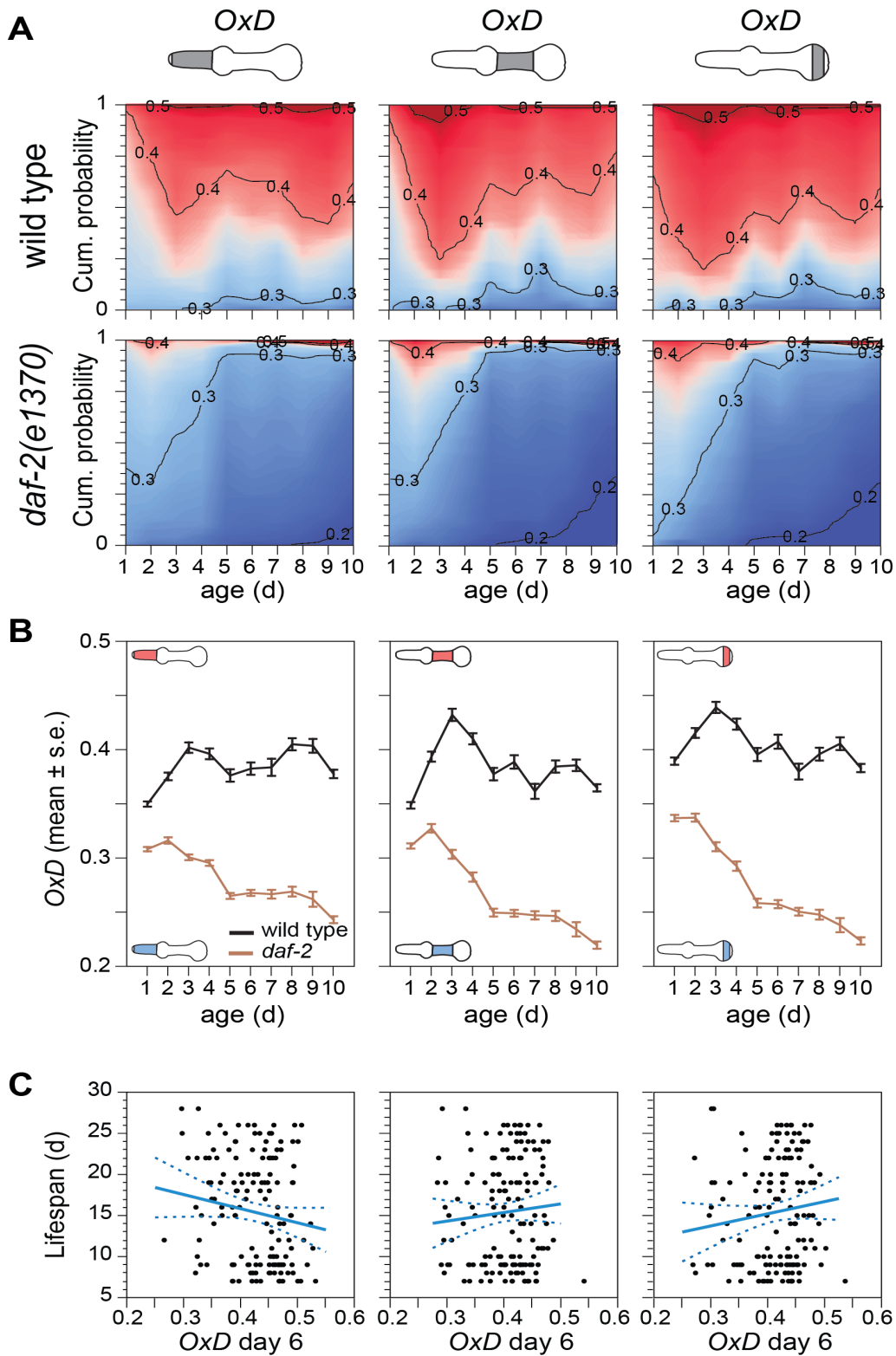
Figure 4.8: Insulin signaling modulates the age-dependent changes of the cytosolic

redox environment A) Contour maps of oxidation levels – data presented in fraction of

(Figure 4.8 *continued*) protein oxidized, OxD_{roGFP}– procorpus, isthmus and posterior bulb of wild-type and *daf-2(e1370)* mutant. (B) Oxidation levels, per age, in the two genotypes. Average levels for the distributions are plotted in panel A. Error bars show the 95% confidence interval. For statistical comparisons see Tables 4.5 and 4.6. (C) Scatter plots for the fraction of protein oxidized and remaining lifespan quantified in 6-day-old adults. Linear regression best-fits are shown as solid lines bounded by dashed lines denoting the 95% confidence interval of the fit. Non-significant correlations (p>0.0001) are shown in blue.
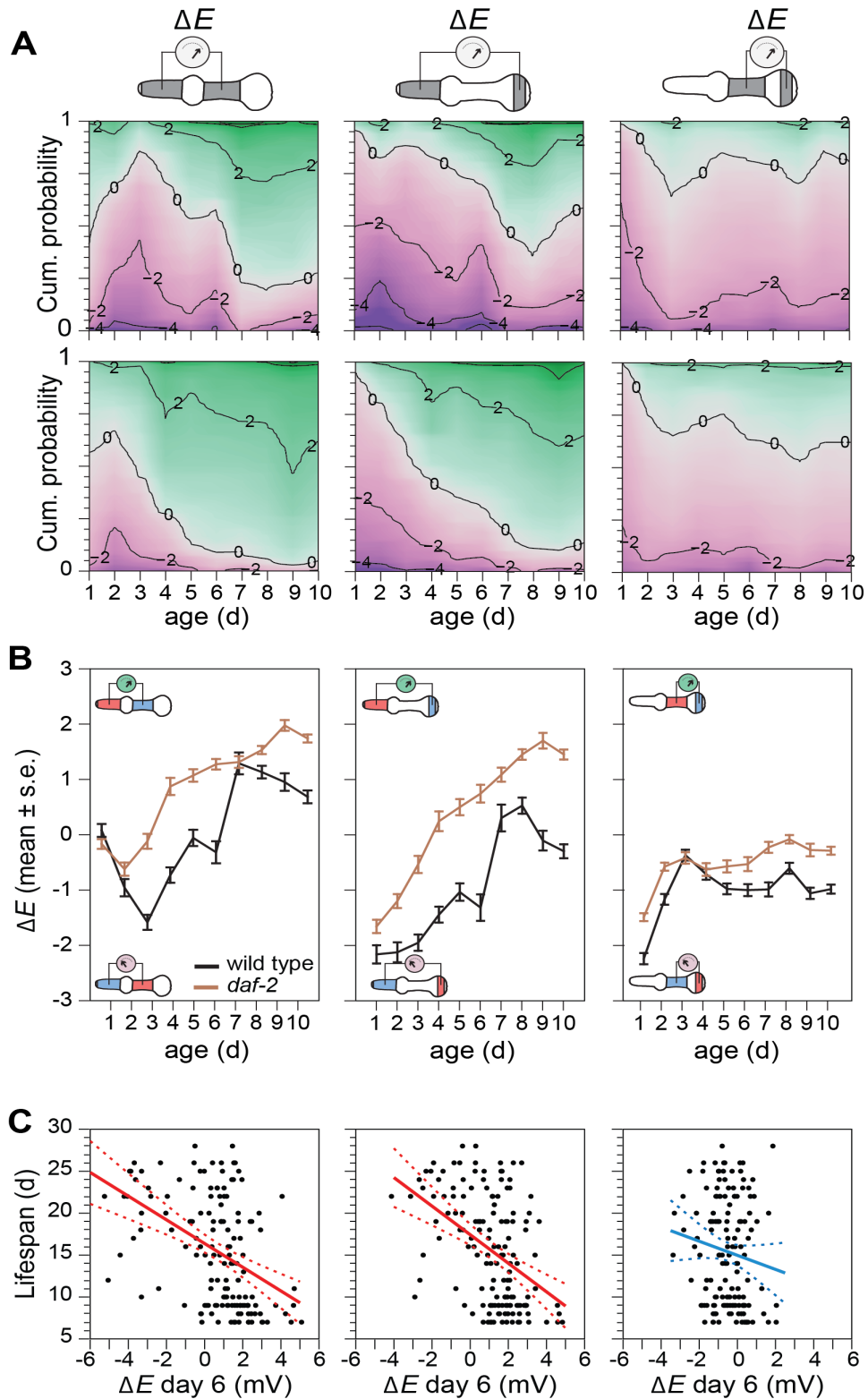
Figure 4.9: Anterior-posterior differences in redox potential are correlated with remaining lifespan. (A) Redox potential differences between regions change with age.

143

(**Figure 4.9** *continued)* Differences in redox potential are presented in the contour map as isopotential lines in mV. (B) Changes in the average redox potential differences shown between pairs of muscle segments for wild-type and *daf-2(e1370).* Average levels for the distributions plotted in panel A. Error bars are the 95% confidence interval. Negative values denote lower oxidation level in the anterior regions than in the posterior, and positive values denote higher oxidation level in the anterior regions than in the posterior. For statistical comparisons see Tables 4.7. (C) Scatter plots for the anterior-posterior redox potential difference and remaining lifespan quantified in 6-day-old adults. Linear regression best-fits are shown as solid lines bounded by dashed lines denoting the 95% confidence interval of the fit. Statistically significant correlations in red (p<0.0001) Non-significant correlations (p>0.0001) shown in blue. ΔE_{PC-I}, R^2= 0.20 p<0.0001; ΔE_{PC-PB}, R^2= 0.18 p<0.0001; n=141.

Table 4.4 – Age-related changes in pharyngeal pumping rates

Age *days*	Number alive	Pumps per minute *mean ± s.d.*
2	21	158 ± 50
3	21	228 ± 19
4	21	188 ± 66
5	21	120 ± 74
6	21	80 ± 45
7	21	73 ± 45
8	20	57 ± 44
9	20	44 ± 34
10	20	35 ± 30
11	20	39 ± 35
12	19	42 ± 34
13	18	41 ± 31
15	18	35 ± 29
17	17	23 ± 29
19	14	3 ± 6
21	10	4 ± 7

Table 4.5 – Redox potential changes during adulthood in wild-type

A) Descriptive statistics. Potentials reported as [mean ± s.d. (n), mV]

Level				
1 (91)	−272.6 ± 1.3	−272.9 ± 1.3	−273.0 ± 1.6	−270.7 ± 1.7
2 (140)	−270.9 ± 2.4	−271.5 ± 2.3	−270.6 ± 2.9	−269.4 ± 2.8
3 (78)	−269.4 ± 2.6	−270.1 ± 2.5	−268.7 ± 2.8	−268.3 ± 2.5
4 (96)	−270.0 ± 2.6	−270.4 ± 2.6	−269.7 ± 2.7	−269.0 ± 2.6
5 (101)	−271.5 ± 3.1	−271.5 ± 3.1	−271.5 ± 3.2	−270.5 ± 3.3
6 (88)	−270.9 ± 2.9	−271.2 ± 2.9	−270.9 ± 3.2	−269.9 ± 3.3
7 (92)	−271.6 ± 4.0	−271.1 ± 4.6	−272.3 ± 3.8	−271.3 ± 3.9
8 (115)	−270.5 ± 2.8	−270.0 ± 2.9	−271.0 ± 2.9	−270.5 ± 3.2
9 (96)	−270.4 ± 3.0	−270.0 ± 3.3	−271.0 ± 2.8	−269.9 ± 3.1
10 (159)	−271.9 ± 2.8	−271.7 ± 3.0	−272.4 ± 2.7	−271.5 ± 3.0

B) Levels

3	A				8	A				3	A				3	A			
4	A	B			9	A				4	A	B			4	A	B		
9	A	B	C		3	A	B			2		B	C		2	A	B	C	
8	A	B	C		4	A	B	C		6		B	C		6		B	C	D
2		B	C		7	A	B	C	D	8			C		9		B	C	D E
6		B	C	D	6	A	B	C	D	9		B	C	D	8			C	D E F
5			C	D E	5		B	C	D	5			C	D E	5			C	D E F
7			C	D E	2			C	D	7				D E F	1				D E F
10				D E	10				D E	10				E F	7				E F
1				E	1				E	1				F	10				F

(levels not connected by the same letter are significantly different, Tukey HSD test,
p<0.05

Table 4.6 – Redox potential changes during adulthood in *daf-2(e1370)* mutants

A) Descriptive statistics. Potentials reported as [mean ± s.d. (n), mV]

Level				
1 (72)	-275.3 ± 1.2	-275.6 ± 1.2	-275.4 ± 1.4	-274.0 ± 1.5
2 (150)	-274.6 ± 2.3	-274.9 ± 2.0	-274.3 ± 2.7	-273.7 ± 2.5
3 (100)	-275.7 ± 1.9	-275.7 ± 1.6	-275.6 ± 2.4	-275.2 ± 2.4
4 (100)	-276.4 ± 1.9	-276.1 ± 1.5	-277.0 ± 2.5	-276.3 ± 2.6
5 (85)	-278.5 ± 2.0	-278.1 ± 1.8	-279.1 ± 2.4	-278.5 ± 2.7
6 (100)	-278.4 ± 1.9	-277.8 ± 1.8	-279.1 ± 2.1	-278.6 ± 2.5
7 (94)	-278.5 ± 2.4	-277.9 ± 2.5	-279.3 ± 2.4	-279.1 ± 2.3
8 (117)	-278.5 ± 2.6	-277.9 ± 2.6	-279.4 ± 2.7	-279.3 ± 2.7
9 (106)	-279.2 ± 4.2	-278.3 ± 4.4	-280.3 ± 4.3	-280.0 ± 4.3
10 (92)	-279.5 ± 3.3	-278.8 ± 3.2	-280.5 ± 3.6	-280.2 ± 3.5

B) Levels

Column 1					Column 2					Column 3					Column 4				
2	A				2	A				2	A				2	A			
1	A	B			1	A	B			1	A	B			1	A	B		
3		B			3	A	B			3		B			3		B	C	
4		B			4		B			4			C		4			C	
6			C		6			C		5				D	5				D
5			C		8			C		6				D	6				D
8			C		7			C		7				D E	7				D E
7			C		5			C		8				D E	8				D E
9			C		9			C		9				D E	9				E
10			C		10			C		10				E	10				E

(levels not connected by the same letter are significantly different, Tukey HSD test, p<0.05

147

Table 4.7 – Difference in potential between pharyngeal regions

Genotype	wild type			daf-2		
1	0.08 ± 1.1	-2.24 ± 1.0	-2.16 ± 1.6	-0.13 ± 0.9	-1.42 ± 0.7	-1.55 ± 1.2
2	-0.96 ± 1.9	-1.17 ± 1.1	-2.12 ± 2.1	-0.62 ± 1.4	-0.59 ± 0.9	-1.21 ± 1.5
3	-1.48 ± 1.3	-0.38 ± 0.8	-1.85 ± 1.3	-0.11 ± 1.3	-0.40 ± 1.0	-0.51 ± 1.5
4	-0.73 ± 1.4	-0.71 ± 0.9	-1.44 ± 1.4	0.90 ± 1.6	-0.63 ± 1.1	0.26 ± 1.8
5	-0.06 ± 1.5	-0.98 ± 1.0	-1.04 ± 1.6	0.99 ± 1.2	-0.60 ± 1.1	0.38 ± 1.5
6	-0.32 ± 1.9	-1.00 ± 1.0	-1.32 ± 2.2	1.27 ± 1.0	-0.53 ± 1.3	0.74 ± 1.6
7	1.25 ± 1.9	-0.99 ± 1.2	0.26 ± 2.4	1.34 ± 1.1	-0.22 ± 1.0	1.12 ± 1.3
8	1.02 ± 1.4	-0.51 ± 1.2	0.51 ± 1.8	1.47 ± 0.9	-0.05 ± 1.0	1.42 ± 1.3
9	0.95 ± 1.6	-1.06 ± 1.0	-0.11 ± 1.8	1.96 ± 1.0	-0.26 ± 1.2	1.71 ± 1.5
10	0.72 ± 1.7	-0.97 ± 1.1	-0.24 ± 1.9	1.68 ± 1.1	-0.31 ± 1.1	1.37 ± 1.3

Author contributions

Catalina Romero (C.R.) and Javier Apfeld (J.A.) designed the research; C.R. performed research; C.R., J.A. and Walter Fontana (W.F.) analyzed data; C.R. wrote the text.

Chapter 4 –Part 2

Methods

For the measurements of cytosolic E_{GSH} presented in section 4.2 we performed every step in parallel for wild-type and *daf-2(e1370)* mutants. We synchronized adults of both genotypes by picking late L4, using vulva morphology as a marker. We used an immobilization range between 60 to 130 minutes and used the protocol of image acquisition and image analysis, described previously in Chapter 3. In each age group, the *daf-2(e1370)* mutant exhibits lower levels of *pmyo2::roGFP1_R12* expression compared to wild-type. Likewise, older individuals show lower levels of expression compared to young individuals, for each genotype. To ensure consistency in image analysis, we adjusted exposure times to obtain similar counts of intensities across all the groups measured. The *daf-2(e1370)* mutant also exhibits morphological differences in pharynx compared to wild type; this mutant has longer and thinner pharynxes, so that the aspect ratio of the tissue changes, but the volume of the tissue seems to be invariant. For this reason, we performed two additionally steps in the supervision of the automated image analysis: 1) because the isthmus is narrower in the *daf-2(e1370)* mutant, we double check that the polyline defining the medial axis across this portion of the tissue will be well centered; 2) we confirmed that the boundaries delimiting each muscle segment hold equally for *daf-2(e1370)* mutants and for wild-type.

References

1.   A.F. Bird, J. Bird, The structure of nematodes. (Academic Press, California, 1991).

2.   R. G. Allen, A. K. Balin, Oxidative influence on development and differentiation: an overview of a free radical theory of development. Free radical biology and medicine 6, 631 (1989).

3.   Z. F. Altun, D. H. Hall, in WormAtlas L. A. Herndon, Ed. (2009).

4.   C. V. Anselmi et al., Association of the FOXO3A locus with extreme longevity in a southern Italian centenarian study. Rejuvenation research 12, 95 (Apr, 2009).

5.   P. Back et al., Exploring real-time in vivo redox biology of developing and aging Caenorhabditis elegans. Free radical biology and medicine 52, 850 (Mar 1, 2012).

6.   M. Bluher, B. B. Kahn, C. R. Kahn, Extended longevity in mice lacking the insulin receptor in adipose tissue. Science 299, 572 (Jan 24, 2003).

7.   K. Brys, J. R. Vanfleteren, B. P. Braeckman, Testing the rate-of-living/oxidative damage theory of aging in the nematode model Caenorhabditis elegans. Experimental gerontology 42, 845 (Sep, 2007).

8.   J. Cai, D. P. Jones, Superoxide in apoptosis. Mitochondrial generation triggered by cytochrome c loss. The Journal of biological chemistry 273, 11401 (May 8, 1998).

9.   D. J. Clancy et al., Extension of life-span by loss of CHICO, a Drosophila insulin receptor substrate protein. Science 292, 104 (Apr 6, 2001).

10.   G. N. Cox, M. Kusch, R. S. Edgar, Cuticle of Caenorhabditis elegans: its isolation and partial characterization. The Journal of cell biology 90, 7 (Jul, 1981).

11.   W. A. Edens et al., Tyrosine cross-linking of extracellular matrix is catalyzed by Duox, a multidomain oxidase/peroxidase with homology to the phagocyte oxidase subunit gp91phox. The Journal of cell biology 154, 879 (Aug 20, 2001).

12.   A. B. Fisher, Redox signaling across cell membranes. Antioxidants and redox signaling 11, 1349 (Jun, 2009).

13.   F. Flachsbart et al., Association of FOXO3A variation with human longevity confirmed in German centenarians. Proceedings of the National Academy of Sciences of the United States of America 106, 2700 (Feb 24, 2009).

14.   A. R. Frand, S. Russel, G. Ruvkun, Functional genomic analysis of C. elegans molting. PLoS biology 3, e312 (Oct, 2005).

15.   D. Gems, L. Partridge, Genetics of longevity in model organisms: debates and paradigm shifts. Annual review of physiology 75, 621 (2013).

16.   C. L. Goodrich, Life span and the inheritance of longevity of mbred mice. J Gerontol 30, 257 (1975).

17.   D. Harman, Aging: a theory based on free radical and radiation chemistry. J Gerontol 11, 298 (Jul, 1956).

18.   D. Harman, The biologic clock: the mitochondria? Journal of the American Geriatrics Society 20, 145 (Apr, 1972).

19.   D. E. Harrison et al., Rapamycin fed late in life extends lifespan in genetically heterogeneous mice. Nature 460, 392 (Jul 16, 2009).

20.   T. Heidler, K. Hartwig, H. Daniel, U. Wenzel, Caenorhabditis elegans lifespan extension caused by treatment with an orally active ROS-generator is dependent on DAF-16 and SIR-2.1. Biogerontology 11, 183 (Apr, 2010).

21.   J. M. Herrmann, T. P. Dick, Redox Biology on the rise. Biological chemistry 393, 999 (Sep, 2012).

22.   M. Holzenberger et al., IGF-1 receptor regulates lifespan and resistance to oxidative stress in mice. Nature 421, 182 (Jan 9, 2003).

23.   C. Huang, C. Xiong, K. Kornfeld, Measurements of age-related changes of physiological processes that predict lifespan of Caenorhabditis elegans. Proceedings of the National Academy of Sciences of the United States of America 101, 8084 (May 25, 2004).

24.   K. Jia, D. Chen, D. L. Riddle, The TOR pathway interacts with the insulin signaling pathway to regulate C. elegans larval development, metabolism and life span. Development 131, 3897 (Aug, 2004).

25.   T. E. Johnson, D. H. Mitchell, S. Kline, R. Kemal, J. Foy, Arresting development arrests aging in the nematode Caenorhabditis elegans. Mechanisms of ageing and development 28, 23 (Nov, 1984).

26.   J. Johnston, W. B. Iser, D. K. Chow, I. G. Goldberg, C. A. Wolkow, Quantitative image analysis reveals distinct structural transitions during aging in Caenorhabditis elegans tissues. PloS one 3, e2821 (2008).

27.   I. L. Johnstone, Cuticle collagen genes. Expression in Caenorhabditis elegans. Trends in genetics : TIG 16, 21 (Jan, 2000).

28.   D. P. Jones, Radical-free biology of oxidative stress. American journal of physiology. Cell physiology 295, C849 (Oct, 2008).

29.   P. Kapahi et al., Regulation of lifespan in Drosophila by modulation of genes in the TOR signaling pathway. Current biology : CB 14, 885 (May 25, 2004).

30.   C. Kenyon, The first long-lived mutants: discovery of the insulin/IGF-1 pathway for ageing. Philosophical transactions of the Royal Society of London. Series B, Biological sciences 366, 9 (Jan 12, 2011).

31.   C. Kenyon, J. Chang, E. Gensch, A. Rudner, R. Tabtiang, A C. elegans mutant that lives twice as long as wild type. Nature 366, 461 (Dec 2, 1993).

32.   J. Kimble, D. Hirsh, The postembryonic cell lineages of the hermaphrodite and male gonads in Caenorhabditis elegans. Developmental biology 70, 396 (Jun, 1979).

33.   K. D. Kimura, H. A. Tissenbaum, Y. Liu, G. Ruvkun, daf-2, an insulin receptor-like gene that regulates longevity and diapause in Caenorhabditis elegans. Science 277, 942 (Aug 15, 1997).

34.   T. B. Kirkwood et al., What accounts for the wide variation in life span of genetically identical organisms reared in a constant environment? Mechanisms of ageing and development 126, 439 (Mar, 2005).

35.   W. G. Kirlin et al., Glutathione redox potential in response to differentiation and enzyme inducers. Free radical biology and medicine 27, 1208 (Dec, 1999).

36.   M. R. Klass, Aging in the nematode Caenorhabditis elegans: major biological and environmental factors influencing life span. Mechanisms of ageing and development 6, 413 (Nov-Dec, 1977).

37.   M. R. Klass, A method for the isolation of longevity mutants in the nematode Caenorhabditis elegans and initial results. Mechanisms of ageing and development 22, 279 (Jul-Aug, 1983).

38.   D. Knoefler et al., Quantitative in vivo redox sensors uncover oxidative stress as an early event in life. Molecular cell 47, 767 (Sep 14, 2012).

39.   T. Kojima et al., Association analysis between longevity in the Japanese population and polymorphic variants of genes involved in insulin and insulin-like growth factor 1 signaling pathways. Experimental gerontology 39, 1595 (Nov-Dec, 2004).

40.   M. S. Leduc et al., Identification of genetic determinants of IGF-1 levels and longevity among mouse inbred strains. Aging cell 9, 823 (Oct, 2010).

41.	Y. Li et al., Genetic association of FOXO1A and FOXO3A with longevity trait in Han Chinese populations. Human molecular genetics 18, 4897 (Dec 15, 2009).

42.	K. Lin, J. B. Dorman, A. Rodan, C. Kenyon, daf-16: An HNF-3/forkhead family member that can function to double the life-span of Caenorhabditis elegans. Science 278, 1319 (Nov 14, 1997).

43.	J. Z. Morris, H. A. Tissenbaum, G. Ruvkun, A phosphatidylinositol-3-OH kinase family member regulating longevity and diapause in Caenorhabditis elegans. Nature 382, 536 (Aug 8, 1996).

44.	S. Ogg et al., The Fork head transcription factor DAF-16 transduces insulin-like metabolic and longevity signals in C. elegans. Nature 389, 994 (Oct 30, 1997).

45.	A. P. Page, I. L. Johnstone, in WormBook T. C. e. R. Community, Ed. (2007).

46.	R. Pearl, The rate of living, being an account of some experimental studies on the biology of life duration. (A.A. Knopf, New York,, 1928), pp. 8 p.l., 185, 1 p.

47.	V. I. Perez et al., Is the oxidative stress theory of aging dead? Biochimica et biophysica acta 1790, 1005 (Oct, 2009) a.

48.	V. I. Perez et al., The overexpression of major antioxidant enzymes does not extend the lifespan of mice. Aging cell 8, 73 (Feb, 2009) b.

49.	M. Rubner, Volksernährungsfragen. (Akademische Verlagsgesellschaft m.b.H., Leipzig,, 1908), pp. iv, 143 p.

50.	T. J. Schulz et al., Glucose restriction extends Caenorhabditis elegans life span by inducing mitochondrial respiration and increasing oxidative stress. Cell metabolism 6, 280 (Oct, 2007).

51.	R. N. Singh, J. E. Sulston, Some observations on moulting in C. elegans. Nematologica, 63 (1978).

52.	P. E. Slagboom et al., Genomics of human longevity. Philosophical transactions of the Royal Society of London. Series B, Biological sciences 366, 35 (Jan 12, 2011).

53.	J. Stenvall et al., Selenoprotein TRXR-1 and GSR-1 are essential for removal of old cuticle during molting in Caenorhabditis elegans. Proceedings of the National Academy of Sciences of the United States of America 108, 1064 (Jan 18, 2011).

54.	J. Sulston, in The nematode C. elegans W. B. Wood, Ed. (Cold Spring Harbor Laboratory Press, Cold Spring Harbor, New York. , 1988), pp. 123-155.

55.	J. E. Sulston, H. R. Horvitz, Post-embryonic cell lineages of the nematode, Caenorhabditis elegans. Developmental biology 56, 110 (Mar, 1977).

56.	J. E. Sulston, E. Schierenberg, J. G. White, J. N. Thomson, The embryonic cell lineage of the nematode Caenorhabditis elegans. Developmental biology 100, 64 (Nov, 1983).

57.	M. Tatar, A. Bartke, A. Antebi, The endocrine regulation of aging by insulin-like signals. Science 299, 1346 (Feb 28, 2003).

58.	M. Tatar et al., A mutant Drosophila insulin receptor homolog that extends life-span and impairs neuroendocrine function. Science 292, 107 (Apr 6, 2001).

59.	M. C. Thein et al., Combined extracellular matrix cross-linking activity of the peroxidase MLT-7 and the dual oxidase BLI-3 is critical for post-embryonic viability in Caenorhabditis elegans. The Journal of biological chemistry 284, 17549 (Jun 26, 2009).

60.	A. R. Timme-Laragy et al., Glutathione redox dynamics and expression of glutathione-related genes in the developing embryo. Free radical biology and medicine 65C, 89 (Jun 13, 2013).

61.	J. M. Tullet et al., Direct inhibition of the longevity-promoting factor SKN-1 by insulin-like signaling in C. elegans. Cell 132, 1025 (Mar 21, 2008).

62.	J. M. Van Raamsdonk, S. Hekimi, Superoxide dismutase is dispensable for normal animal lifespan. Proceedings of the National Academy of Sciences of the United States of America 109, 5785 (Apr 10, 2012).

63.	B. J. Willcox et al., FOXO3A genotype is strongly associated with human longevity. Proceedings of the National Academy of Sciences of the United States of America 105, 13987 (Sep 16, 2008).

64.	J. L. Wong, R. Creton, G. M. Wessel, The oxidative burst at fertilization is dependent upon activation of the dual oxidase Udx1. Developmental cell 7, 801 (Dec, 2004).

Chapter 5

Differences in E_{GSH} across tissues and tissue communication

Abstract

The extent to which different cells and tissues in multicellular organisms communicate in order to coordinate their redox states is not yet known. To investigate how the organismal redox homeostasis is regulated, we implemented tissue-specific measurements of E_{GSH} in *C.elegans*. First, we established that the cytosolic E_{GSH} in *C.elegans* is indeed a tissue-specific variable: we observed different steady-state values of cytosolic E_{GSH} for feeding muscle, intestine and PLM neurons in young wild-type individuals. We also determined that insulin signaling has tissue-specific effects in the regulation of redox potential: *daf-2* mutants exhibit lower cytosolic E_{GSH} in feeding muscles and intestine compared to wild type, but show no effect in the cytosolic E_{GSH} of PLM neurons. As discussed in chapter 2, the effect of insulin signaling in the cytosolic redox potential requires the activity of the FOXO/DAF-16 transcription factor, so we tested whether this transcription factor acts locally or remotely to control cytosolic redox potential in feeding muscles. In *daf-16(mu86); daf-2(e1370)* double mutants the action of *daf-16(+)* in the pharynx is sufficient to lower E_{GSH} values in this tissue. Remarkably, the action of *daf-16(+)* in intestinal cells is also sufficient to lower E_{GSH} in feeding muscles, despite the absence of *daf-16* in this tissue, suggesting that the pharyngeal cytosolic redox environment can be modified by the action of other tissues, cell-non-autonomously.

Chapter 5 – Introduction

From cellular to organismal redox homeostasis

Biological organization at the cellular level reveals great specialization and capabilities for redox regulation:

1) *The cell coordinates subcellular compartments that differ widely in their redox environments*. Many functions in the cell depend on the spatial compartmentalization of redox potentials: from the electron transport chain in mitochondria, to oxidative protein folding in the ER, the cell exhibits great specialization of redox in different compartments. Glutathione potentials in the cell range from -280 mV in the mitochondrial matrix to -150 mV in the endoplasmic reticulum (ER), with cytosolic values falling between -220 to -260 mV (Cai & Jones 1998, Rebrin et al., 2004; Go & Jones, 2008; Jones 2010).

Even within the same compartment, the partitioning of redox reactions in space allows for great specialization in signaling and regulatory mechanisms. For instance, when the insulin receptor binds to its ligand, a local wave of oxidation in the proximity of the membrane is promoted by the action of NADPH oxidases. This wave of oxidation transiently inactivates nearby phosphatases, thus reinforcing signaling, but only in the proximity of the stimulus (Mahadev et al., 2004; Espinosa et al., 2009).

2) *The cell exhibits redox changes in different stages of its life cycle.* Decisions like proliferation, growth or apoptosis involve marked redox changes: cytosolic values of E_{GSH} are about -260 mV in cells under proliferative conditions, -220mV under differentiated conditions, and -170mV during apoptosis (Cai & Jones 1998; Kirlin et al., 1999). Measurements of E_{GSH} in zebrafish embryos during development show a similar trend. During the first 12 hours after fertilization, E_{GSH} increases exponentially from -230mV to -190mV; it then oscillates around -190mV during organogenesis and decreases again to -220 mV after hatching, which occurs about 72 h post-fertilization (Timme-Laragy et al., 2013).

In multicellular organisms, the scope to which already differentiated cells coordinate their redox states is unknown (Blackstone, 2000; Lalucque and Silar, 2003), and many open questions remain regarding how redox homeostasis works at the level of the organism. How does an organism coordinate the redox state of different cell-types and tissues? Is redox a local variable, defined autonomously by each cell? Or is it a global variable that integrates information about other tissues, in a cell-non-autonomous manner? Implementing tissue-specific measurements of E_{GSH} in *C.elegans*, with spatial-resolution, can make a valuable contribution in the investigation of organismal redox homeostasis.

Redox status of different tissues

Tissues have diverse energy requirements and metabolic rates. In humans, the resting energy expenditure is 440 kcal/kg per day for heart and also 440 for kidneys, 240 for

brain, 200 for liver, 13 for skeletal muscle, 4.5 for adipose tissue and 12 for residual mass

in the human body (Wang et al., 2012). Metabolism is the source of reducing equivalents,

such as NADPH, that are required for the reduction of oxidized glutathione and

thioredoxin. The extent to which E_{GSH} depends on the metabolic rates for different cell

types is not yet known.

Tissues also differ in their concentration of GSH and GSSG. There are 3 cellular

mechanisms that regulate GSH and GSSG concentration: synthesis, export (Ballatori et

al., 2009), and sequestration in vesicles (Morgan et al., 2013). Although in principle all

cells are able to synthesize glutathione in their cytoplasm, liver production of GSH is

essentially post-developmental (Chen et. al., 2007). HPLC measurements of GSH and

GSSG in tissue homogenates[13] in mice show up to a 10-fold difference in the average

concentration of GSH and GSSG for different tissues (see Figure 2.6 and discussion in

Chapter 2 about the relationship between [GSH]$_{Total}$ and E_{GSH}). These different tissues

can have GSH/GSSG ratios between 230:1 to 36:1; with the following rank order: brain >

testis > eye > liver = kidney > heart (Rebrin et al., 2003). The rank order of GSH/GSSG

ratios changes under different types of stress and pathologies, such us

hypoxia/reoxygenation, and inflammation (Fokkelman et al., 2007; Kemp et al., 2008;

Benton et al., 2012). Kemp et al., 2008 reports cytosolic E_{GSH} values[14] for human cells in

the range of -260 mV to -200mV, with liver being the most reduced, and red blood cells

---

[13] In this study, the E_{GSH} was not calculated because the homogenization will average
GSH and GSSG from different subcellular compartments.

[14] However, biochemical measurements of cytosolic E_{GSH} though HPLC have the burden
of proof to show no contamination with the contents of cell organelles.

being the most oxidized. Note that this range of E_{GSH} values are also outside the glutathione buffering regime discussed in Figure 2.6, suggesting that in mammalian cells E_{GSH} is a responsive variable, which will exhibit big fluctuations in response to small changes in [GSSG].

Different tissues also have different capacities to withstand oxidative imbalances. Particular attention has been given to the susceptibility of the nervous system, since oxidative damage is a hallmark of age-related neurodegenerative diseases. Oxidative stress and protein misfolding –where the GSH:GSSG ratio is critical for the function of the ER–, have been associated with Alzheimer's, Parkinson's and Huntington's diseases, amyotrophic lateral sclerosis, and Friedreich's ataxia (Johnson et al., 2012).

Skeletal muscle, on the other hand, is resilient to oxidative stress: during aerobic exercise, muscle upregulates adaptative responses, including antioxidant enzymes and heat shock proteins (McArdle & Jackson, 2000). Recently, Welc & Clanton, 2013 hypothesized that skeletal muscle works as an integrative stress sensor. The recent discovery of myokines – cytokines secreted by skeletal muscle mainly in response to exercise, but also to internal stresses such us oxidative stress, unfolded proteins and hyperthermia – provides a conceptual basis for exploring how muscles communicate with other organs in response to oxidative stress (Pedersen and Febbraio, 2008; Pedersen and Febbraio, 2012).

Tissue specificity of insulin signaling

The human insulin receptor substrate proteins IRS1 and IRS2 are regulated by a complex mechanism of post-translational modifications, which can have both positive and negative effects on the receptor's activity. This regulation depends on a combinatorial state of more than 50 serine/threonine phosphorylation sites, plus other modifications like lysine acetylation and serine-linked N-acetylglucosamine (Copps & White, 2012; Fisher-Wellman, & Neufer, 2012). In the worm, part of this combinatorial regulation seems to be encoded not in the receptor itself, but in its ligands. The worm encodes 40 insulin-like peptides, many of them with unknown function. The closest homologue to the human insulin peptide, both in sequence and structural similarity, is INS-1. Curiously, INS-1 seems to act as an antagonist of DAF-2: overexpression of *ins-1* results in decreased DAF-2 signaling activity and extends lifespan in the worm (Pierce et al., 2001). However, INS-7 and DAF-28 are insulin genes that function as agonists (Li et al., 2008 ; Murphy et al., 2007).

Mosaic analysis and tissue-specific rescue suggests that inactivation of *daf-2* in small subpopulations of neurons is sufficient to initiate hormonal changes that lead to longevity (Apfeld & Kenyon, 1998; Wolkow et al., 2000); *daf-16* activity is required in other tissues to receive those hormonal signals and execute metabolic changes (Libina et al., 2003; Iser et al., 2007). This tissue-specific evidence suggests that neurons receive environmental inputs, which are then transduced into inactivation of DAF-2, and activation of DAF-16. Hormonal signals from those neurons are sent to other tissues in the worm, decreasing insulin/IGF signaling locally and activating DAF-16 in the target

161

tissues. These target tissues, like the intestine, execute metabolic changes and can amplify hormonal input to induce more global changes (Murphy et al., 2007). Understanding the network of agonist and antagonist effects of the 40 insulins, and mapping their spatio-temporal pattern of expression to the roles of different tissues, will clarify how insulin-controlled metabolic changes modulate the aging process of the worm.

Redox imbalances and the deregulation of insulin signaling

Several components of the insulin signaling pathway are under regulatory control of redox modifications. Stimulation of the insulin receptor initiates a local wave of ROS via NADPH oxidases, which inhibits the catalytic activity phosphatases. This local and transient event reinforces the initial steps of phosphorylation-dependent signaling (Mahadev et al., 2004; Espinosa et al., 2009). Recently, AGE-1/PI3K was shown to contain redox sensitive cysteines (Knoefler et al., 2012); DAF-16/FOXO nuclear localization is mediated by disulfide formation with transportin-1 (Putker et al., 2013); and the activity of the transcription factor SKN-1/NRF-2 is presumably controlled by the redox state of cysteines, as in its mammalian homologue NRF-2 (Dinkova-Kostova et al., 2002).

Conversely, de-regulation of redox homeostasis is associated with the development of insulin resistance: over-nutrition and physical inactivity are major risk factors, and can cause diabetes. Nutrient overload imposes an overflow of reducing equivalents in the cells, which increases emission of superoxide from the mitochondria (Anderson et al.,

2009). This ROS emission is thought to work as a release valve for the excess of electrons in the mitochondrial electron transport chain, created by fuel overload. The persistent emission of H_2O_2 is expected to *i)* affect cellular redox circuits, and *ii)* depress phosphatase activity, ultimately leading to the deregulation of phosphorylation based signaling (Fisher-Wellman & Neufer et al., 2012).

Chapter 5 – Results

To investigate how the redox status in different tissues varies in the physiological context of living organism, we measured three *C.elegans* tissues *in vivo,* representing the three primary developmental layers: intestine for the endoderm; feeding muscles for the mesoderm; and PLM touch neurons, to represent the ectoderm (Figure 5.1). We found significant differences in the cytosolic values of E_{GSH} for these three tissues (Table 5.1): intestine shows the highest E_{GSH} (-268.1 ± 2.1 mV), PLM neurons have an intermediate value of E_{GSH} (-269.9 ± 1.3), and feeding muscles have the lowest E_{GSH} of all (-270.9 ± 1.7 mV). Overall, *C.elegans* tissues have a more oxidizing cytosolic environment than yeast (E_{GSH} = -290 mV) (Morgan et al., 2013) and various tissues of *Drosophila* larvae (E_{GSH} < -300 mV) (Albrecht et al., 2011), while they have a more reducing environment than mammalian liver (E_{GSH} = -255 mV) and intestine (E_{GSH} = -220 mV) (Kemp et al., 2008). It is interesting to notice that the cytosolic E_{GSH} of different species varies so widely. How the evolution of redox-sensitive regulatory mechanisms coevolves with this change is a thought-provoking question, to be explored when more species-specific measurements become available.

Little is known about the phenotypic variability of the redox status between different individuals. This information is essentially inaccessible to biochemical measurements, which requires averaging over the population. In isogenic populations of 2-day-old worms, we observe a wide variability of E_{GSH}: we observe differences between individuals of up to 13.3 mV in intestine, 10.7 mV in pharynx, while the values for

neurons are the least dispersed, covering a range of 7.3 mV. As discussed in Chapter 4, the variability in E_{GSH} values for feeding muscle increases with aging.

In Chapter 3, we showed how insulin signaling modulates the cytosolic redox state in feeding muscle. Given the complex combinatorial network of insulin regulation in the worm, we next asked whether this hormonal signal modulates the redox state of different tissues in a differential manner. Although it has only one insulin/IGF-1 receptor, the worm has 40 insulin-like peptides with a wide diversity of spatio-temporal expression patterns in different tissues. Particular specialization is seen in the nervous system, where at least 15 insulin-like peptides are expressed in different subpopulations of neurons (Li and Kim, 2008). We found that *daf-2(e1370)* mutants exhibit lower E_{GSH} than wild-type animals in feeding muscle and intestine, but not in PLM neurons (Figure 5.2), indicating that the effect of insulin/IGF-1 signaling on the cytosolic redox environment is tissue specific (Table 5.2).

In the worm, the action of insulin signaling in specific tissues is crucial for the pathway to affect longevity systemically (Apfeld & Kenyon 1998; Libina et al., 2003). Reduced DAF-2 activity in neurons prompts DAF-16/FOXO nuclear translocation, which decreases the neuronal production of hormones like insulin-like peptide INS-7. Once systemic levels of INS-7 have decreased, DAF-16/FOXO in the intestine translocate to the nucleus. The activity of DAF-16/FOXO in the intestine in turn increases the production of additional hormones while inhibiting the production of insulin-like peptides (Murphy et al., 2007). Thus, the activity of the DAF-16/FOXO transcription factor in one
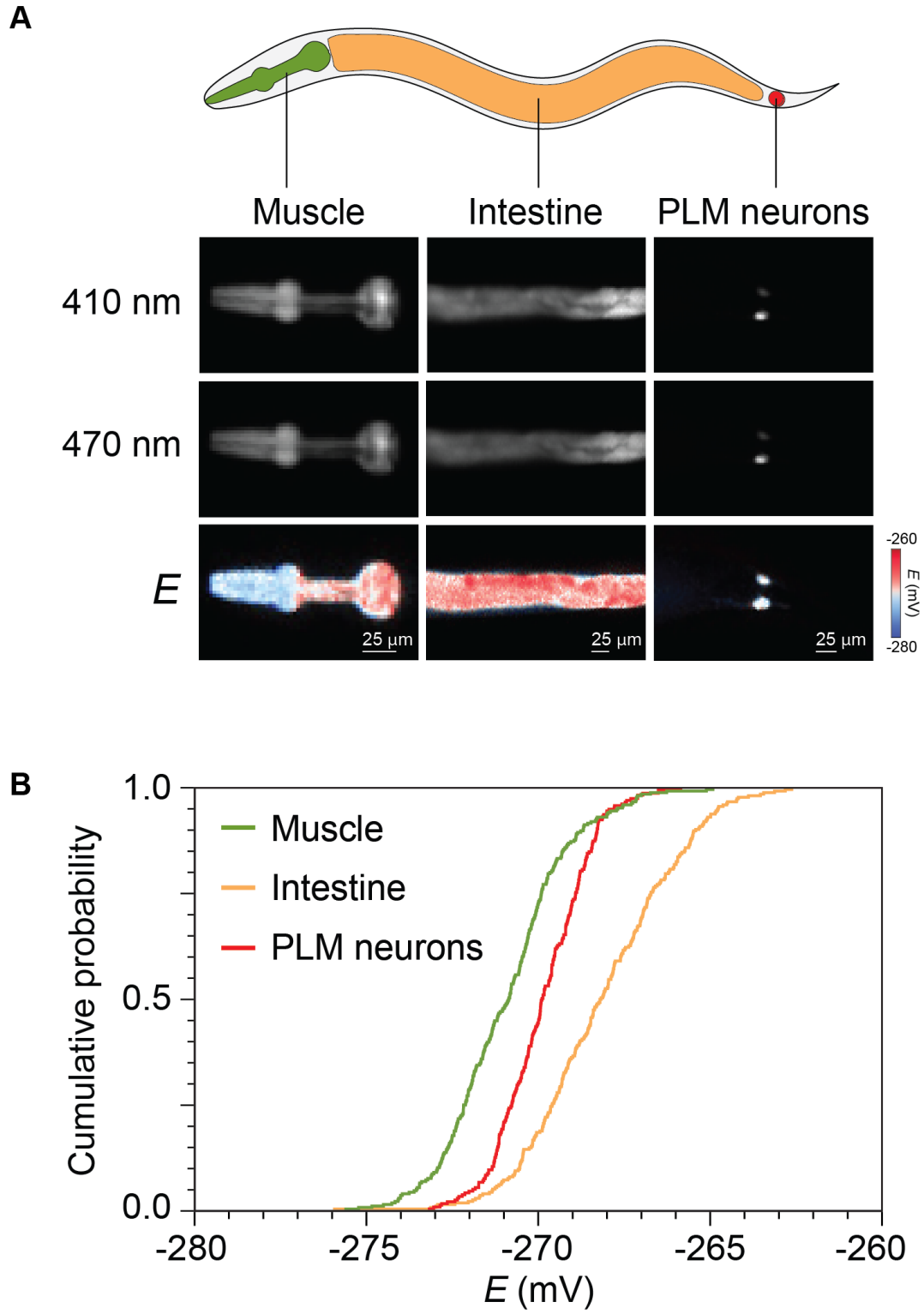
Figure 5.1: Cytosolic redox potentials of different tissues in wild type animals

(**Figure 5.1** *continued)* We measured the cytosolic redox potential in transgenic animals expressing roGFP1_R12 in pharyngeal muscles, intestine, and PLM motor neurons. The relative positions of these organs and cells in the animal are denoted by the diagram at the top. (A) Fluorescence images of animals expressing roGFP1_R12 in specific tissues upon illumination with 410 and 470 nm light (top and middle rows), and visualization of the pixel-by-pixel redox potential (E) derived from these images (bottom row). These animals exhibited E values close to the average for the tissue. (B) Cumulative distributions of E values in pharyngeal muscles, intestine, and PLM motor neurons. These tissues exhibited significant differences in average E ($P < 0.0001$ for all pair-wise comparisons, Tukey HSD test). For statistics see Table 5.1

Figure 5.2: Tissue-specific effects of insulin signaling on redox potential
(following page). We measured the cytosolic redox potential in transgenic animals expressing roGFP1_R12 in pharyngeal muscles, intestine, and PLM motor neurons, for both wild type and *daf-2(e1370)* mutants. Compared to wild type, *daf-2(e1370)* mutants exhibit lower cytosolic E in feeding muscles (A) and intestine (B), but do not affect cytosolic E in PLM neurons (C). For statistics see Table 5.2
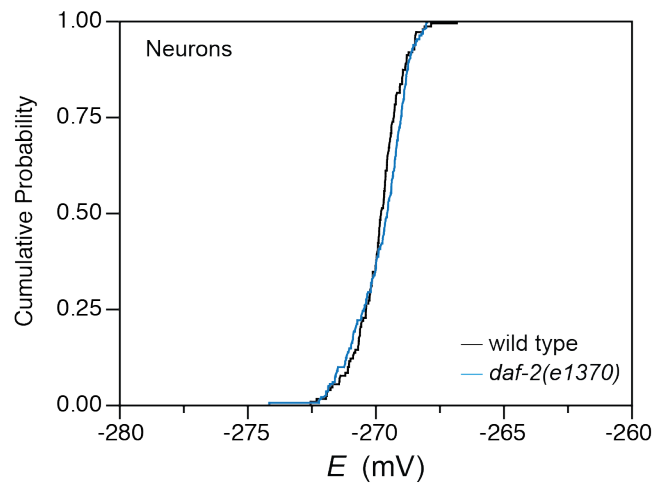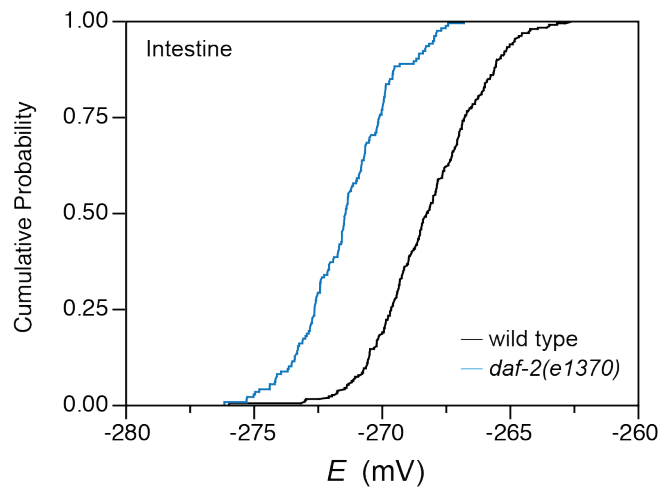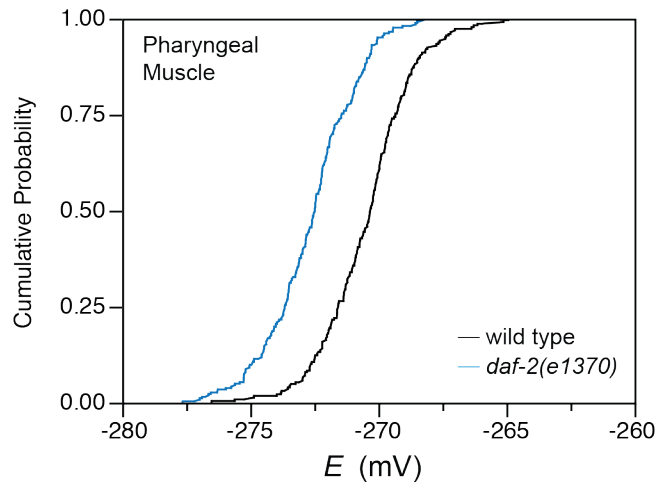
(**Figure 5.2** *continued*)

168

tissue can modulate its activity in other tissues through hormonal signaling.

We wanted to investigate whether the expression of the DAF-16/FOXO transcription factor remotely could affect the cytosolic redox state in the pharynx. To see if there is a cell non-autonomous effect, we chose to express DAF-16 in the intestine, since expression of this transcription factor in this tissue is sufficient to affect global phenotypes in the worm, such as lifespan. We performed this tissue-specific rescue experiment in 6-day-old adults, where the difference in the cytosolic E_{GSH} of feeding muscles between phenotypes of wild-type and *daf-2(e1370)* mutant give us a greater dynamic range, allowing us to detect smaller differences (see Figure 4.8).

First, we expressed *daf-16(+)* locally in the pharynx, and we confirmed that local activity of DAF-16/FOXO in 6-day-old individuals lowers the E_{GSH} in *daf-16(mu86);daf-2(e1370)* double mutants, as was shown for 2-day-old worms. Next, we restored *daf-16(+)* exclusively in the intestine for *daf-16(mu86);daf-2(e1370)* double mutants, and found that the activity of this transcription factor is sufficient to lower cytosolic E_{GSH} in feeding muscles that lack *daf-16* (Figure 5.3). This evidence suggests that the pharyngeal cytosolic redox environment can be modified by the action of other tissues, in an insulin/IGF-1-independent manner (Table 5.3).

169
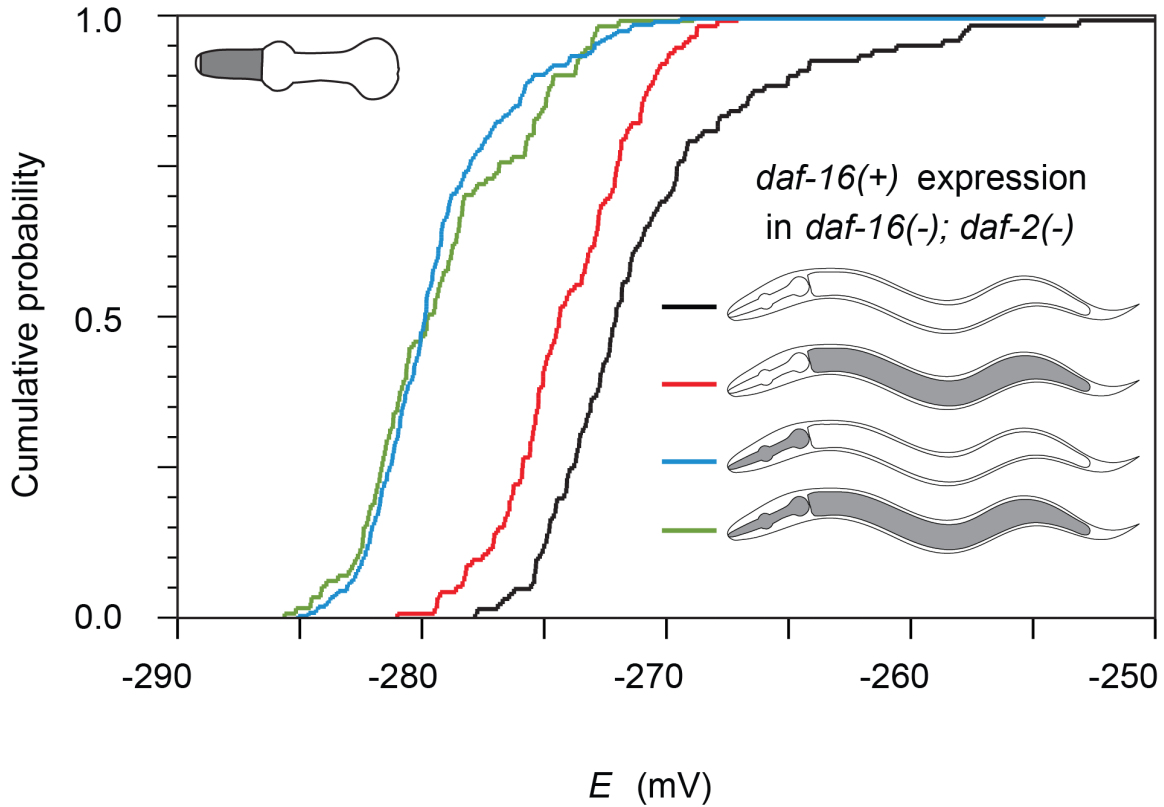
Figure 5.3: Activity of DAF-16/FOXO transcription factor in intestine can affect the redox potential in the pharynx

Insulin signaling can act locally or remotely to regulate the redox potential of the pharynx. In *daf-16(mu86); daf-2(e1370)* double mutants the action of *daf-16(+)* in feeding muscles (blue) is sufficient to lower E values in this tissue, compared to their siblings with no pharyngeal *daf-16(+)* expression (black). The action of *daf-16(+)* in intestinal cells (red) is also sufficient to lower E in feeding muscles, despite the absence of *daf-16* in this tissue. For statistics see Table 5.3

Murphy et al., 2007 showed that by experimentally increasing the activity of DAF-16 in one tissue, the activity in other tissues rises, through a feedback mechanism involving INS-7, so called "FOXO to FOXO" communication. To test whether this interaction could further decrease cytosolic E_{GSH} in pharyngeal muscle, we expressed *daf-16(+)*in both pharyngeal muscle and intestine. No difference is observed when expressing DAF-16/FOXO in both tissues as compared to the local rescue alone; this suggests that, for redox regulation, there is no synergistic interaction between these two tissues (Figure 5.3).

Our results show that different tissues in *C.elegans* have different steady-state values for cytosolic E_{GSH}. The magnitude of this difference (a range of 2.8 mV between intestine and muscle) is comparable to the effect that the *daf-2(e1370)* mutant has in intestine and feeding muscle. Our results also support the involvement of insulin signaling in the tissue-specification of the redox environment, as well as the participation of FOXO/DAF-16 in tissue-to-tissue communication, which can modulate the cytosolic redox environment in a cell non-autonomous manner.

Author contributions

Catalina Romero (C.R), and Javier Apfeld (J.A.) designed research; C.R. performed research; C.R. and J.A. analyzed data; C.R. wrote the manuscript.

Table 5.1 – Measurements of redox potential in different tissues

A) Descriptive statistics. Potentials reported as [mean ± s.d. (n), mV]

Genotype	N	Tissue	E
	(276)	pharynx	-270.9 ± 1.7
wild type	(276)	intestine	-268.1 ± 2.1
	(239)	PLM neurons	-269.9 ± 1.3

B) Statistical comparisons between tissues. Reported as [mean ± s.e., mV]

Genotype	Tissues		$\Delta\langle E \rangle$	p-value
	intestine	pharynx	2.8 ± 0.1	< 0.0001
wild type	intestine	PLM neurons	1.7 ± 0.2	< 0.0001
	PLM neurons	pharynx	1.1 ± 0.2	< 0.0001

Table 5.2 – *daf-2* has a tissue-specific effect on redox potential

A) Descriptive statistics. E in [mean ± s.d. (n), mV], and Δ E in [mean ± s.e., mV]

Tissue	Genotype	N	E	Δ⟨E⟩	p-value
Pharynx	wild type	(227)	-270.4 ± 1.8	-2.2 ± 0.2	< 0.0001
	daf-2(e1370)	(263)	-272.6 ± 1.8		
Intestine	wild type	(276)	-268.1 ± 2.1	-3.2 ± 0.2	< 0.0001
	daf-2(e1370)	(151)	-271.3 ± 1.8		
PLM neurons	wild type	(133)	-269.8 ± 0.9	0.1 ± 0.1	0.700
	daf-2(e1370)	(205)	-269.8 ± 1.0		

Table 5.3 – Site of *daf-16* action in pharyngeal redox control

A) Descriptive statistics. Reported as [mean ± s.d. (n), mV] (experiments performed on 6-day-old individuals).

Genetic background	*daf-16(+)* expression	
	none	-270.8 ± 4.9 (120)
daf-16(mu86); daf-2(e1370)	pharynx	-279.3 ± 3.4 (193)
	intestine	-274.0 ± 2.8 (112)
	pharynx + intestine	-279.2 ± 3.4 (111)

B) Parameter estimates for linear model, estimate ± s.e. (mV) and p-value

Term	
intercept	-270.8 ± 0.3 *< 0.0001*
pharynx	-8.4 ± 0.4 *< 0.0001*
intestine	-3.2 ± 0.5 *< 0.0001*
pharynx * intestine	3.4 ± 0.7 *< 0.0001*

Model: E = Intercept + pharynx + intestine + pharynx * intestine + ε

Chapter 5 – Methods

In Chapter 2, we described the construction of the transgene expressing the sensor in pharyngeal muscle, and the generation of transgenic animals with the insertion *ydIs1[pmyo-2::roGFP1_R12 + rol-6(su1006)]*. To express roGFP1_R12 in motor neurons, we amplified the *mec-4* promoter from *C.elegans* genomic DNA with the primers WF96 and WF99 (Table S1), and cloned the PCR product into a TOPO BluntII vector. *roGFP1_R12* was inserted into this vector backbone by restriction with AgeI and PstI, generating *Pmec-4:: roGFP1_R12*. Intestinal expression of roGFP1_R12 was achieved using the *sur-5* promoter. We amplified this promoter region from pPD158.87 (Fire vector kit, Addgene) with primers WF45 and WF49, and cloned the PCR product into a TOPO BluntII vector. We fused this promoter to a restriction fragment containing *roGFP1_R12* by secondary PCR using primers WF38 and WF129, generating *sur-5::roGFP1_R12*.

Although we expected the *sur-5* promoter to drive roGFP1_R12 expression in several tissues, at the 100X magnification we used for imaging animals throughout this study we found that our transgenic lines exhibit high expression of roGFP1_R12 only in the intestine. Very infrequently (in less than 2% of the worms) we observed very faint fluorescence signals from tissues other than the intestine; in such cases, the animals were not imaged. During the image analysis we used the morphology and location of the intestine to ensure that the fluorescence intensity of the segmented region derives exclusively from the intestine.

The plasmid containing *Pmec-4::roGFP1_R12* was microinjected using *rol-6(su1006)* as coinjection marker. The plasmid containing *Psur-5::roGFP1_R12* was microinjected without a coinjection marker. *Pmec-4::roGFP1_R12* and *Psur-5::roGFP1_R12* were microinjected into wild type to generate *ydEx37* and *ydEx25* respectively. Transgenic lines were maintained by picking rollers or by picking fluorescent individuals.

Double and triple mutants were generated by standard genetic methods. The 25°C Daf-c phenotype was used to identify *daf-2* mutants. *daf-16(mu86)* and *daf-16(+)* were distinguished by PCR (Lin et al., 1997). *ydIs1* was identified based on the presence of green fluorescence in the pharynx. *ydEx37* was identified based on the presence of green fluorescence in mechanosensory neurons. *ydEx25* was identified based on the presence of green fluorescence in the intestine.

For the cell-non-autonomous experiment we used the following transgenes:

- *ExYW [Pmyo-2::daf-16d/f::Cherry; rol-6 (su1006)]* was identified based on the presence of red florescence in the pharynx.
- *muEx268[pNL213 (Pges-1::GFP::daf-16cDNA) + odr-1::RFP]* was identified based on the expression of the *odr-1::*RFP coinjection marker.
- *daf-16(mu86); daf-2(e1370); ydIs1; muEx268* was constructed by crossing *daf-16(mu86); daf-2(e1370); ydIs1* males to *daf-16(mu86); daf-2(e1370); muEx268* hermaphrodites.

- *daf-16(mu86); daf-2(e1370); ydIs1; ExYW* was constructed by crossing *daf-16(mu86); daf-2(e1370); ydIs1* males to *daf-16(mu86); daf-2(e1370); ExYW* hermaphrodites.

- *daf-16(mu86); daf-2(e1370); ydIs1; ExYW; muEx268* was constructed by crossing *daf-16(mu86); daf-2(e1370); ydIs1; muEx268* males with *daf-16(mu86); daf-2(e1370); ExYW* hermaphrodites.

Live microscopy and ratiometric measurements were as described in Chapter 3. To perform the ratiometric fluorescent measurements, we optimized the microscopy protocol for each tissue. We optimized exposure times to use at least two-thirds of the dynamic range of the camera. This step ensured that image segmentation was performed consistently across all experimental conditions and for all imaged tissues. We chose the camera binning based on the spatial resolution required for tissues of different morphology.

To image the feeding muscles of the pharynx, we focused on the plane of the pharyngeal lumen under transmitted light. Fluorescence images were acquired with 4x4 binning using an average exposure time of 40 ms. To image intestine, we concentrated on the posterior region of the tissue, which exhibits higher expression of the sensor. Fluorescence images were acquired with 4x4 binning, using average exposure times of 105 ms. To image mechanosensory neurons, we selected the PLMs neurons because they are located at the tail of the worm where the specimen is thin and flat and, therefore, short focal depth is required for imaging. Because the *rol-6* coinjection marker induces

twisting of the body, only one of the two PLM neurons was quantified for each worm.

Fluorescence images were acquired with 2x2 binning using average exposure times of

450 ms.

Image processing for the three tissues was performed as described in Chapter 3 for the

pharyngeal images. In addition, we used the same intensity value for the segmentation

across all tissues and conditions. In the case of PLM neurons, the ROIs correspond to

single cells; for intestine, they correspond to the most posterior portion of the tissue

(approximately 85 μm in length); and for feeding muscles, they correspond to the entire

pharynx. We used the ROIs to quantify both the 410 nm and 470 nm excitation images

(I_{410} and I_{470} images, respectively).

For the experiment testing cell non-autonomy we built a *daf-16(mu86); daf-2(e1370)*;

ydIs1; ExYW; muEx268 strain, which generates siblings with one, both or none of the

extrachromosomal transgenes. These animals were imaged on day 6 of adulthood. The

muEx268[Pges-1::GFP::daf-16cDNA + odr-1::RFP] transgene expresses a GFP-DAF-

16 fusion protein in the intestine and only animals with visible intestinal GFP expression

where considered for this experiment. In control experiments on animals that do not carry

ydIs1, we found that *muEx268* does not cause any detectable levels of GFP expression in

the pharynx at 1000X magnification. The *ExYW[Pmyo-2::daf-16d/f::Cherry + rol-

6(su1006)]* transgene expresses *daf-16(+)* in the pharynx. In control experiments on

animals that do not carry *ydIs1*, we found that the DAF-16D/F-Cherry expressed from

this transgene has no detectable signal through the roGFP1_R12 emission filter when

illuminated at 410 or 470nm. Animals carrying this transgene where identified based on their expression of Cherry in the pharynx. We confirmed the genotype of each animal at the time of imaging roGFP1_R12, by taking pictures of the intestine in the GFP channel and the pharynx in the RFP channel.

References

1. Apfeld J, Kenyon C (1998) Cell nonautonomy of C. elegans daf-2 function in the regulation of diapause and life span. Cell 95: 199-210.

2. Ballatori N, Krance SM, Marchan R, Hammond CL (2009) Plasma membrane glutathione transporters and their roles in cell physiology and pathophysiology. Mol Aspects Med 30: 13-28.

3. Ballatori N, Krance SM, Notenboom S, Shi S, Tieu K, et al. (2009) Glutathione dysregulation and the etiology and progression of human diseases. Biol Chem 390: 191-214.

4. Benton SM, Liang Z, Hao L, Liang Y, Hebbar G, et al. (2012) Differential regulation of tissue thiol-disulfide redox status in a murine model of peritonitis. J Inflamm (Lond) 9: 36.

5. Blackstone NW (2000) Redox control and the evolution of multicellularity. Bioessays 22: 947-953.

6. Cai J, Jones DP (1998) Superoxide in apoptosis. Mitochondrial generation triggered by cytochrome c loss. J Biol Chem 273: 11401-11404.

7. Chen Y, Yang Y, Miller ML, Shen D, Shertzer HG, et al. (2007) Hepatocyte-specific Gclc deletion leads to rapid onset of steatosis with mitochondrial injury and liver failure. Hepatology 45: 1118-1128.

8. Copps KD, White MF (2012) Regulation of insulin sensitivity by serine/threonine phosphorylation of insulin receptor substrate proteins IRS1 and IRS2. Diabetologia 55: 2565-2582.

9. Dinkova-Kostova AT, Holtzclaw WD, Cole RN, Itoh K, Wakabayashi N, et al. (2002) Direct evidence that sulfhydryl groups of Keap1 are the sensors regulating induction of phase 2 enzymes that protect against carcinogens and oxidants. Proc Natl Acad Sci U S A 99: 11908-11913.

10. Espinosa A, Garcia A, Hartel S, Hidalgo C, Jaimovich E (2009) NADPH oxidase and hydrogen peroxide mediate insulin-induced calcium increase in skeletal muscle cells. J Biol Chem 284: 2568-2575.

11. Fisher-Wellman KH, Neufer PD (2012) Linking mitochondrial bioenergetics to insulin resistance via redox biology. Trends Endocrinol Metab 23: 142-153.

12. Fokkelman K, Haase E, Stevens J, Idikio H, Korbutt G, et al. (2007) Tissue-specific changes in glutathione content of hypoxic newborn pigs reoxygenated with 21% or 100% oxygen. Eur J Pharmacol 562: 132-137.

13. Go YM, Jones DP (2008) Redox compartmentalization in eukaryotic cells. Biochim Biophys Acta 1780: 1273-1290.

14. Iser WB, Gami MS, Wolkow CA (2007) Insulin signaling in Caenorhabditis elegans regulates both endocrine-like and cell-autonomous outputs. Dev Biol 303: 434-447.

15. Johnson WM, Wilson-Delfosse AL, Mieyal JJ (2012) Dysregulation of glutathione homeostasis in neurodegenerative diseases. Nutrients 4: 1399-1440.

16. Jones DP, Go YM (2010) Redox compartmentalization and cellular stress. Diabetes Obes Metab 12 Suppl 2: 116-125.

17. Kemp M, Go YM, Jones DP (2008) Nonequilibrium thermodynamics of thiol/disulfide redox systems: a perspective on redox systems biology. Free Radic Biol Med 44: 921-937.

18. Kirlin WG, Cai J, Thompson SA, Diaz D, Kavanagh TJ, et al. (1999) Glutathione redox potential in response to differentiation and enzyme inducers. Free Radic Biol Med 27: 1208-1218.

19. Knoefler D, Thamsen M, Koniczek M, Niemuth NJ, Diederich AK, et al. (2012) Quantitative in vivo redox sensors uncover oxidative stress as an early event in life. Mol Cell 47: 767-776.

20. Lalucque H, Silar P (2003) NADPH oxidase: an enzyme for multicellularity? Trends Microbiol 11: 9-12.

21. Li C, Kim K (2008) Neuropeptides. WormBook: 1-36.

22. Libina N, Berman JR, Kenyon C (2003) Tissue-specific activities of C. elegans DAF-16 in the regulation of lifespan. Cell 115: 489-502.

23. Lin K, Dorman JB, Rodan A, Kenyon C (1997) daf-16: An HNF-3/forkhead family member that can function to double the life-span of Caenorhabditis elegans. Science 278: 1319-1322.

24. Mahadev K, Motoshima H, Wu X, Ruddy JM, Arnold RS, et al. (2004) The NAD(P)H oxidase homolog Nox4 modulates insulin-stimulated generation of H2O2 and plays an integral role in insulin signal transduction. Mol Cell Biol 24: 1844-1854.

25. McArdle A, Jackson MJ (2000) Exercise, oxidative stress and ageing. J Anat 197 Pt 4: 539-541.

26. Morgan B, Ezerina D, Amoako TN, Riemer J, Seedorf M, et al. (2013) Multiple glutathione disulfide removal pathways mediate cytosolic redox homeostasis. Nat Chem Biol 9: 119-125.

27. Murphy CT, Lee SJ, Kenyon C (2007) Tissue entrainment by feedback regulation of insulin gene expression in the endoderm of Caenorhabditis elegans. Proc Natl Acad Sci U S A 104: 19046-19050.

28. Pedersen BK, Febbraio MA (2008) Muscle as an endocrine organ: focus on muscle-derived interleukin-6. Physiol Rev 88: 1379-1406.

29. Pedersen BK, Febbraio MA (2012) Muscles, exercise and obesity: skeletal muscle as a secretory organ. Nat Rev Endocrinol 8: 457-465.

30. Pierce SB, Costa M, Wisotzkey R, Devadhar S, Homburger SA, et al. (2001) Regulation of DAF-2 receptor signaling by human insulin and ins-1, a member of the unusually large and diverse C. elegans insulin gene family. Genes Dev 15: 672-686.

31. Putker M, Madl T, Vos HR, de Ruiter H, Visscher M, et al. (2013) Redox-dependent control of FOXO/DAF-16 by transportin-1. Mol Cell 49: 730-742.

32. Rebrin I, Kamzalov S, Sohal RS (2003) Effects of age and caloric restriction on glutathione redox state in mice. Free Radic Biol Med 35: 626-635.

33. Rebrin I, Sohal RS (2004) Comparison of thiol redox state of mitochondria and homogenates of various tissues between two strains of mice with different longevities. Exp Gerontol 39: 1513-1519.

34. Timme-Laragy AR, Goldstone JV, Imhoff BR, Stegeman JJ, Hahn ME, et al. (2013) Glutathione redox dynamics and expression of glutathione-related genes in the developing embryo. Free Radic Biol Med 65C: 89-101.

35. Wang Z, Ying Z, Bosy-Westphal A, Zhang J, Heller M, et al. (2012) Evaluation of specific metabolic rates of major organs and tissues: comparison between nonobese and obese women. Obesity (Silver Spring) 20: 95-100.

36. Welc SS, Clanton TL (2013) The regulation of interleukin-6 implicates skeletal muscle as an integrative stress sensor and endocrine organ. Exp Physiol 98: 359-371.

37. Wolkow CA, Kimura KD, Lee MS, Ruvkun G (2000) Regulation of C. elegans life-span by insulinlike signaling in the nervous system. Science 290: 147-150.

Table S1 - Gene alleles and strains

Genotype

ydIs1[Pmyo-2::roGFP1_R12; rol-6 (su1006)]IV

daf-16(mu86)I; daf-2(e1370)III; ydIs1[Pmyo-2::roGFP1_R12; rol-6 (su1006)]IV

daf-2(e1370)III; ydIs1[Pmyo-2::roGFP1_R12; rol-6 (su1006)]IV

daf-16(mu86)I; ydIs1[Pmyo-2::roGFP1_R12; rol-6 (su1006)]IV

daf-16(mu86)I; daf-2(e1370)III; ydIs1[Pmyo-2::roGFP1_R12; rol-6 (su1006)]IV; muEx268[pNL213 (Pges-1::GFP::daf-16cDNA) + odr-1::RFP]

daf-16(mu86)I; daf-2(e1370)III; ydIs1[Pmyo-2::roGFP1_R12; rol-6 (su1006)]IV; ExYW[Pmyo-2::daf-16d/f::Cherry; rol-6 (su1006)]; (continue)

muEx268[pNL213 (Pges-1::GFP::daf-16cDNA) + odr-1::RFP]

daf-16(mu86)I; daf-2(e1370)III; ydIs1[Pmyo-2::roGFP1_R12; rol-6 (su1006)]IV; ExYW[Pmyo-2::daf-16d/f::Cherry; rol-6 (su1006)]

ydEx25[Psur-5::roGFP1_R12; 1 kb ladder]

daf-2(e1370)III; ydEx22[Psur-5::roGFP1_R12; rol-6 (su1006)]

ydEx37 [Pmec-4::roGFP1_R12; rol-6 (su1006); 1kb lader]

daf-2(e1370)III; ydEx37 [Pmec-4::roGFP1_R12; rol-6 (su1006); 1kb lader]

Table S2 – List of primers

Primer	Sequence
WF 38	GGCTGAAATCACTCACAACG
WF 45	GAGTCAGTGAGCGAGGAAGC
WF 46	TTCTTCTCCTTTACTCATTTTTTCTACCGGTACCCTCCTGAAAATGTTCTATGTTATGTT
WF 49	CTTTACTCATTTTTTCTACCGGTACCAATACGACTCACTATAGGGCACCC
WF 96	AAATCTTCTCACGTCATAACCT
WF 99	CTTTACTCATTTTTTCTACCGGTACATCCATGACATTCTATAACTTGATA
WF 129	CCCGGCGTGTCAATAATATC

Appendix 1 – *Personal Acknowledgements*

*"It takes a whole village
to raise one child"*

This saying came immediately to mind when I thought of the long list of people who contributed time and effort to this project, and helped me grow as a scientist and as a person. I feel that, indeed, it takes more than one community to bring these large projects to life. I would like to acknowledge each of them here.

The intellectual support I received from the Harvard scientific community has been invaluable for the completion of this work. Acknowledgements for specific scientific contributions, pertinent to each section, are found within each chapter. In this appendix, I would like to extend my gratitude to a larger circle of people from Harvard, whose contributions over the last years have fed many other dimensions of my scientific and personal development.

First, I would like to express gratitude to my advisor, Walter Fontana: for the intellectual authenticity that drives his mind along a gradient of *interestingness*, never compromising depth for any other parameter; for the power of his abstractions and the beauty of his metaphors; and for the humane nature he carries with him wherever he goes.

I would also like to express my deepest gratitude to Javier Apfeld, my advisor *de facto*: for pouring his knowledge and expertise into our group with such dedication and enthusiasm; for generously giving of his time and energy; for his immense optimism that makes possible the unlikely; and particularly for teaching me, not only about science, but about the resilience and integrity of the human spirit.

Thanks to Nicholas Stroustrup, for his company in these years, for his steadiness, his courage, his sense of humor and his persistence.

To Deborah Marks, for her inspiring polymath abilities, that allow her to belong to different intellectual circles and occupy many roles at once; and for all the energy and support she invested in the projects of the Fontana Lab.

To Daniel Yamins, for his eager intellect and insightful mind, and in particular for early discussions on pattern formation and local-to-global theory, which clearly influenced this project.

I would also like to thank other former members of the Fontana lab: to Van Savage, for the conversations about literature and perspectives about life; to Eric Deeds for his keenness and his energy; to Tom Kolokotrones for his ability to integrate so many different sciences; and to the members in the theoretical side of the lab, in particular to Vincent Danos, Jean Krivine, Jérôme Feret.